EFFECT OF RADIATION INDUCED DEFECTS ON THE OPTICAL TRANSITIONS OF 3-d IMPURITIES

By

KUO-HUA LEE

Bachelor of Science in Electrical Engineering
Tatung Institute of Technology
Taipei, Taiwan
Republic of China
1969

Master of Science
Northeast Louisiana University
Monroe, Louisiana
1972

Master of Science
Oklahoma State University
Stillwater, Oklahoma
1974

Submitted to the Faculty of the Graduate College
of the Oklahoma State University
in partial fulfillment of the requirements
for the Degree of
DOCTOR OF PHILOSOPHY
July, 1975

EFFECT OF RADIATION INDUCED DEFECTS ON THE

OPTICAL TRANSITIONS OF 3-d IMPURITIES

Thesis Approved:

W. A. Sibley
Thesis Adviser

Richard C. Powell

Larry E. Halliburton

Gilbert J. Mains

Joel J. Martin

N. B. Newton
Dean of the Graduate College

ACKNOWLEDGEMENTS

The author wishes to express his gratitude and appreciation to his major advisor, Dr. W. A. Sibley, who has provided guidance and help throughout the entire research.

Appreciation is also acknowledged to Drs. S. I. Yun, W. E. Vehse, R. C. Powell, and L. E. Halliburton for many valuable suggestions and discussions and to National Science Foundation for financing this work.

Thanks are also extended to Drs. C. T. Butler and J. J. Martin for their assistance in growing crystals and to Mrs. Janet Sallee for typing this manuscript.

Finally, I would like to express my deep gratitude to my wife, Esther, who has lent me great help and shown appropriate encouragement throughout the entire work and to my grandmother and parents for their financial and spiritual support.

TABLE OF CONTENTS

LIST OF TABLES

LIST OF FIGURES

LIST OF FIGURES (Continued)

CHAPTER I

INTRODUCTION

The colors of inorganic complex salt containing transition metal ions have attracted the attention of many scientists for a long time. The marked color differences among the various divalent transition metal ions, gives strong evidence that the position and symmetry of the 3d-ion with respect to the ligand plays a fundamental role. Ligands are the atoms, ions, or molecules which are the neighbors of the 3d-ions. Bethe (1) employed group theory to develop ligand field theory and to explain why the degeneracies of the electronic terms of the free ions are removed in crystal fields of cubic or lower symmetry.

Schlapp and Penney (2) and Van Vleck (3) applied Bethe's theory to explain the magnetic properties of these solids. Subsequently, Van Vleck (4) displayed the connection between Pauling's valence band theory and the crystal field theory. Van Vleck (5) and Finkelstein and Van Vleck (6) were the first to apply crystal field theory to optical spectra of d-electrons in paramagnetic crystals. They studied the visible absorption bands of chromium alum crystal (the so-called ruby) R band and concluded that the energy levels responsible for these bands are the Zeeman split ^2G term of the free Cr^{3+} ion.

Hartman, Schlaefer, and Ilse (7-9) used crystal field theory to calculate the energy levels of 3-d transition metal ions which have no more than five d-electrons. Further theoretical work was done by Orgel

(10-12), Tanabe and Sugano (13), Jorgensen (14,15), Ballhausen (16,17), and Owen (18) over the last two decades. These people have done an excellent job in building a base of knowledge of 3-d transition ions.

Optical properties of Ni, Mn, and Co transition ions in the perovskite structure, shown in Figure 1, have been studied by numerous researchers. Knox and others (19) were the first to study $KNiF_3$ and $KMgF_3$:Ni crystals. They were mainly interested in crystal field strength. It was discovered that the absorption spectra of $KNiF_3$ and $KMgF_3$:Ni at low temperatures showed some very narrow lines (fine structure). A series of papers reported this discovery (20-22) and Liehr and Ballhausen (23) developed spin-orbit ligand field matrices to show that the fine structure was due to the ground state of all components of the ^3F, ^1D, and ^3P terms of Ni^{2+} ions. Mehra and Venkatewarlu (24) and others (12,13,25) studied the absorption spectra of $KMnF_3$ and $RbMnF_3$. The emission spectra of Mn^{2+} ions in $KMnF_3$ and other crystals were investigated by Holloway, et al. (26), and by Klassens, et al. (27). They studied the intensity of emission bands and found that it was strongly dependent on temperature. A group of scientists, among them Ferguson (28), engaged in studies of the absorption of $KCoF_3$ and $KMgF_3$:Co. They calculated the energy levels of Co^{2+}, using the strong field matrices of Einstein (29). They determined that the spin-orbit splitting of ground state was 1000 cm^{-1}. Nesterova et al. (30) have observed absorption bands in the infrared region from $NaCoF_3$, $KCoF_3$, and $RbCoF_3$, but detailed analyses of the bands have not been made.

For substitutional 3-d impurities in $KMgF_3$ crystals, the optical transitions are symmetry forbidden since the 3-d ions have octahedral symmetry, as shown in Figure 1, and some of the transitions are also

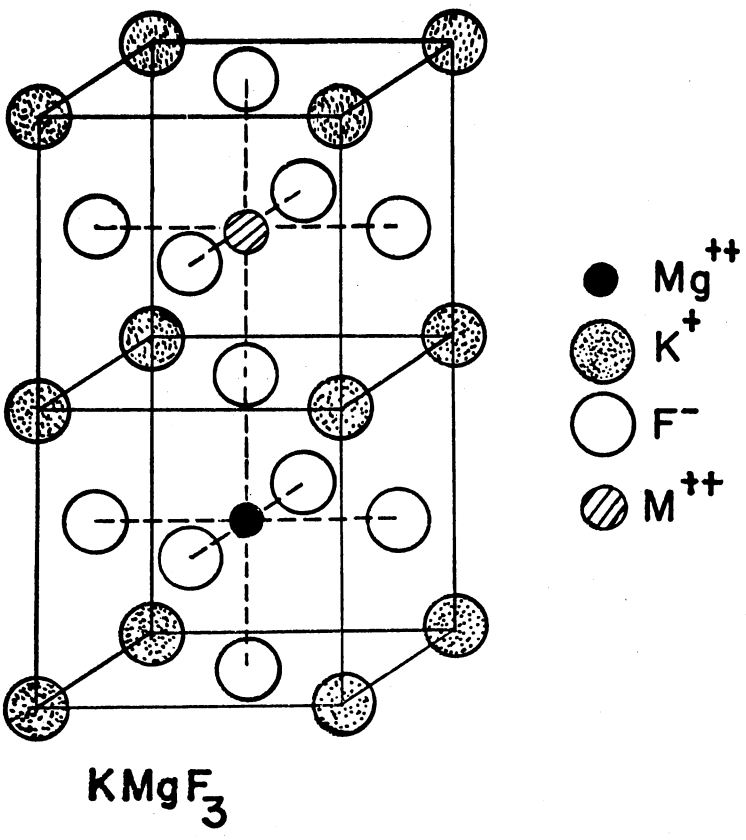

Figure 1. Perovskite Structure $KMgF_3:M^{2+}$(3d)

spin forbidden. When an impurity pair, such as Mn and Cu, Mn and Ni, ... etc., is present, the spin forbiddenness is lifted by the interaction between the pair so that the intensity of optical transition of spin forbiddenness increases by several orders of magnitude. Of course, pair spectra only occur in heavily doped crystals containing about 1-2 at. % impurity. Likewise, if an F center--a negative-ion vacancy with a trapped electron--is present next to a 3-d impurity, an increase in the oscillator strength should be observable since the local symmetry changes to C_{4v}, as shown in Figure 2, and an exchange interaction between the F center and impurity electrons exists.

F centers and other color centers can be produced by the following methods: additive coloration (38-41), electrolytic coloration (38,42-44), ionizing or particle radiation (electrons, protons, x-rays, and neutrons) (45,46). Seitz (47,48), Schulman and Compton (49), Compton and Rabin (50), Fowler (51), and Crawford and Slifkin (52) have given excellent reviews on the subject of color centers.

Color centers have been studied intensively since the early nineteenth century. From time to time, many models of color centers have been proposed by various investigators (47,48,53,54). In 1937, de Boer (55) proposed a F center model which consisted of an electron trapped at the position of a halogen ion vacancy. This model has been examined and proved to be correct by many ESR and ENDOR experiments (52). The nomenclature for color centers can be complicated and sometimes leads to confusion among the researchers. Sonder and Sibley (45) have suggested a generalized nomenclature for color centers. They reserved the F center for negative-ion vacancies containing the same number of electrons as the charge of normal lattice ion. The F_2 center consists of

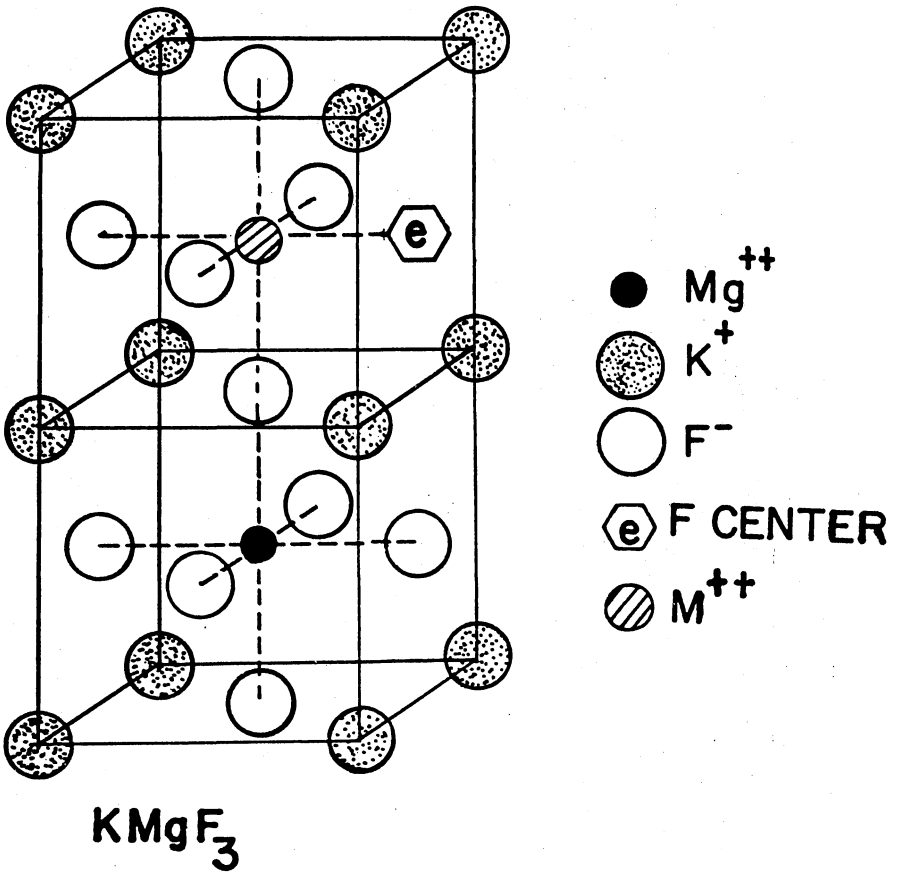

Figure 2. $KMgF_3:M^{2+}$(3d)-F Center Configuration

two adjacent F centers, and F_3 center is formed by three adjacent F centers. The self-trapped hole center, V_k or X_2^-, consists of a hole which is self-trapped on two adjacent anions.

Radiation induced defects in $KMgF_3$ crystals have been studied. Using electron spin resonance and polarized luminescence, Hall and Leggeat (56) tentatively identified F, F_2, and V_k center absorption bands. Riley, Yun, and Sibley (57-60), by means of polarized bleaching method and excitation spectrum, identified F, F_2, F_3, and V_k center absorption bands and F_2 and F_3 emission bands. More extensive studies on V_k centers in electron irradiated $KMgF_3$ have been done by Lewis et al. (16). The ESR spectrum of sodium perturbed H centers in irradiated $KMgF_3$ has been studied by Roads et al. (62,63). Alcala, Koumvakalis, and Sibley (64) observed the emission from the recombination of electrons with V_k centers in irradiated $KMgF_3$.

Vehse and Sibley (65) observed a series of optical absorption bands in 80^oK electron irradiated Mn-doped $KMgF_3$ crystals. They concluded that a F center-Mn complex was responsible for the occurrence of these bands and were able to optically bleach the center with polarized light to produce a dichroism which indicated that the defect orientation was <100> . Sibley, Yun, and Vehse (66) found an emission band in 80^oK electron irradiated Mn-doped $KMgF_3$ crystals. The excitation spectrum of this emission band and the absorption spectrum were almost the same which indicated that the optical bands were due to perturbed Mn^{2+} ions. They tentatively proposed that the model for this defect center was an Mn^{2+}-F center-Mn^{2+} complex. One interesting aspect of their investigations was the observation of large oscillator strength increases for previously forbidden transitions when radiation defects are present. Since the

forbidden transitions are both spin and parity forbidden in Mn-doped $KMgF_3$ crystals, the presence of nearby defects results in symmetry change and hence selection rule change. Exchange between the radiation damage defects and the transition metal ion impurities can also affect the intensity of the optical transitions. Even in the ground state, the F center has a rather extended wave function compared to a fluorine ion, which should lead to large exchange interactions. An investigation of whether symmetry or exchange effects cause the enhanced intensity for the optical transitions seems in order.

Simkin and Aked (67,68) studied optical absorption bands in irradiated Co-doped $KMgF_3$ crystals and pointed out that the valence state of cobalt remained two plus after gamma irradiation at 300K.

Ralph and Townsend (69) in their study of $MgO:Ni^{2+}$ reported an emission band at about 13,000 cm^{-1} which they attributed to a $^3T_{1g} \rightarrow {}^3A_{2g}$ transition. Yun, Kappers, and Sibley (70) observed the same band in $MgF_2:Ni^{2+}$; and on the basis of optical excitation experiments, they suggested a different assignment. The assignment of this transition needs to be verified by more experiments.

The object of this work is therefore threefold:

(1) to identify the emission band at about 13,000 cm^{-1} of Ni^{2+} ions and to study the radiation effect on this emission band,

(2) to present the models for the radiation mechanism of Mn^{2+} and Co^{2+} doped $KMgF_3$ crystals, and

(3) to study the mechanism which causes the enhanced intensity for the optical transitions of Mn^{2+} and Co^{2+} ions in irradiated $KMgF_3$ crystals.

CHAPTER II

CRYSTAL GROWTH

Apparatus

Crystals of $KMgF_3$ doped with Mn, Co, and Ni were grown in the Oklahoma State University crystal growth laboratory by means of modified Bridgman (71) and Stockbarger techniques (72,73). The principle of the technique lies in the change of the temperature. A material contained in a suitable crucible is slowly lowered from a region in which the temperature is slightly above the melting point of the material into another region in which the temperature is below the melting point of the material. The temperature gradient is shown schematically in Figure 3. The crucible is placed in an immobile vacuum system which is surrounded by a furnace. Though it is apparent that the temperature effect is the same for both raising the furnace and lowering the crucible, raising the furnace is much easier than lowering the crucible.

Figure 4 is a schematic showing the main components of the Oklahoma State University Bridgman Apparatus which provides with an adequate temperature gradient to allow the crystal to grow. The crucible containing the chemicals is placed in a graphite heat sink at the bottom of an Al_2O_3 vacuum tube. A small furnace around the tube is raised up to move the temperature gradient of the crucible. The crucible and the heat sink were purchased from Ultra Carbon (UT-9 grade) and the Al_2O_3 vacuum tube was purchased from Coors Mullite. The inside diameter of the graphite

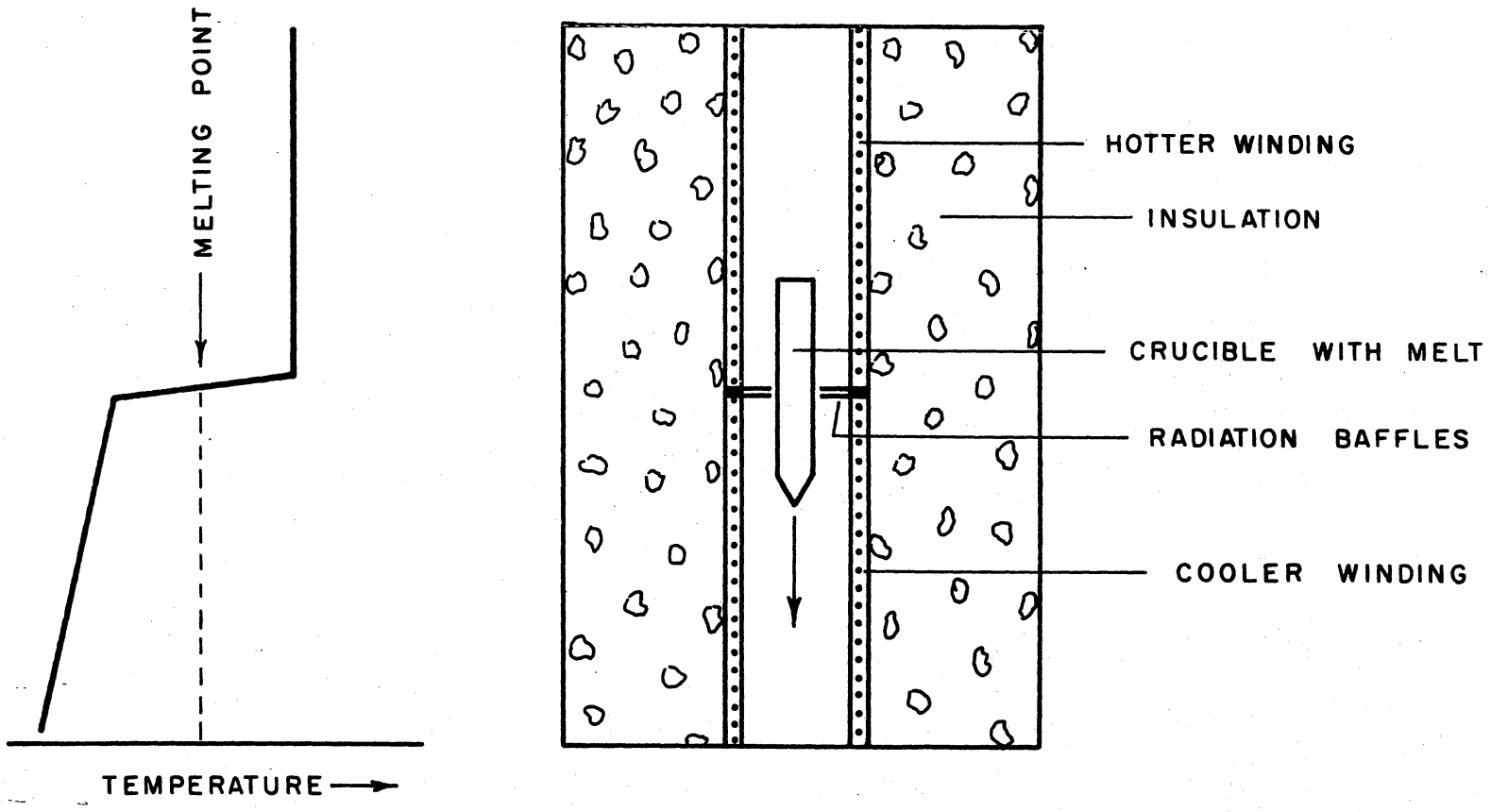

Figure 3. Schematic Bridgman Apparatus With Idealized Temperature Profile

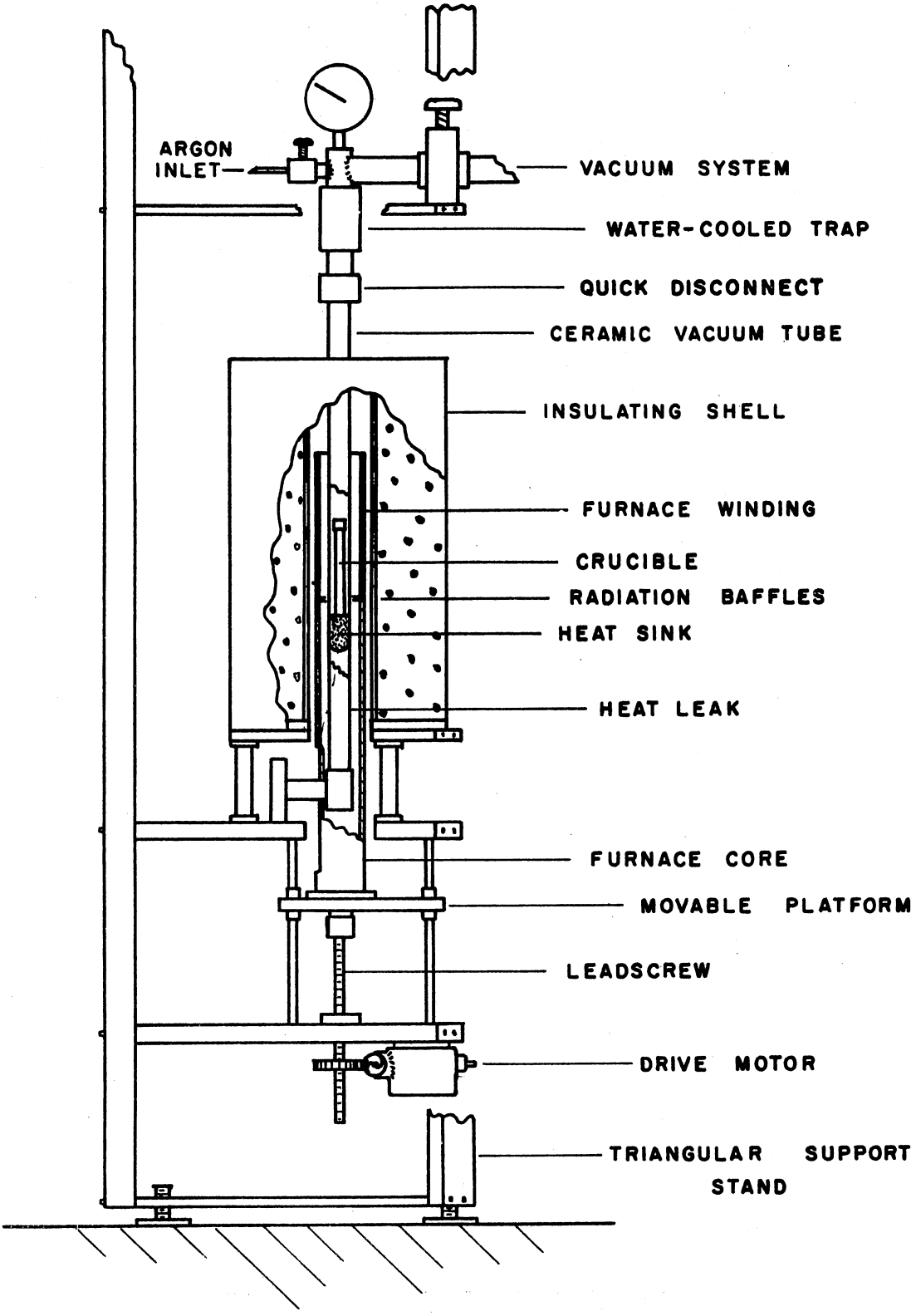

Figure 4. The OSU Bridgman Apparatus

crucible is 1.25 cm, and the length is approximately 16 cm. The tube has an outside diameter of 3.8 cm and inside 3.2 cm. It is 76 cm long; one end is round and closed.

A platinum wire which is approximately 12 meters long and has a diameter of .810 mm (0.0319"), is used to provide the high temperatures which are required for growing higher melting point fluorides. Figure 5 shows details of the platinum-wound furnace. The wire is coiled around a Norton high-purity alumina core. Region A, as shown in Figure 5, is wound at 6 turns per inch (2.36 turns per cm), region B at 3 turns per inch, and region C at 2 turns per inch. This winding pattern results in a nearly uniform temperature profile for the furnace.

The vacuum system for the apparatus consists of a T-M Vacuum Products 200 l/s diffusion pump and a Welch 3 l/s forepump. This system is able to reduce the pressure in the tube from a cold start to 10^{-6} Torr in five minutes. A bourdon gauge calibrated from -1 to +2 atmospheres is employed to monitor the Argon pressure. Moving the inner furnace can be raised at speeds of 1.5, 0.76, 0.30, 0.15, 0.08, or 0.03 cm/hr and the raising mechanism has a maximum travel of 23 cm. A limit switch is set capable of stopping the system at any desired point.

Growth Procedure

Doped potassium magnesium fluoride crystals were grown from a stoichiometric mixture of Harshaw zone-refined crystal pieces of potassium fluoride and magnesium fluoride and Research Organic/Inorganic Chemical Corp. 3-d fluoride (CoF_2, NiF_2, $KMnF_3$) powder which were mixed and placed into a graphite crucible containing approximately 1 mm^3 of anhydrous ammonium bifluoride. The ammonium bifluoride decomposed at

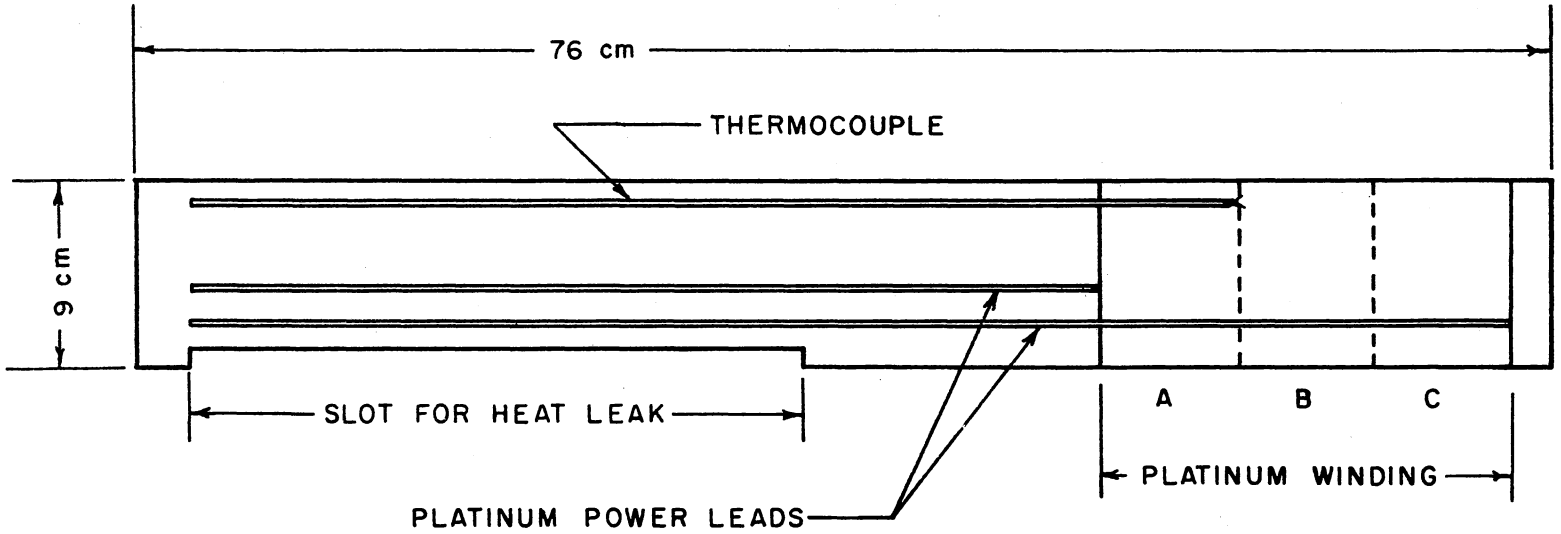

Figure 5. Details of the Platinum-Wound Furnace

about 200°C, releasing hydrogen fluoride gas which flushed some of the absorbed water out of the system. A screw cap, having a small hole to relieve the pressure inside the crucible, was placed on the crucible, and the assembly, in its heat sink, was inserted into the Al_2O_3 tube. The Al_2O_3 tube was connected to the pumping system by means of a quick disconnect vacuum connector, axially aligned. The components of the starting materials were weighed in a dry box. The system was pumped very slowly so that escaping gases from the graphite crucible did not force any of the powder through the small hole of the cap. After 50 microns pressure was obtained through the forepump, the diffusion pump was turned on. When the pressure reached between 15 and 30 microns, the furnace, which was in its lowest position, was turned on at a set temperature (350°C) and was maintained at this temperature while the diffusion pump was on for about 10 hours. After this initial out-gassing procedure, the vacuum tube was alternately filled with Argon and evacuated several times to displace unwanted gases. After the final evacuation, the tube was filled with Argon at the gauge pressure of 700 torr. The temperature was set at 750°C. Approximately 5 hours later, the set point was raised to 1160°C. This temperature was held for about 5 more hours, after which the furnace was moved to pass the graphite crucible at the speed of 1.5 centimeter per hours.

After the furnace had traveled to its maximum distance, the furnace tube was flushed with Argon gas at least three times and then filled with Argon gases at the pressure of 1,200 torr. The furnace was then reset to its starting position. The temperature was reset in four successive steps to minimize thermal shock which would crack the furnace tube. When the thermal equilibrium was again established after about 5

hours, the system was then ready to start the growth procedure. The furnace was raised at the rate of 1.5 millimeter per hour. With the completion of the maximum travel (23 cm) of the furnace, its temperature was lowered through several steps in order to avoid cracking of the furnace tube. When the temperature of the furnace reached 900^{o}C, the pressure of the system was reduced to 150 torr. After reaching room temperature, the furnace tube was removed from the system. Usually, the bottom nine-tenths of the material removed from the graphite crucible was single crystal and the top one-tenth polycrystalline potassium magnesium fluoride. Each crystal was assigned a serial number indicating the date growth began: for example, crystal 072373 started to grow on July 23, 1973. An impurity analysis was made by means of mass-spectroscopy and the results are shown in Table I.

TABLE I

IMPURITY ANALYSIS OF SAMPLES ($\frac{\mu g}{g}$)

	$KMgF_3$:Mn	$KMgF_3$:Co
Ag	10	<1
Al	2000	100
Au	<5	<5
B	<1	<1
Ba	25	<2
Be	<.5	<.5
Bi	<2	<2
Ca	75	<10
Cd	<2	<2
Co	<5	150
Cr	<2	4
Cu	<1	1
Fe	200	4
Ca	11	<1
Ge	<2	<2
Hg	<5	10
Gd	<5	<5
Eu	<5	<5
Li	15	40
Mn	4000	~1
Mo	<1	2
Na	600	700
Nb	<10	<10
Ni	<5	~5
Pb	<1	<1
Pt	<5	<5
Rb	100	90
Sb	<10	<10
Si	10	20
Sn	<2	<2
Sr	75	<25
Ti	40	20
V	<5	<5
W	<5	<5
Zn	<200	<200
Zr	<5	<5

CHAPTER III

THEORY

Crystal Field Theory

Octahedral Potential Energy

The wavefunctions of transition metal ions in octahedral crystal field can be obtained by linearly combining 3-d wavefunctions of a Hydrogen atom which is placed in octahedral crystal field. In this section, 3-d wavefunctions and associated energy states of the electron of the Hydrogen atom are calculated.

A hydrogen atom is surrounded by six negative point charges which locate at the vertices of a regular octahedron. The potential energy of the electron of the hydrogen atom due to the octahedron of the six point charges is given as

$$V(x,y,z) = \sum_{i=1}^{6} V(i,x,y,z) = \sum_{i=1}^{6} \frac{eZ}{r_{ij}}, \qquad (1)$$

where r_{ij} is the distance from ith point charge to the position (x,y,z) of the electron. The inverse of the distance, r_{ij}, can be expanded in terms of spherical harmonic coordinates as

$$\frac{1}{r_{ij}} = \sum_{n=o}^{\infty} \sum_{m=-n}^{n} \frac{4\pi}{2n+1} \frac{r_<^n}{r_>^n} Y_{n_i}^m Y_{n_i}^{m*} \qquad (2)$$

The potential energy within the octahedron of the point charges was calculated. The distance $r_<$ is r, the distance from the origin to the position of the electron, and the distance $r_>$ can be written as a, the distance between the origin and point charges. Equation (1) may now be rewritten in the following form.

$$V(x,y,z) = \sum_{i=1}^{6} eZ \left(\sum_{n=o}^{\infty} \sum_{m=-n}^{n} \frac{4\pi}{2n+1} \frac{r^n}{a^{n+1}} Y_n^m Y_{ni}^{m*} \right) \qquad (3)$$

Since the positions of the six point charges are localized, the function Y_{ni}^{m*} becomes a single number. The contribution from odd n to V(x,y,z) is zero. The above statement can be verified by the following equation.

$$\int_o^{\pi}\int_o^{2\pi} Y_\ell^{m*} Y_n^m Y_\ell^{m_\ell} \sin\theta \, d\phi \, d\theta = 0 \quad (n = \text{odd number})$$

In the case of d wavefunctions, n is not higher than 4. This is because the integrals of spherical harmonics with n' > 2n taken with the product of two spherical harmonics with n must vanish: namely,

$$\int_o^{\pi}\int_o^{2\pi} Y_n^{m*} Y_{n'}^m Y_n^m \sin\theta \, d\phi \, d\theta = 0; \text{ if } n' > 2n$$

Consider the summation of Equation (3) term by term, n = 0; m = 0,

$$\sum_{i=1}^{6} eZ \frac{4\pi}{a} Y_o^o Y_{oi}^{o*} = \frac{eZ4\pi}{a} 2^{-\frac{1}{2}}(2\pi)^{-\frac{1}{2}} \sum_{i=1}^{6} 2^{-\frac{1}{2}}(2\pi)^{-\frac{1}{2}} = \frac{6Ze}{a} \qquad (4)$$

It is found the total contribution to V(x,y,z) from n=0 is $\frac{6Ze}{a}$ · n=2; m=0,

$$\sum_{i=1}^{6} eZ \frac{4\pi r^2}{5a^3} Y_2^o Y_{2i}^{o*} = \frac{eZ4\pi r^2}{5a^3} Y_2^o \sum_{i=1}^{6} \left(\frac{5}{8}\right)^{\frac{1}{2}} (2\pi)^{-\frac{1}{2}} (3\cos^2\theta_i - 1) = 0$$

m=±1,

$$\sum_{i=1}^{6} eZ \frac{4\pi r^2}{5a^3} Y_2^{\pm 1} Y_{2i}^{\pm 1*} = \frac{eZ4\pi r^2}{5a^3} Y_2^{\pm 1} \sum_{i=1}^{6} \left(\frac{5}{16}\right)^{\frac{1}{2}} (2\pi)^{-\frac{1}{2}} \cos\theta_i \sin\theta_i \cdot$$

$$e^{\mp i\phi_i} = 0$$

$m=\pm 2$,

$$\sum_{i=1}^{6} eZ \frac{4\pi r^2}{5a^3} Y_2^{\pm 2} Y_{2i}^{\pm 2*} = \frac{eZ4\pi r^2}{5a^3} Y_2^{\pm 2} \sum_{i=1}^{6} \left(\frac{5}{16}\right)^{\frac{1}{2}} (2\pi)^{-\frac{1}{2}} \sin^2\theta_i \cdot e^{\mp 2\phi_i} = 0$$

The total contribution from n=2 is therefore zero.

n=4; m=0,

$$\sum_{i=1}^{6} eZ \frac{4\pi r^4}{9a^5} Y_4^0 Y_{4i}^{0*} = \frac{eZ4\pi r^4}{9a^5} Y_4^0 \sum_{i=1}^{6} \left(\frac{9}{128}\right)^{\frac{1}{2}} (2\pi)^{-\frac{1}{2}} (35\cos^4\theta_i - 30\cos^2$$

$$\cdot \theta_i + 3) = \left(\frac{49}{18}\right)^{\frac{1}{2}} (2\pi)^{\frac{1}{2}} \left(\frac{Zer^4}{a^5}\right) Y_4^0$$

$m=\pm 1, \pm 2, \pm 3$,

The contribution from these values of m is found to be zero.

$m=\pm 4$,

$$\sum_{i=1}^{6} eZ \frac{4\pi r^4}{9a^5} Y_4^{\pm 4} Y_{4i}^{\pm 4*} = \frac{eZ4\pi r^4}{9a^5} Y_4^{\pm 4} \sum_{i=1}^{6} \left(\frac{315}{245}\right)^{\frac{1}{2}} (2\pi)^{-\frac{1}{2}} \sin^4\theta_i \, e^{\mp 4i\phi_i}$$

$$= \left(\frac{49}{18}\right)^{\frac{1}{2}} (2\pi)^{\frac{1}{2}} \left(\frac{Zer^4}{a^5}\right) \left(\frac{5}{14}\right)^{\frac{1}{2}} Y_4^{\pm 4}$$

The total contribution to V(x,y,z) from n=4 is

$$\left(\frac{49}{18}\right)^{\frac{1}{2}} (2\pi)^{\frac{1}{2}} \left(\frac{Zer^4}{a^5}\right) \left[Y_4^0 + \left(\frac{5}{14}\right)^{\frac{1}{2}} (Y_4^4 + Y_4^{-4})\right] . \qquad (5)$$

The potential energy in the system is then

$$V(x,y,z) = \text{Equation 4} + \text{Equation 5.}$$

Equation (4) is constant; therefore, Equation (5) is responsible for the splitting of the d orbitals. V_{oct} is defined here as that part of $V(x,y,z)$ for an octahedron of charges which leads to the splitting of the d orbitals.

The matrix element of V_{oct} between ϕ_{nlm} state and $\phi_{n'l'm'}$ state is given by

$$\langle\phi_{nlm}|V_{oct}|\phi_{n'l'm'}\rangle = \int d\vec{r}\ \phi^*_{nlm}(\vec{r})\ V_{oct}\ \phi_{n'l'm'}(\vec{r}) \qquad (6)$$

The calculation of the matrix element of d wavefunction is straight forward, and the nonvanishing matrix elements are given as follows:

$$\langle\phi_{nd\pm2}|V_{oct}|\phi_{nd\pm2}\rangle = Dq,$$

$$\langle\phi_{nd\pm1}|V_{oct}|\phi_{nd\pm1}\rangle = -4Dq,$$

$$\langle\phi_{ndo}|V_{oct}|\phi_{ndo}\rangle = 6Dq,$$

$$\langle\phi_{nd\pm2}|V_{oct}|\phi_{nd\mp2}\rangle = 5Dq,$$

where

$$D = 35\,\frac{Ze^2}{4a^5}, \quad q = \left(\frac{2}{105}\right)\langle r^4\rangle_{nd}, \text{ and}$$

$$\langle r^4 \rangle_{nd} = \int_o^\infty R^*_{n,2}\, r^4\, R_{n,2}\, r^2\, dr.$$

The perturbed energies of the 3d-level are given by solving the following secular equation,

$$\begin{vmatrix} Dq-E & 0 & 0 & 0 & 5Dq \\ 0 & -4Dq-E & 0 & 0 & 0 \\ 0 & 0 & 6Dq-E & 0 & 0 \\ 0 & 0 & 0 & -4Dq-E & 0 \\ 5Dq & 0 & 0 & 0 & Dq-E \end{vmatrix} = 0$$

The eigenvalues and eigenfunctions can be found as follows:

$$E = -4\ Dq; \qquad \phi_{3d\ 1}$$

$$\phi_{3d-1}$$

$$2^{-\frac{1}{2}}(\phi_{3d\ 2} - \phi_{3d-2}),$$

$$E = 6\ Dq; \qquad \phi_{3d\ 0}$$

$$2^{-\frac{1}{2}}\ (\phi_{3d\ 2} + \phi_{3d-2}).$$

The eigenfunctions of the E = -4 Dq state are not real numbers. By using the unitary transformation matrix,

$$\begin{bmatrix} i2^{-\frac{1}{2}} & -2^{-\frac{1}{2}} & 0 \\ i2^{-\frac{1}{2}} & 2^{-\frac{1}{2}} & 0 \\ 0 & 0 & -i \end{bmatrix},$$

real wavefunctions for the E = -4 Dq state are obtained as follows:

$$\xi = (i2^{-\frac{1}{2}})\ (\phi_{3d\ 1} + \phi_{3d-1}) = \left(\frac{15}{4\pi}\right)^{\frac{1}{2}} \left(\frac{YZ}{r^2}\right) R_{3d}(r),$$

$$\mu = 2^{-\frac{1}{2}} (\phi_{3d\ 1} - \phi_{3d-1}) = (\frac{15}{4\pi})^{\frac{1}{2}} (\frac{ZX}{r^2}) R_{3d}(r),$$

$$\zeta = -i2^{-\frac{1}{2}} (\phi_{3d\ 2} - \phi_{3d-2}) = (\frac{15}{4\pi})^{\frac{1}{2}} (\frac{xy}{r^2}) R_{3d}(r).$$

The wavefunctions for the E = 6Dq state may be rewritten as follows:

$$u = \phi_{3d\ 0} = (\frac{5}{16\pi})^{\frac{1}{2}} (\frac{3Z^2 - r^2}{r^2}) R_{3d}(r)$$

$$v = (\phi_{3d\ 2} + \phi_{3d-2})2^{-\frac{1}{2}} = (\frac{15}{16\pi})^{\frac{1}{2}} (\frac{x^2-y^2}{r^2}) R_{3d}(r)$$

The d-level of a hydrogen atom splits into a doubly degenerated level and a triply degenerated level in an octahedron crystal field.

Group Theory Considerations

When a hydrogen atom is placed in the octahedral symmetry, as described in the previous section, the Hamiltonian of the electron is no longer invariant under rotations around arbitrary axes by arbitrary angles, but it is invariant under the symmetry operations in the octahedral group. The characters of a reducible representation of d wavefunction can be obtained (74) by

$$\chi(\alpha) = \frac{\sin (2 + \frac{1}{2})\alpha}{\sin \frac{\alpha}{2}} .$$

The calculation of the characters is straightforward. The reducible representation can be shown as

$$\Gamma_d = e_g + t_{2g} .$$

The above equation shows that the five-fold degenerated d wavefunction in free ions does not remain degenerated in octahedral symmetry environment. The wavefunctions are split into a triply degenerate set, t_{2g}, and a doubly degenerate set, e_g. The wavefunctions of the t_{2g} state are ξ, μ, ζ, and the wavefunctions of E_g state are u and v.

Strong Field Scheme

In 1954, Tanabe and Sugano (13) presented the strong field scheme to treat the transition metal ions and to obtain the energy levels of the transition metal ions. They pointed out that the inner shells of 3-d ions in an octahedral field, in many cases, are completely filled with electrons and that ligands have closed-shell configurations with energy lower than those of t_{2g} and e_g shells. Therefore, the states can be obtained by accommodating the 3-d electrons in t_{2g} shells and e_g shells. They used the configurations $e_g^n t_{2g}^{N-n}$ (n = 0 to N) as the starting point for $3d^N$ electron configuration. If the crystal field is very strong, the interaction between these configurations, $e_g^n t_{2g}^{N-n}$, can be neglected. Unfortunately, the crystal field is not sufficiently strong to ensure the neglect of the interaction entirely. By proper linear combinations of the configurations, the states can be constructed and we consider $3d^2$ here as an example to explain the method. The states of $3d^2$ can be obtained by accommodating the two electrons in the t_{2g} shells. If the spin function in the states is considered there are then 15 possible ways to accommodate the two electrons, considering Pauli principle and antisymmetric property. The Slater determinants corresponding to the fifteen states are given as

$$|\xi\mu|,\ |\bar{\xi}\bar{\mu}|,\ |\mu\xi|,\ |\bar{\mu}\bar{\xi}|,\ |\zeta\xi|,\ |\bar{\zeta}\bar{\xi}|,$$

$$|\xi\bar{\mu}|,\ |\bar{\xi}\mu|,\ |\mu\bar{\xi}|,\ |\zeta\bar{\xi}|,\ |\bar{\mu}\xi|,\ |\bar{\zeta}\xi|,$$

$$|\xi\bar{\xi}|,\ |\mu\bar{\mu}|,\ |\xi\bar{\xi}|.$$

$|S\ M\ \Gamma\ \gamma\rangle$ is defined as the wavefunction of $^{2S+1}\Gamma$ term. γ is one of the bases of the irreducible representation Γ, for example $\gamma = \mu, \xi, \zeta$ for $\Gamma = T_{2g}$. For two electrons in t_{2g}, the irreducible representation Γ can be found via the direct product of t_{2g} and t_{2g}.

$$\Gamma = t_{2g} \times t_{2g} = A_{1g} + E_g + T_{1g} + T_{2g}$$

The wavefunction then can be constructed by the linear combination of those 15 Slater determinants.

$$|t_{2g}^2\ S\ M\ \Gamma\ \gamma\rangle = \sum_{\substack{m_1 m_2 \\ \gamma_1 \gamma_2}} |\phi(t_{2g} m_1 \gamma_1)\phi(t_{2g} m_2 \gamma_2)| \langle \tfrac{1}{2}\ m_1\ \tfrac{1}{2}\ m_2 | S\ M\rangle\ \langle T_2 \gamma_1 T_2 \gamma_2 | \Gamma\gamma\rangle$$

where $\langle \frac{1}{2}\ m_1\ \frac{1}{2}\ m_2 | S\ M\rangle$ and $\langle T_2\ \gamma_1\ T_2\ \gamma_2 | \Gamma\gamma\rangle$ are the Clebsch-Gordon coefficient. The wavefunctions are obtained as follows:

$$\phi(t_{2g}^2,\ ^1A_{1g}) = (|\xi\bar{\xi}| + |\mu\bar{\mu}| + |\zeta\bar{\zeta}|)/\sqrt{3},$$

$$\phi(t_{2g}^2,\ ^1E_g u) = (-|\xi\bar{\xi}| - |\mu\bar{\mu}| + 2|\zeta\bar{\zeta}|)/\sqrt{6},$$

$$\phi(t_{2g}^2,\ ^1E_g v) = (|\xi\bar{\xi}| - |\mu\bar{\mu}|)/\sqrt{2},$$

$$\phi(t_{2g}^2,\ ^3T_{1g}\ M = 1\ \gamma) = |\xi\mu|,$$

$$\phi(t_{2g}^2,\ ^3T_{1g}\ M = 0\ \gamma) = (|\xi\bar{\mu}| - |\mu\bar{\xi}|)/\sqrt{2},$$

$$\phi(t_{2g}^2,\ ^3T_{1g}\ M = -1\ \gamma) = |\bar{\xi}\bar{\mu}|,$$

$$\phi(t_{2g}^2,\ ^1T_{2g}\ \zeta) = (|\xi\bar{\mu}| + |\mu\bar{\xi}|)/\sqrt{2}\ .$$

For e_g shells, there are 6 ways to accommodate the two electrons. There are uv, $\bar{u}v$, $u\bar{v}$, $u\bar{u}$, $v\bar{v}$, $\overline{uv}$. The irreducible representations of the two electrons in e_g shells are A_{1g}, A_{2g}, and E_g. The wavefunctions are given by linearly combining those 6 Slater determinants,

$$|e_g^2,\ S\ M\ \Gamma\ \gamma\rangle = \sum_{\substack{m_1 m_2 \\ \gamma_1 \gamma_2}} |\phi(e_g\ m_1\gamma_1)\ \phi\ (e_g m_2\gamma_2)|\langle \tfrac{1}{2}\ m_1\ \tfrac{1}{2}\ m_2|S\ M\rangle\ \langle E\gamma_1 E\gamma_2|\Gamma\ \gamma\rangle$$

The wavefunctions are then obtained as follows:

$$\phi(e_g^2,\ ^1A_{1g}) = (|u\bar{u}| + |v\bar{v}|)/\sqrt{2},$$

$$\phi(e_g^2,\ ^3A_{2g}\ M = 1) = |uv|,$$

$$\phi(e_g^2,\ ^3A_{2g}\ M = 0) = (|u\bar{v}| - |v\bar{u}|)/\sqrt{2},$$

$$\phi(e_g^2,\ ^3A_{2g}\ M = -1) = |\bar{u}\bar{v}|,$$

$$\phi(e_g^2,\ ^1E_g\ u) = (-|u\bar{u}| + |v\bar{v}|)/\sqrt{2},$$

$$\phi(e_g^2,\ ^1E_g\ v) = (|u\bar{v}| + |v\bar{u}|)/\sqrt{2}\ .$$

For one electron in e_g shell and another electron in t_{2g} shell, there are 24 ways to accommodate them. The irreducible representations are T_{1g} and T_{2g}. The wavefunctions are given as

$$|t_{2g}\ e_g,\ S\ M\ \Gamma\ \gamma\rangle = \sum_{\substack{m_1 m_2 \\ \gamma_1 \gamma_2}} |\ \phi(t_{2g} m_1 \sigma_1)\phi(e_g m_2 \sigma_2)|\langle \tfrac{1}{2}\ m_1\ \tfrac{1}{2}\ m_2|S\ M\rangle\langle T_2 \gamma_1 E \gamma_2|\Gamma\gamma\rangle$$

The wavefunctions are then obtained as follows:

$$\phi(t_{2g}e_g,\ ^3T_{1g}\ M = 1\ \gamma) = |\zeta v|,$$

$$\phi(t_{2g}e_g,\ ^3T_{1g}\ M = 0\ \gamma) = (|\zeta\bar{v}| + (\bar{\zeta}v|)|\sqrt{2},$$

$$\phi(t_{2g}e_g,\ ^3T_{1g}\ M = -1\ \gamma) = |\bar{\xi}\bar{v}|,$$

$$\phi(t_{2g}e_g,\ ^3T_{2g}\ M = 1\ \zeta) = |\zeta u|,$$

$$\phi(t_{2g}e_g,\ ^3T_{2g}\ M = 0\ \zeta) = (|\zeta\bar{u}| + |\bar{\zeta}u|)|\sqrt{2},$$

$$\phi(t_{2g}e_g,\ ^3T_{2g}\ M = -1\ \zeta) = (|\zeta\bar{u}|),$$

$$\phi(t_{2g}e_g,\ ^1T_{1g}\ \gamma) = (|\zeta\bar{v}| - |\bar{\zeta}v|)|\sqrt{2},$$

$$\phi(t_{2g}e_g,\ ^1T_{2g}\ \zeta) = (|\zeta\bar{u}| - |\bar{\zeta}u|)|\sqrt{2}\ .$$

The two electron Hamiltonian in octahedral crystal field is given as

$$H = f_1 + f_2 + g_{12} = H_0 + H_1, \ldots\ldots\ldots \quad (6)$$

where $f_i = (2m)^{-1}\ \hat{P}_i^2 + V_{oct}(r_i)$ and $g_{12} = e^2\ r_{12}^{-1}$. By using

$$\sum_{\sigma_1\sigma_2} \int d\tau_1 d\tau_2 |\phi(\lambda_1 m_1 \gamma_1)\ \phi(\lambda_2 m_2 \gamma_2)|^*\ g_{12}\ |\phi(\lambda_1' m_1' \gamma_1')\ \phi(\lambda_2' m_2' \gamma_2')| \quad (7)$$

the matrix of H_1 can be calculated as follows:

$$\langle t_{2g}^2, {}^1A_{1g} \,|g_{12}|\, t_{2g}^2, {}^1A_{2g}\rangle = J(\zeta\xi) + 2K(\xi\mu) = A + 10B + 5C$$

$$\langle t_{2g}^2, {}^1E_g\ u \,|g_{12}|\, t_{2g}^2, {}^1E_g\ u\rangle = J(\zeta\xi) - K(\xi\mu) = A + B + 2C$$

$$\langle t_{2g}^2, {}^3T_{1g}\ M{=}0 \,|g_{12}|\, t_{2g}^2, {}^3T_{1g}\ M{=}0\rangle = J(\xi\mu) - K(\xi\mu) = A - 5B$$

$$\langle t_{2g}^2, {}^1T_{2g}\ \xi \,|g_{12}|\, t_{2g}^2, {}^1T_{2g}\ \xi\rangle = J(\zeta\mu) + K(\xi\mu) = A + B + 2C$$

$$\langle e_g^2, {}^1A_{1g} \,|g_{12}|\, e_g^2, {}^1A_{1g}\rangle = \tfrac{1}{2}(J(uu) + J(vv)) + K(uv) = A + 8B + 4C$$

$$\langle e_g^2, {}^3A_{2g}\ M = 1 \,|g_{12}|\, e_g^2, {}^3A_{2g}\ M = 1\rangle = J(uv) - K(uv) = A - 8B$$

$$\langle e_g^2, {}^1E_g\ u \,|g_{12}|\, e_g^2, {}^1E_g\ u\rangle = \tfrac{1}{2}(J(uu) + (vv)) - K(uv) = A + 2C$$

$$\langle t_{2g}e_g, {}^3T_{1g}\ M = 1 \,|g_{12}|\, t_{2g}e_g, {}^3T_{1g}\ M{=}1\rangle = J(\zeta v) - K(\zeta v) = A + 4B$$

$$\langle t_{2g}e_g, {}^1T_{1g}\ \gamma \,|g_{12}|\, t_{2g}e_g, {}^1T_{1g}\ \gamma\rangle = J(\zeta v) + K(\zeta v) = A + 4B + 2C$$

$$\langle t_{2g}e_g, {}^3T_{2g}\ M{=}1\ \gamma \,|g_{12}|\, t_{2g}e_g, {}^3T_{2g}\ M = 1\ \gamma\rangle = J(\zeta u) - K(\zeta u) = A{-}8B$$

$$\langle t_{2g}e_g, {}^1T_{2g}\ \zeta \,|g_{12}|\, t_{2g}e_g, {}^1T_{2g}\ \zeta\rangle = J(\zeta u) + K(\zeta u) = A + 2C$$

$$\langle t_{2g}^2, {}^3T_{1g}\ M{=}1\ \gamma \,|g_{12}|\, t_{2g}e_g, {}^3T_{1g}\ M{=}1\ \gamma\rangle = \langle \xi u \,|g_{12}|\, \zeta v\rangle - \langle \xi u \,|g_{12}|\, v\zeta\rangle = 6B$$

$$\langle t_{2g}^2, {}^1T_{2g}\ \xi \,|g_{12}|\, t_{2g}e_g, {}^1T_{2g}\ \xi\rangle = \langle \xi\mu \,|g_{12}|\, \zeta u\rangle - \langle \xi u \,|g_{12}|\, u\zeta\rangle = 2\,3^{\frac{1}{2}}B$$

$$\langle t_{2g}^{2},\ {}^{1}A_{1g} \mid g_{12} \mid e_{g}^{2},\ {}^{1}A_{1g} \rangle = \left(\frac{3}{2}\right)^{1/2} (K(\zeta u) + K(\zeta v)) = 6^{1/2}(2B + C)$$

$$\langle t_{2g}^{2},\ {}^{1}E_{g}\ u \mid g_{12} \mid e_{g}^{2},\ {}^{1}E_{g}\ u \rangle = -\left(\frac{3}{2}\right)^{1/2} (K(\zeta u) - K(\zeta v)) = -2\ 3^{1/2}B,$$

where $J(ab) = \langle ab|g_{12}|ab\rangle$, $K(ab) = \langle ab|g_{12}|ba\rangle$. To obtain these results the following relations were used.

$$J(\zeta\zeta) = A + 4B + 3C, \qquad J(uv) = A - 4B + C,$$

$$J(\xi\mu) = A - 2B + C, \qquad K(uv) = 4B + C,$$

$$K(\xi\mu) = 3B + C, \qquad J(\zeta u) = A - 4B + C,$$

$$J(\zeta v) = A + 4B + C, \qquad K(\zeta u) = 4B + C,$$

$$K(\zeta v) = C, \qquad \langle \xi\mu \mid g_{12} \mid \zeta u \rangle = 3^{1/2}B.$$

For energy matrices of $H_o + H_1$, $(-4n+6m)Dq$ must be added to the diagonal element in the state of $t_{2g}^{n}e_{g}^{m}$. The similar calculation can be used to botain the other $3d^{N}$ (N = 2 to 9) energy matrices. The electron configuration of Mn^{2+} is $3d^{5}$, and the spin-quartet energy matrices of Mn^{2+} are obtained as follows:

$$\begin{array}{c} {}^{4}T_{1g}({}^{4}P,\ {}^{4}F,\ {}^{4}G) \\ \left|\begin{array}{ccc} -25B + 6C - 10Dq & 3B2^{1/2} & -C \\ 3B2^{1/2} & -16B + 7C & -3B2^{1/2} \\ -C & -3B2^{1/2} & -25B + 6C + 10Dq \end{array}\right| . \end{array}$$

$$^4T_{2g}(^4F,\ ^4G,\ ^4D)$$

$$\begin{vmatrix} -17B + 6C - 10Dq & -6^{\frac{1}{2}}B & -4B - C \\ -6^{\frac{1}{2}}B & -22B + 5C & -6^{\frac{1}{2}}B \\ -4B - C & -6^{\frac{1}{2}}B & -17B + 6C + 10Dq \end{vmatrix},$$

$$^4E_g(^4D,\ ^4G)$$

$$\begin{vmatrix} -22\ B + 5C & -2B3^{\frac{1}{2}} \\ -2B3^{\frac{1}{2}} & -21B + 5C \end{vmatrix},$$

$$^4A_{1g}(^4G) \quad -25B + 5C,$$

$$^4A_{2g}(^4F) \quad -13B + 7C,$$

$$^6A_{1g}(^6S) \quad -35B \quad .$$

The electron configuration of Co^{2+} is $3d^7$, and the energy matrices of Co^{2+} are obtained as follows:

$$^2T_{2g}(a^2D,\ b^2D,\ ^2F,\ ^2G,\ ^2H)$$

$$\begin{vmatrix} 5C + 12Dq & -3B3^{\frac{1}{2}} & -5B3^{\frac{1}{2}} & 4B + 2C & 2B \\ -3B3^{\frac{1}{2}} & -6B + 3C + 2Dq & 3B & -3B3^{\frac{1}{2}} & -3B3^{\frac{1}{2}} \\ -5B3^{\frac{1}{2}} & 3B & 4B + 3C + 2Dq & -3^{\frac{1}{2}}B & 3^{\frac{1}{2}}B \\ 4B + 2C & -3B3^{\frac{1}{2}} & -3^{\frac{1}{2}}B & 6B + 5C - 8Dq & 10B \\ 2B & -3B3^{\frac{1}{2}} & 3^{\frac{1}{2}}B & 10B & -2B + 3C - 8Dq \end{vmatrix},$$

$$^2T_{1g}(^2P,\ ^2F,\ ^2G,\ ^2H)$$

$$\begin{vmatrix} -6B+3C+12Dq & -3B & 3B & 0 & -2B3^{\frac{1}{2}} \\ -3B & 3C+2Dq & -3B & 3B & 3B3^{\frac{1}{2}} \\ 3B & -3B & -6B+3C+2Dq & -3B & -3^{\frac{1}{2}}B \\ 0 & 3B & -3B & -6B+3C-8Dq & 2B3^{\frac{1}{2}} \\ -2B3^{\frac{1}{2}} & 3B3^{\frac{1}{2}} & -3^{\frac{1}{2}}B & 2B3^{\frac{1}{2}} & -2B+3C-8Dq \end{vmatrix},$$

$$^2E_g(a^2D,\ b^2D,\ ^2G,\ ^2H)$$

$$\begin{vmatrix} -6B+3C+12Dq & -6B2^{\frac{1}{2}} & -3B2^{\frac{1}{2}} & 0 \\ -6B2^{\frac{1}{2}} & 8B+6C+2Dq & 10B & 3^{\frac{1}{2}}(2B+C) \\ -3B2^{\frac{1}{2}} & 10B & -B+3C+2Dq & 2B3^{\frac{1}{2}} \\ 0 & 3^{\frac{1}{2}}(2B+C) & 2B3^{\frac{1}{2}} & -8B+4C-18Dq \end{vmatrix},$$

$$^4T_{1g}(^4P,\ ^4F)$$

$$\begin{vmatrix} -3B + 2Dq & 6B \\ 6B & -12B - 8Dq \end{vmatrix},$$

$$^4A_{2g}(^4F) \qquad -15B + 12Dq,$$

$$^4T_{2g}(^4F) \qquad -15B + 2Dq,$$

$$^2A_{1g}(^2G) \qquad -11B + 3C + 2Dq,$$

$$^2A_{2g}(^2F) \qquad 9B + 3C + 2Dq\ .$$

Spin-Orbit Interaction

As a result of the spin of an electron, there is a magnetic moment associated with the spin. The electron is moving arouns the nucleus with velocity $\bar{V}$ and, therefore, there is a magnetic field associated with this motion. The interaction between these two magnetic fields can be expressed by the term $-(\bar{V} \times \bar{E})/c^2$. $\bar{V}$ can be rewritten as $\bar{P}/m_o$. Thomas (75) and Frankel (76) calculated the spin-orbit energy as

$$\text{Spin-orbit energy} = \xi \, \bar{s} \cdot \bar{\ell} \, .$$

For many-electron atom, the spin-orbit interaction is usually a sum

$$\sum_i \xi_i \, \bar{s}_i \cdot \bar{\ell}_i$$

The spin-orbit Hamiltonian is given by

$$H_{so} = \sum_i \xi(r_i) \, \bar{s}_i \cdot \bar{\ell}_i$$

Therefore, the energy split by spin-orbit interaction can be calculated by quantum mechanics.

As a consequence of the spin-orbit interaction, the irreducible representation of the state can be calculated via direct product of the reducible representation of the spin and the state. In order to understand the energy level split due to the spin-orbit interaction, the Ni^{2+} ion in octahedral symmetry is given as an example. The characters of the reducible representations of s = 0 and s = 1 are presented as follows: (74)

O	E	$6C_4$	$3C_2$	$8C_3$	$6C_2$
s = o	1	1	1	1	1
s = 1	3	1	-1	0	-1

Therefore, the irreducible representation of s = O, Γ_o, equals to A_1, and irreducible representation of s = 1, Γ_1, equals to T_1. The energy level splits of Ni^{2+} states are then displayed as follows:

$$^3A_2, \quad \Gamma_1 \times A_2 = T_1 \times A_2 = T_2$$

$$^3T_2, \quad \Gamma_1 \times T_2 = T_1 \times T_2 = A_2 + T_2 + T_1 + E$$

$$^1E, \quad \Gamma_o \times E = A_1 \times E = E$$

$$^3T_1, \quad \Gamma_1 \times T_1 = T_1 \times T_1 = T_2 + E + T_1 + A_1$$

$$^1T_2, \quad \Gamma_o \times T_2 = A_1 \times T_2 = T_2$$

$$^1A_1, \quad \Gamma_o \times A_1 = A_1 \times A_1 = A_1$$

Configuration Coordinate Model of the Optical Band Shape

The band shape of optical transition can be explained by the configuration coordinate model which derived from the results of the Born-Oppenheimer approximation. The approximation suggests that the wavefunction may be written as

$$\Psi_{nN}(\vec{r}, \vec{R}) = \phi_{n,R}(\vec{r})\, \chi_{nN}(\vec{R}), \tag{8}$$

where n and N are the set of electronic and nuclear quantum numbers,

$\phi_{n,R}(\vec{r})$ is the electronic wavefunction which depends on the nuclear coordinates R, and $\chi_{nN}(\vec{R})$ is nuclear wavefunction which depends only on the electronic quantum numbers and not on the electronic coordinates. Keil (77) presents a linear coupling scheme to solve the problem. The excited state adiabatic is given in terms of the normal mode coordinates and has linear relation with the ground state adiabatic potential. The potentials are

$$E_g(Q) = \tfrac{1}{2}m\omega^2 Q^2$$

and

$$E_e(Q) = E_{ge} + A\hbar\omega \left(\frac{m\omega}{\hbar}\right)^{\frac{1}{2}} Q + \tfrac{1}{2}m\omega^2 Q^2 ,$$

where A is a dimensionless constant which expresses the strength of the electron-phonon interaction, Q is the normal configuration coordinate which is usually chosen to be the totally symmetric mode of the nearest neighbor, and E_{ge} is the potential energy difference between the ground state and excited state at Q = 0. The nuclear wavefunctions for the ground state are obtained as

$$\chi_{g\mu}(\rho) = \left[\frac{(m\omega/\hbar)^{\frac{1}{2}}}{\pi^{\frac{1}{2}} 2^{\mu} \mu!}\right]^{\frac{1}{2}} e^{-\frac{1}{2}\rho^2} H_{\mu}(\rho)$$

where $\rho = \left(\frac{m\omega}{\hbar}\right)^{\frac{1}{2}} Q$ and $H_{\mu}(\rho)$ is a Hermite polynomial. The possible energies of the ground states are

$$\varepsilon_{g\mu} = (\mu + \tfrac{1}{2})\hbar\omega .$$

The wavefunctions for the excited state are found as

$$\chi_{ev}(\rho+A) = \left(\frac{(m\omega/\hbar)^{1/2}}{\pi^{1/2}2^v v!}\right)^{1/2} e^{-\frac{1}{2}(\rho+A)^2} H_v(\rho + A),$$

and energies are

$$\varepsilon_{ev} = (v + \tfrac{1}{2})\hbar\omega + E_{ge} - \frac{A^2}{2}\hbar\omega .$$

From Frank-Condon approximation, the interaction matrix element, $\langle\Psi_{eN}(\vec{r},\vec{R})\,|\bar{M}|\,\Psi_{gN}(\vec{r},\vec{R})\rangle$, can be written as

$$\langle\phi_{e,\rho+A}(\vec{r})\,|\bar{M}|\,\phi_{g,\rho}(\vec{r})\rangle\langle\chi_{ev}(\rho+A)\,|\,\chi_{g\mu}(\rho)\rangle .$$

Therefore, the optical band shape is determined by the overlap integral. $\langle\chi_{ev}(\rho+A)\,|\,\chi_{g\mu}(\rho)\rangle$. Keil shows that the result of this integral is

$$\langle\chi_{ev}(\rho+A)\,|\,\chi_{g\mu}(\rho)\rangle = e^{-A^2/4}\left(\frac{\mu!}{v!}\right)^{1/2}\left(\frac{A^2}{2}\right)^{\frac{1}{2}(v-\mu)} L_u^{v-\mu}\left(\frac{A^2}{2}\right) , \quad (9)$$

where $L_\mu^{v-\mu}(\frac{A}{2})^2$ is the Laguerre polynomial. $S = \frac{A^2}{2}$, where S is the Huang-Rhys factor (78). The normalized transition probability from the ground state to the excited state is then given as

$$P_{v\mu} = |\langle\chi_{ev}|\chi_{g\mu}\rangle|^2 = e^{-S}\left(\frac{\mu!}{v!}\right) S^{(v-\mu)} [L_\mu^{v-\mu}(S)]^2 .$$

At T = O, the only occupied ground level is μ = O, and $L_O(S) = 1$, and the probability for the transition to the vth level of the excited state is

$$P_{vo} = \frac{S^v}{v!} e^{-S} . \quad (10)$$

Therefore, the line shape function is

$$G(\varepsilon) = \sum_{v=0}^{\infty} \frac{e^{-S} S^{v}}{v!} (v\hbar\omega + E_{ge} - S\hbar\omega + \varepsilon) \qquad (11)$$

From the above equation, it can be seen that the absorption spectrum at T = 0 is a series lines at

$$\varepsilon_{v} = E_{ge} - S\hbar\omega + v\hbar\omega \ .$$

The transition at v = 0 is called the zero-phonon line, and v = 1 is the one phonon line. Since $\sum_{v=0}^{\infty} P_{v0} = 1$, the ratio of the area under the zero-line to that of the total band is e^{-S}. The same result can be found for the emission band. At low temperature the emission band consists a series lines at

$$\varepsilon_{\alpha} = E_{ge} - S\hbar\omega + \alpha\hbar\omega \ .$$

$S \leq 6$ is usually considered as a limit to observe such lines. For a broad band, the moment of the band is used to describe the band shape. The Huang-Rhys factor can be related to $W_{\frac{1}{2}}(0)$, full band width at half maximum at T = 0, for large S. For a Gaussian band shape the result is

$$W_{\frac{1}{2}}^{2}(0) = (8 \ln 2) S (\hbar\omega)^{2} \ . \qquad (12)$$

At high temperature ($\rho < S \frac{KT}{\hbar\omega}$), $P_{\mu\nu}$ can be expanded as

$$P_{\mu\nu} \cong (2 S \operatorname{csch} \frac{\gamma}{2})^{-\frac{1}{2}} \exp\left(\frac{(\varepsilon - E_{ge})^{2}}{2\hbar^{2}\omega^{2} S \operatorname{csch} \frac{\gamma}{2}}\right) \ ,$$

where $\gamma = \frac{\hbar\omega}{KT}$. For a Gaussian approximation, the half-width as a func-

tion of temperature is found to be

$$W_{\frac{1}{2}}^2(T) \cong 8 \ln 2 \, h^2 \omega^2 S \operatorname{csch} \frac{\gamma}{2}$$

$$= W_{\frac{1}{2}}^2(0) \operatorname{csch} \frac{\hbar\omega}{2KT} \tag{13}$$

$$\cong W_{\frac{1}{2}}^2(0) \coth \frac{\hbar\omega}{2KT} \, .$$

CHAPTER IV

EXPERIMENTAL PROCEDURE

Two principal radiation damage sources, ^{60}Co gamma rays and 1.5 Mev electrons from a Van de Graaff accelerator at a dose rate of about 1.85×10^{13} Mev/cm^3 sec, were utilized to irradiate the sample. The sample was placed in a cryogenerator manufactured by Cryogenic Technology, Inc., or a cryostat manufactured by the Sulfrian Cryogenic Corporation. In the cryogenerator, the temperature could be controlled between 15 and 300 K to ± 1K by a electric heater. The temperature was measured by a thermocouple (number 36 gauge gold: 0.7 at. % iron versus chromel P wire.) A nearly one millimeter thick sample was cut by an IMANCO Macrotome diamond saw and then polished on a Syntron LP-01 vibratory polisher with a Linde Al distilled water slurry. Before polishing by the vibratory polisher, the sample was polished by hand lapping on a glass plate with number 600 carborundum grit and mineral oil. The faces of the sample were checked by a Laue X-ray back reflection machine was {100} planes.

Optical absorption was measured by a Cary 14 spectrophotometer which recorded the optical density as a function of wavelength. The optical density, O.D. = $\log_{10} (I_0/I)$, is related to the absorption coefficient, α, by $\alpha = 2.303 \times (O.D.)/t$, where t is the thickness of the sample. Using a micrometer, several portions of the sample were measured to determine its thickness.

A block diagram of the luminescence apparatus is shown in Figure 6. A 75 w short arc Xenon lamp, manufactured by PEK, Inc., was used as an excitation source. The exciting light passed through a Spex Minimate 22 cm monochromator and was chopped at a frequency of 450 Hz with a Keithley Model 8403-450 light chopper. The sample was rotated slightly off a 45^{o} angle to minimize the reflection of exciting light into the detection system. The detection system consisted of a RCA C 31034 photomultiplier tube mounted to a one-meter Jarrell-Ash monochromator with a dispersion of 8.20 A/mm. The phototube was cooled to $-20^{o}C$ by a cooler manufactured by Products for Research, Inc., and was operated at 1,800 V DC. The output from this phototube was connected to the input of a Keithley Model 427 current amplifier, the output of the current amplifier was then connected to the input of a Keithley Model 840 lock-in amplifier. A reference signal for the lock-in amplifier was taken from the chopper. The luminescence intensity was plotted on a Moseley Model 7001 A X-Y Recorder. The detection system was calibrated by a standard quartz-iodine lamp with a calibration data supplied by the National Bureau of Standards. The response factor of the luminescence detection system after the calibration is shown in Figure 7. The spectral intensity of the PEK X-75 Xenon short arc lamp is presented in Figure 8. The optical excitation spectrum for the luminescence band was taken with the same apparatus described before. The exciting light was varied by a synchronous motor drive which was connected with the grating of the Spex Minimate 22 cm monochromator. The intensity of the excitation spectra were corrected for the intensity spectrum of X-75 lamp.

For low temperature measurements the sample was mounted either in the Sulfrian cryostat or in the cryogenerator. The cryostat and the

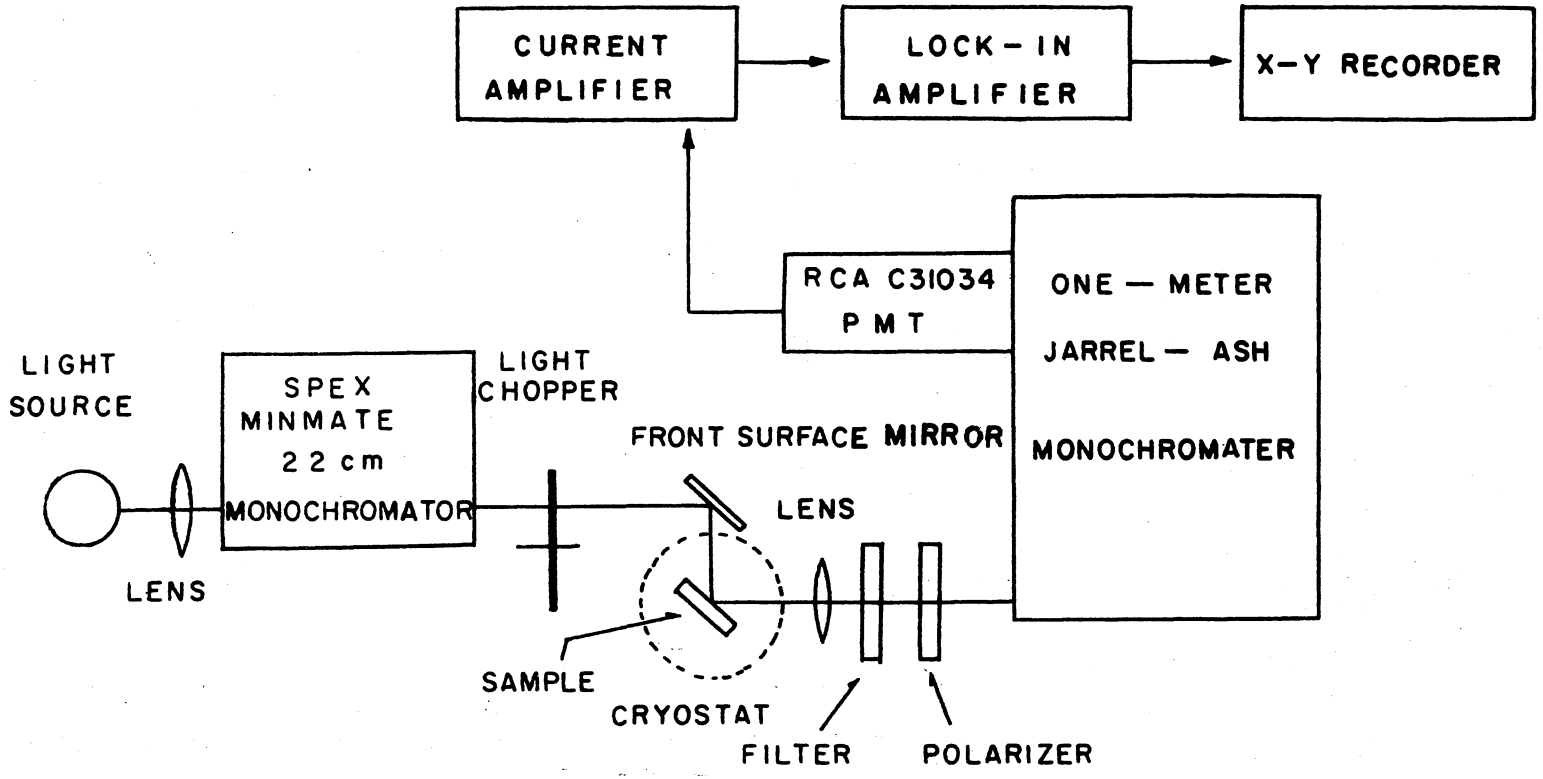

Figure 6. Block Diagram of Luminescence Apparatus

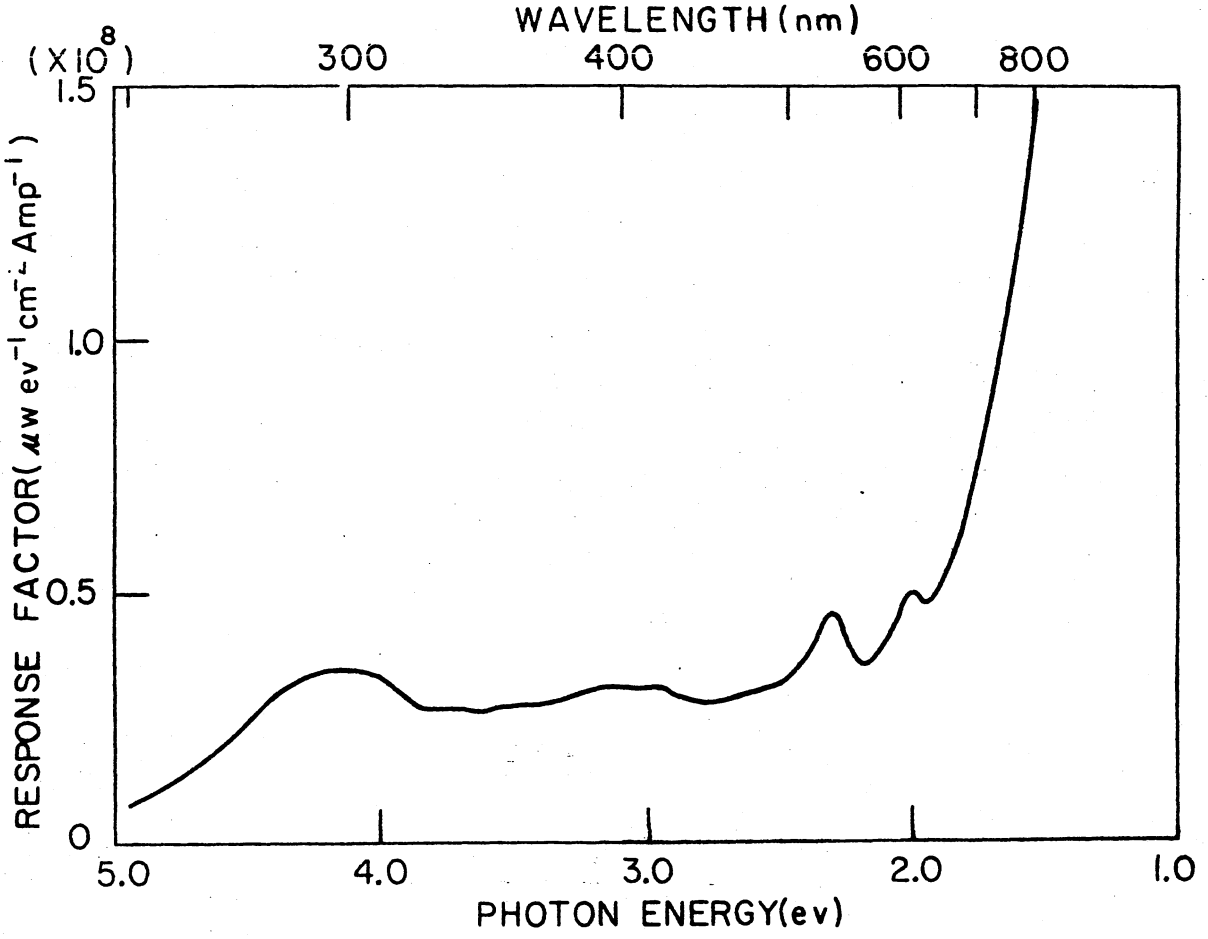

Figure 7. Response of Luminescence Detection System as a Function of Photon Energy

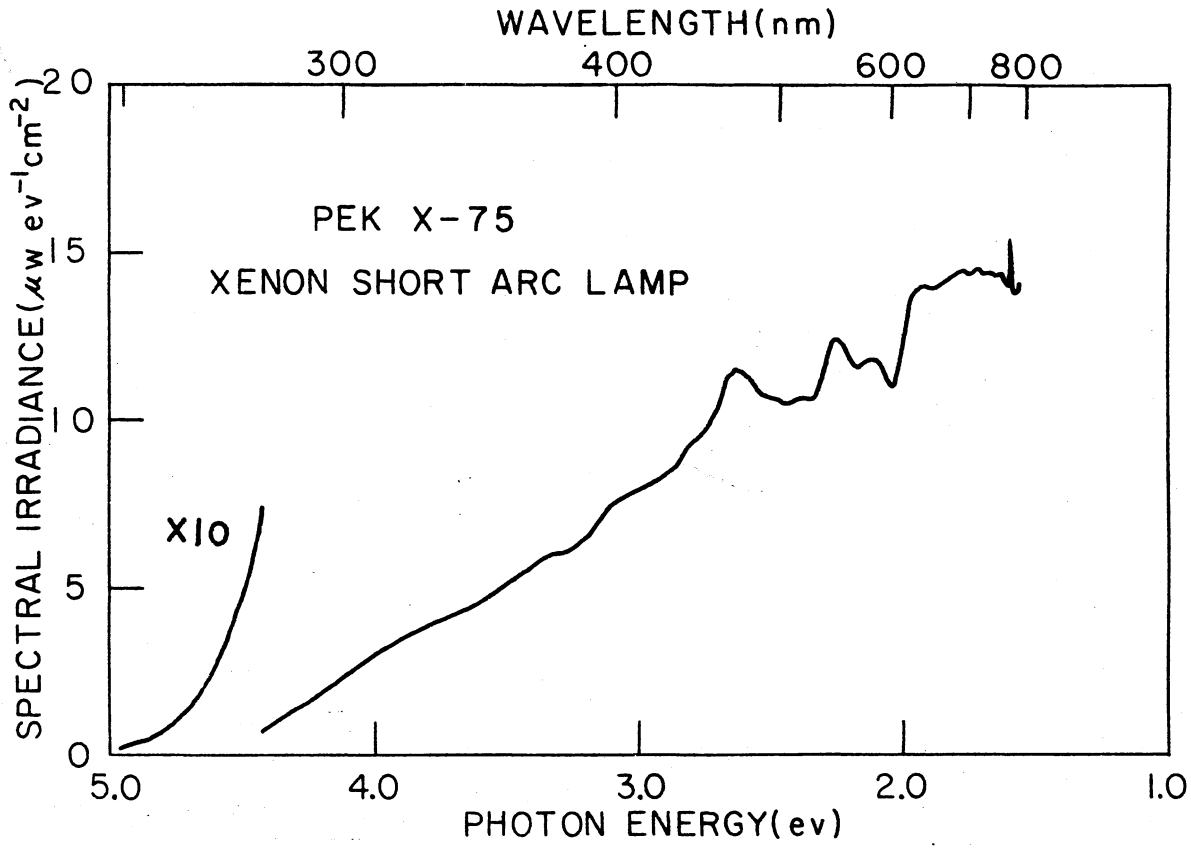

Figure 8. Spectral Output of PEK-75 Xenon Short Arc Lamp as a Function of Photon Energy

cryogenerator were equipped with a rotatable tail section with quartz windows for optical measurement and aluminum windows for irradiation.

Below room temperature, two types of annealing experiments were conducted. For continuous annealing, an electric heater was used to quickly warm the sample to the desired temperature. The sample was maintained at that temperature; an optical spectrum was recorded. For pulse annealing, an optical spectrum was originally recorded at 15 K; then the electric heater was used to quickly warm the sample to the desired temperature which was maintained for ten minutes. The sample was then quenched to 15 K; and the optical spectrum was recorded. Above room temperature, a furnace capable of holding the temperature of the sample stable up to 1,300 K was used to heat the sample to obtain the desired temperature. After that temperature had been maintained for ten minutes, the sample was removed and quenched on a brass block at room temperature. The optical spectrum was then recorded.

The polarized spectrum was obtained through using Polaroid Type NHP'B unsupported polarized sheets. Optical bleaching was accomplished by either a 300 w mercury lamp together with a filter transmitting light from 200 nm-400 nm or the lamp without filter.

CHAPTER V

OPTICAL TRANSITIONS OF 3-d IMPURITIES

Ni^{2+} Emission Bands

Results

Two emission bands, were observed in unirradiated $KMgF_2$:Ni samples. The same green emission band as well as the near infrared emission band were examined in three other different host crystals: the cubic crystals MgO, $KZnF_3$ and the rutile crystal MgF_2. The emission spectra are shown in Figures 9-12. The spectra of $KMgF_3:Ni^{2+}$ and $KZnF_3:Ni^{2+}$ are very similar. The structures of $KMgF_3$ and $KZnF_3$, except for lattice size, are identical. The Ni^{2+} ions in MgO, $KZnF_3$, and $KMgF_3$ hosts occupy a site of O_h symmetry. The spectra for these three hosts consist of two bands, one in the 13,000 cm^{-1} to 14,000 cm^{-1} range and the other in the 20,000 cm^{-1} to 21,000 cm^{-1} range. In all three cases, the lower energy spectrum has much more structure than the higher energy band. In these hosts a sharp line, having a full width at half maximum $\simeq$ 2 cm^{-1}, is observed on the high energy edge of the 13,000 cm^{-1} band.

The spectra for $MgF_2:Ni^{2+}$ are shown in Figure 12. Since the Ni^{2+} ion occupies a site of D_{2h} symmetry in this crystal, it is possible to observe polarization effects by judicious orientation of the crystal. The spectra labeled σ and π refer to those spectra taken with the propagation vector of the emitted light perpendicular to the crystal optic

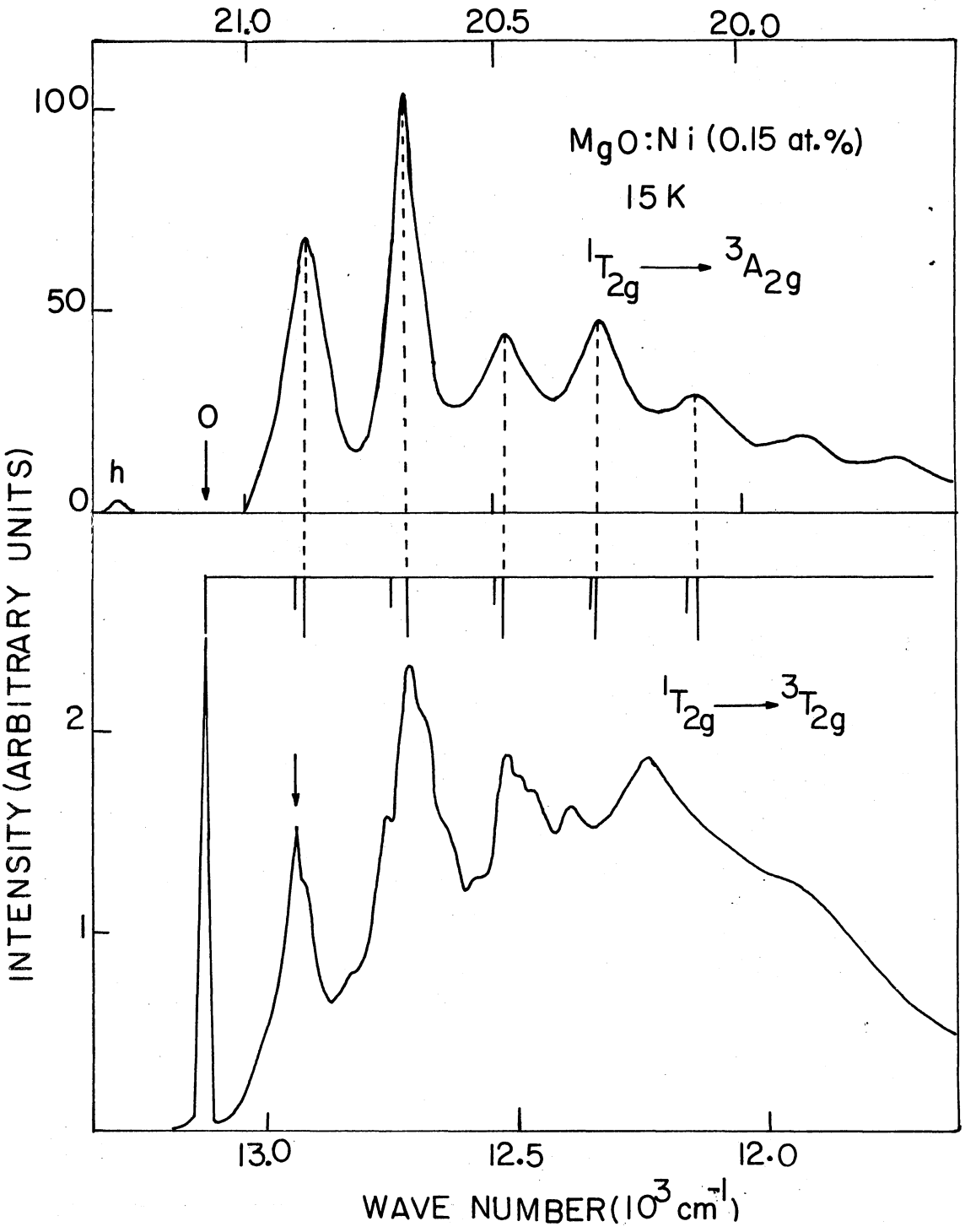

Figure 9. Emission Bands for MgO:Ni at 15 K

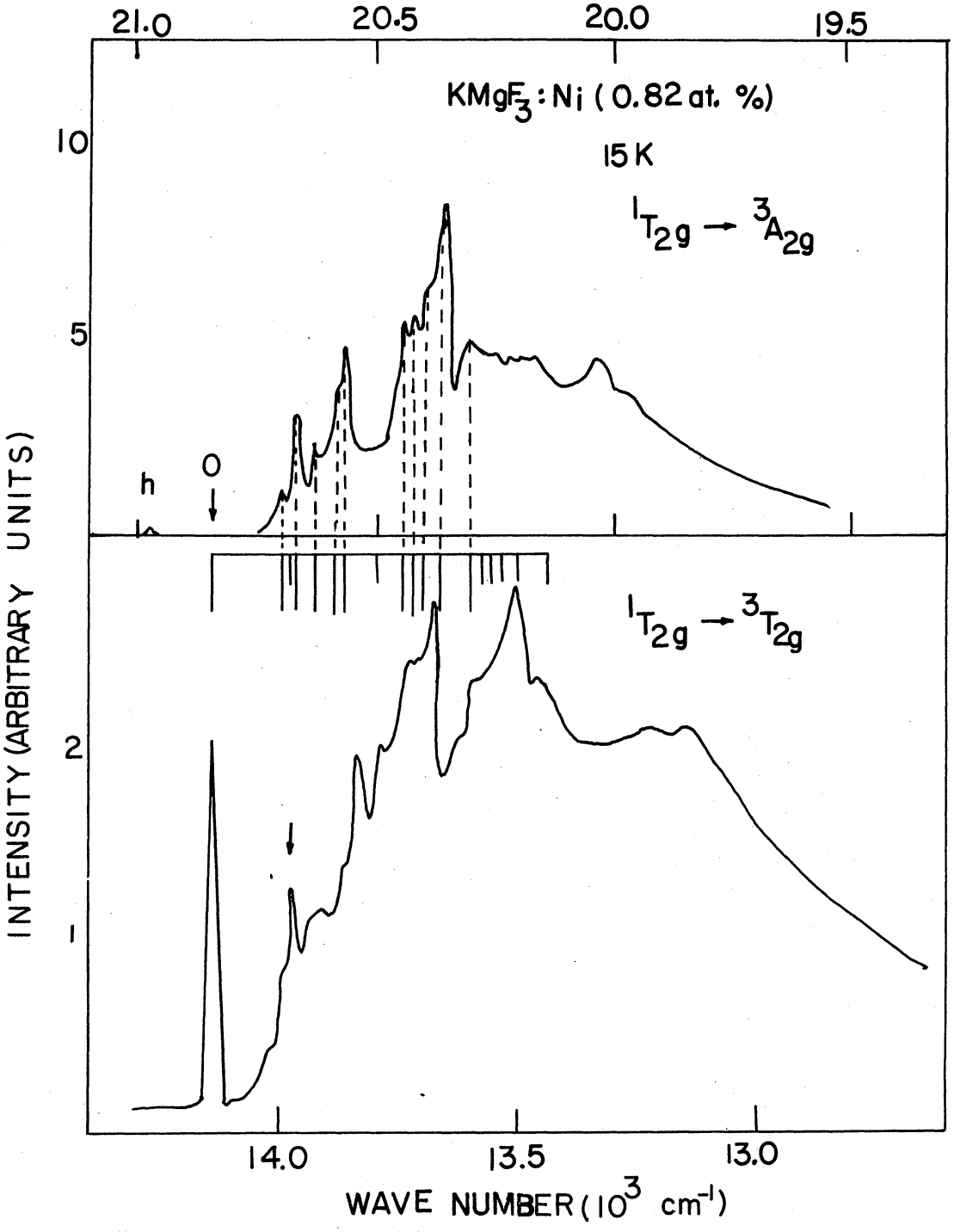

Figure 10. Emission Bands for $KMgF_3$:Ni at 15 K

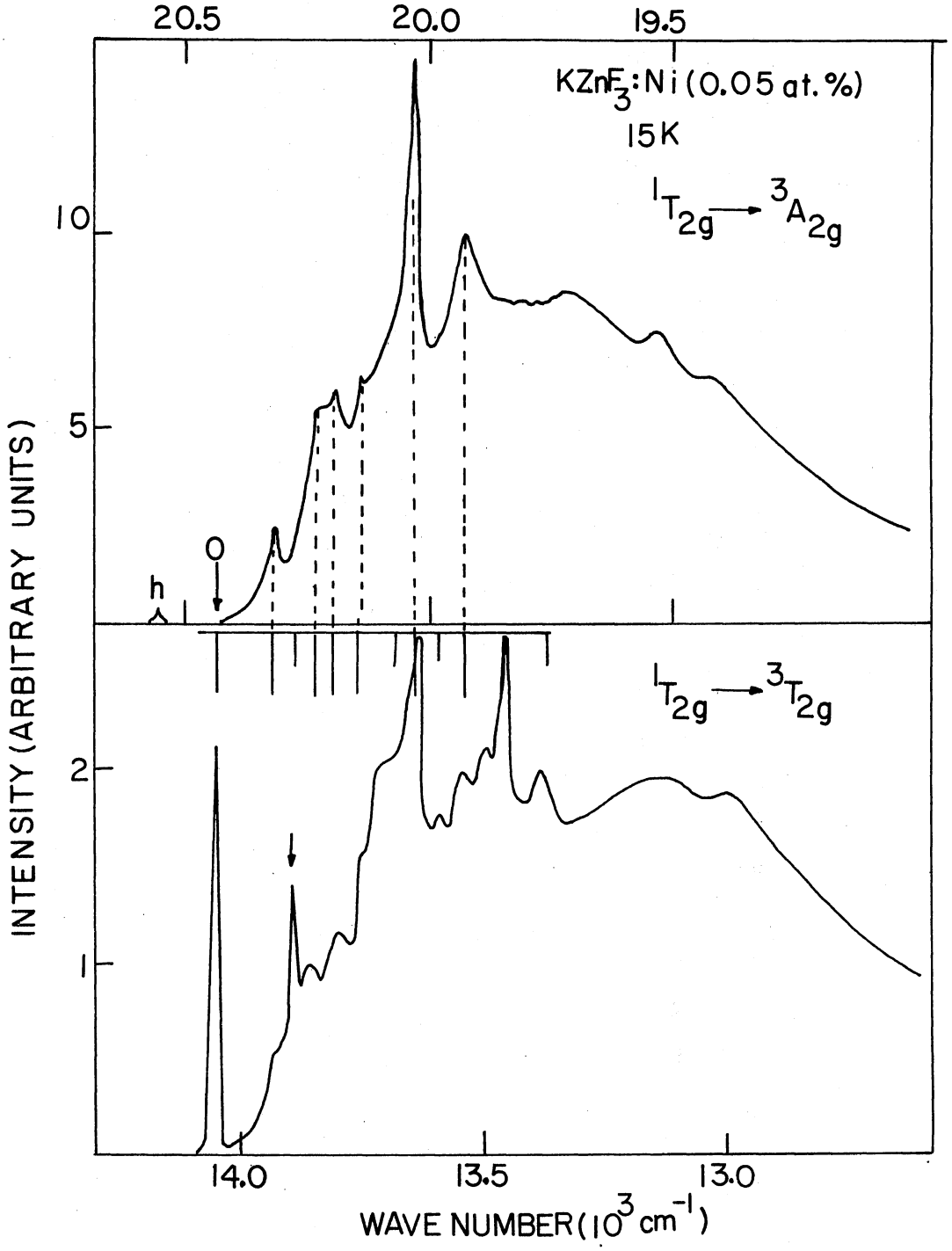

Figure 11. Emission Bands for $KZnF_3$:Ni at 15 K

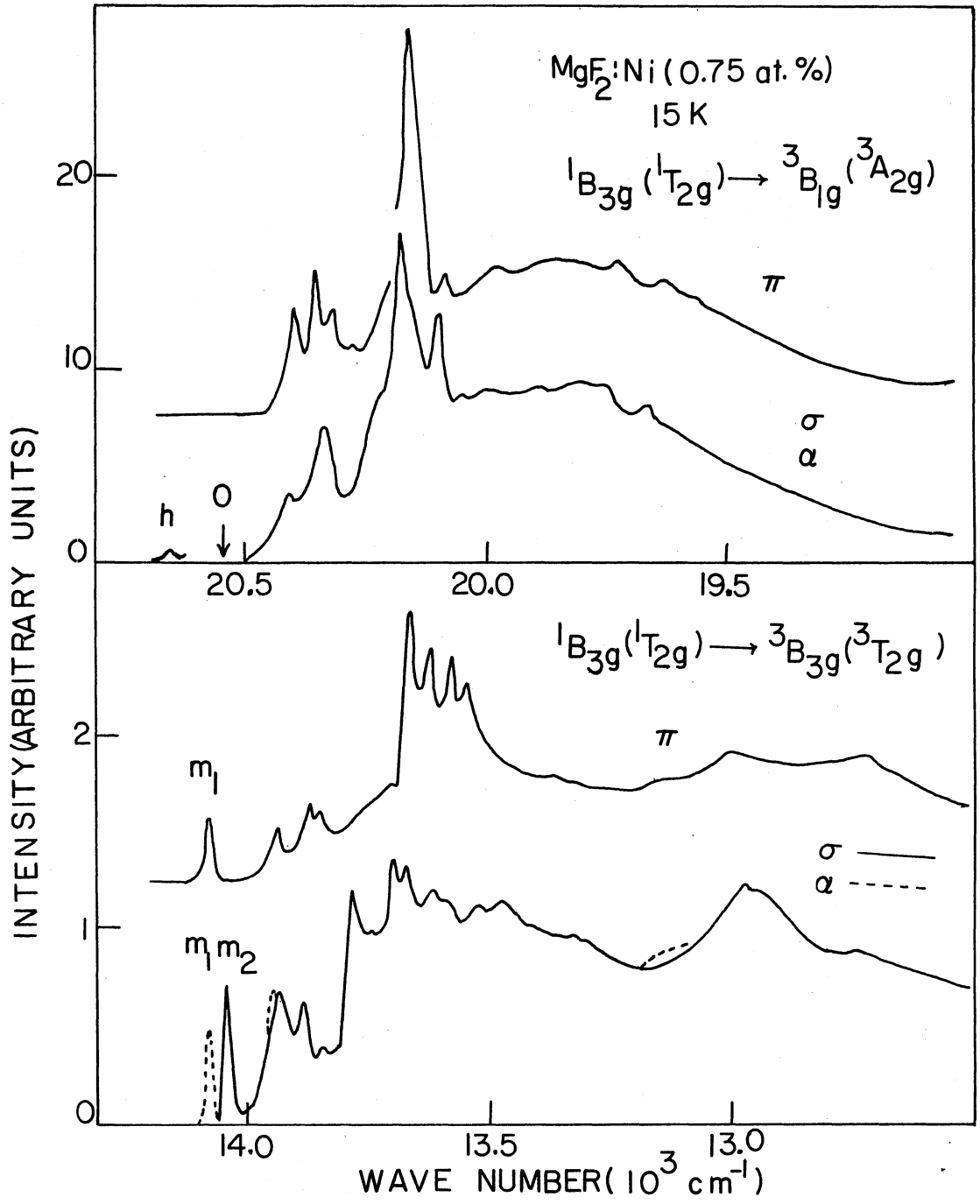

Figure 12. Polarized Emission Bands for MgF_2:Ni at 15 K

axis and the electric vector perpendicular to and parallel to the optic axis respectively. The α spectrum is for unpolarized light propagating along the optic axis. With the exception of the two sharp lines, m_1 and m_2, the σ and α spectra are identical for both bands. This indicates that the broad bands are primarily due to electric-dipole transitions and from symmetry arguments the bands must therefore be phonon assisted. The two lines m_1 and m_2 presumably are split due to the defect symmetry D_{2h} in MgF_2 and merge into one sharp line for a site of O_h symmetry in cubic crystals. The fact that the π and α spectra are identical for these lines indicates that they are magnetic-dipole transitions. Although a corresponding sharp line is not observed in any of the higher energy 20,000 - 21,000 cm^{-1} emission bands, the position of such a pure magnetic-dipole transition for these bands can be inferred as follows: As the sample temperature is increased from 12 K to 100 K, a small band (labeled h in the figures) appears in the spectra. Assuming that this "hot" band is due to an electronic transition assisted by the annihilation of a phonon in the lowest possible mode, the missing zero-phonon line should lie halfway between "h" and the first peak in the low temperature emission spectrum. This position is indicated by the arrow, o, in the figures and is the assumed origin for these bands.

For the higher energy transition in $MgF_2:Ni^{2+}$, a hot band was observed in the σ and α spectra which indicated that the band was due to phonon assisted electronic transition. The pure electronic magnetic-dipole transitions are assumed to be at o as before.

Peak positions and the separations from the band origins are presented in Tables II - V. The observed peak separations are in the range of appropriate lattice vibrations and show good agreement in the cases

TABLE II

SPACING OF EMISSION LINES IN $MgO:Ni^{2+}$

$^1T_{2g} \rightarrow {}^3A_{2g}$		$^1T_{2g} \rightarrow {}^3T_{2g}$			
Peak Position (cm^{-1})	Separation From Band Origin (cm^{-1})	Peak Position (cm^{-1})	Separation From Band Origin (cm^{-1})	Series	Separation From Series Origin (cm^{-1})
21,240 (h)	-189	13,120	Origin	A	0
(21,051)	Origin	12,938	182	B	0
20,872	189	12,925	195	A	195
20,673	388	12,824	296	C	0
20,479	582	12,760	360	B	178
20,288	773	12,710	410	A	410
20,092	969	12,682	438	D	0
19,881	1180	12,637	483	C	187
19,689	1372	12,578	542	B	360
		12,525	595	A	595
		12,506	614	D	176
		12,469	651	C	355
		12,399	721	B	539
		12,247	873	E	0

TABLE III

SPACING OF EMISSION LINES IN $KMgF_3:Ni^{2+}$

$^1T_{2g} \rightarrow {}^3A_{2g}$		$^1T_{2g} \rightarrow {}^3T_{2g}$			
Peak Position (cm^{-1})	Separation From Band Origin (cm^{-1})	Peak Position (cm^{-1})	Separation From Band Origin (cm^{-1})	Series	Separation From Series Origin (cm^{-1})
20,973 (h)	-139	14,138	Origin	A	0
(20,834)	Origin	14,013	125	A	125
20,695	139	13,976	162	A	162
20,670	164	13,972	166	B	0
20,627	207	13,931	207	A	207
20,582	252	13,904	234	A	234
20,563	271	13,829	309	B	143
20,437	397	13,780	358	B	192
20,408	426	13,732	406	A	406
20,379	455			B	240
20,358	476	13,676	462	A	462
20,300	534	13,646	492	A	492
		13,594	544	A	544
				B	378
				C	0
		13,506	632	B	466
		13,457	681	C	137

TABLE IV

SPACING OF EMISSION LINES IN $MgF_2:Ni^{2+}$

$^1T_{2g} \rightarrow {}^3A_{2g}$			$^1T_{2g} \rightarrow {}^3T_{2g}$	
Peak Position (cm^{-1})		Separation From Band Origin (cm^{-1})	Peak Position (cm^{-1})	Separation From Band Origin
20,653 (h)	σ	-120	14,073 π	Origin
(20,533)	σ	Origin	14,027 σ	36
20,412	σ	121	13,954 π	119
20,392	π	141	13,928 σ	145
20,346	π	187	13,870 σ	203
20,329	σ	204	13,863 π	210
20,305	π	228	13,847 π	226
20,284	π	249	13,827 σ	246
20,190	σ	343	13,774 σ	299
20,182	σ	351	13,710 σ	363
20,161	π	372	13,693 σ	380
20,141	σ	392	13,656 π	417
20,100	σ	433	13,618 π,σ	455
20,092	π	441	13,572 π	501
20,045	σ	488	13,539 π	534
19,960	π	573	13,514 σ	559
19,896	σ	637	13,459 σ	614
19,806	σ	727	13,405 π	668
19,755	π	778	13,320 π,σ	753
19,743	σ	790	13,290 σ	783
19,666	π	867	13,000 π	1,073
19,639	σ	894	12,977 σ	1,096
			12,940 σ	1,133
			12,736 σ	1,337

TABLE V

SPACING OF EMISSION LINES IN $KZnF_3:Ni^{2+}$

$^1T_{2g} \rightarrow {}^3A_{2g}$		$^1T_{2g} \rightarrow {}^3T_{2g}$			
Peak Position (cm^{-1})	Separation From Band Origin (cm^{-1})	Peak Position (cm^{-1})	Separation From Band Origin (cm^{-1})	Series	Separation From Series Origin (cm^{-1})
20,555 (h)	-119	14,049	0	A	0
(20,436)	Origin	13,928	121	A	121
20,317	119	13,889	160	B	0
20,218	218	13,850	199	A	199
20,190	246	13,793	256	A	256
20,145	291	13,746	303	A	303
20,032	404			B	143
20,932	504	13,699	356	B	190
		13,628	421	A	421
				B	261
		13,583	466	B	306
		13,535	514	A	514
		13,481	568	C	0
		13,456	593	B	433
		13,378	671	B	511

where information on Ni^{2+} substituted lattices is available (79-84).

The temperature dependence of the peak positions, line widths, and relative intensities of the lines m_1 and m_2 are shown in Figure 13. It is noted that within experimental error the temperature dependence of the half-width is the same for both lines and that the ratio of the intensities is constant over the temperature range from 15 K to 80 K.

The effect of a <100> stress on the narrow line of the 13,000 cm^{-1} band in MgO was also examined. A slight shift of the peak to lower energy with increasing stress was observed. Polarization properties were also examined. Both the σ and π components show approximately the same energy shift of 5 cm^{-1} at a pressure of 1.94×10^8 dynes/cm^2. At this pressure, the σ component has approximately the same halfwidth as the unstressed line while the π component is about 25% narrower. The peak height of the σ line is enhanced with respect to that of the π component with increasing pressure.

Discussion

The energy level schemes shown in Figure 14 (20,21,85-87) have been compiled mainly from published optical absorption data (32,69,88,89). The group representations of the levels in the absence of spin-orbit coupling are listed on the left of each column. It is for convenience that these designations are used in describing transitions from one group of levels to another even in the case of $MgF_2:Ni^{2+}$ where the crystal field is of lower symmetry. The spin-orbit splittings as measured from the bottom level of a set are shown on the right side of each column together with the appropriate group representations. However, the subscript g common to all levels in the designation of the group

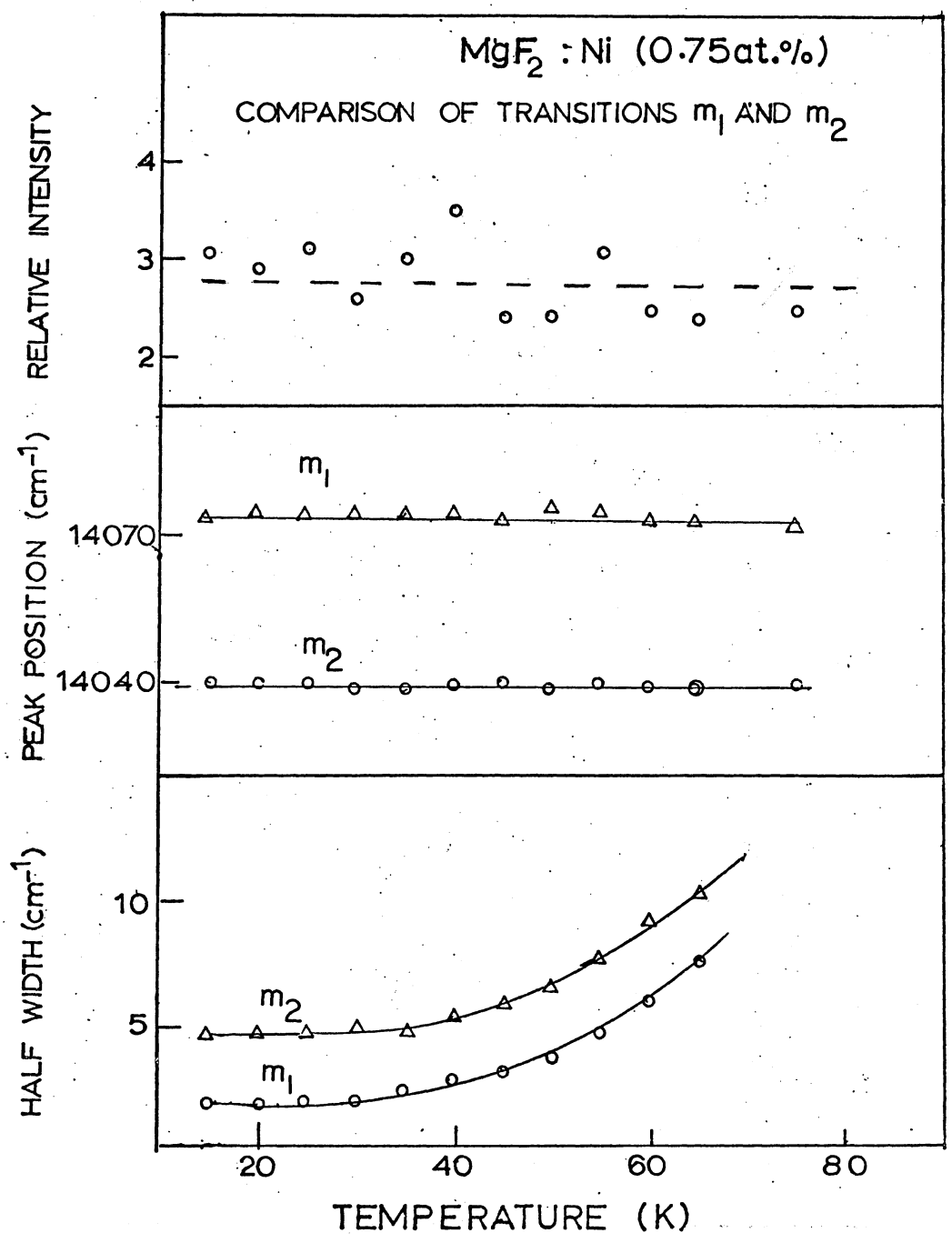

Figure 13. Observed Temperature Dependence of the Narrow Lines, m_1 and m_2 in the Emission Band of $MgF_2:Ni^{2+}$ Showing Relative Intensity, Peak Position, and Full Width at Half Maximum

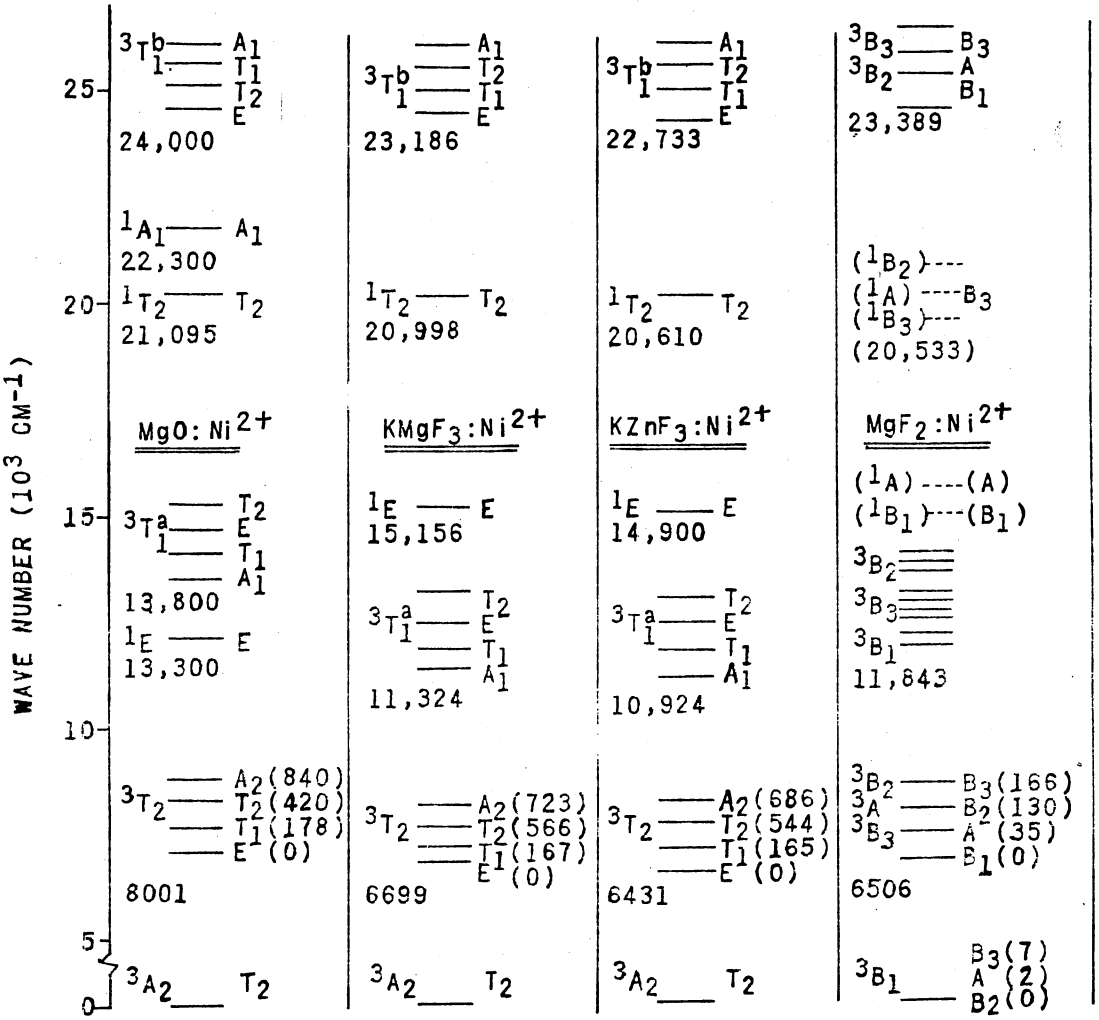

Figure 14. Energy Level Schemes for Ni^{2+} Ion in Four Host Crystals

representations has been omitted.

The results suggest that the exciting light causes a transition from the ground state ($^3A_2$) to the $^3T_1{}^b$ set of states at 25,000 cm^{-1}. Radiationless transitions occur to the $^1T_2$ states from which both emission bands under discussion originate. The more energetic band results from a transition which terminates on the ground state, while the lower energy transitions terminate on the first excited set of levels ($^3T_2$). Support for this interpretation, as presented below, is based on observed band energies and spin-orbit splittings, polarization data, excitation data, and to a limited extent on the consistency of the result of uniaxial stress measurements.

Energy Assignments

Energies for transitions from the lowest of the $^1T_2$ set of levels to the $^3A_2$ and $^3T_2$ states are summarized in Table VI. It is noted that there is good agreement between the results (the underlined numbers) and existing data for the $^1T_2 \rightarrow {}^3A_2$ transition. There is also agreement in the assignment of the lower energy band to the $^1T_2 \rightarrow {}^3T_2$ transition. The assignment of the lower energy band to the $^1E \rightarrow {}^3A_2$ transition leads to discrepancies significantly outside of the limits which could be attributed to experimental error in the case of the $KMgF_3$ and $KZnF_3$ hosts. No experimental data are available for the $^1T_2 \rightarrow {}^1E$ levels in $MgF_2:Ni^{2+}$. However, if the results from the $^1T_2 \rightarrow {}^3A_2$ emission are employed to determine the energy of the lowest $^1T_2$ level as 20,533 cm^{-1}, the $^1T_2 \rightarrow {}^3T_2$ assignment is consistent with existing data on the $^3T_2$ energy level. For $MgO:Ni^{2+}$, the energies are such that the 13,000 cm^{-1} band could be assigned to either the $^1T_2 \rightarrow {}^3T_2$ or the $^1E, {}^3T_1{}^a \rightarrow {}^3A_2$

TABLE VI

OBSERVED ENERGIES OF Ni^{2+} TRANSITIONS

Transition	Host			
	MgO	$KMgF_3$	$KZnF_3$	MgF_2
	(cm^{-1})			
$^1T_{2g} \rightarrow {}^3A_{2g}$	21095	20998	20610	-
	21056	20834	20436	20533
$^1T_{2g} \rightarrow {}^3T_{2g}$	13094	14229	14179	14027
	13120	14138	14049	14073
$^1E_g \rightarrow {}^3A_{2g}$	13300	15156	14900	-

transitions, but the excitation spectrum does not support the ^1E, $^3T_1{}^a \rightarrow {}^3A_2$ possibility.

Spin-Orbit Splittings

The position of some of the spin-orbit components of the $^3T_2$ set of levels can be inferred from a comparison of the two spectra for each of the three cubic host crystals. However, some of the spin-orbit splittings in $MgF_2:Ni^{2+}$ can be observed directly by examination of the 13,000 cm^{-1} band. In the latter case, the two lines, m_1 and m_2, as indicated previously are probably pure electronic transitions. If the reasonable assumption is made that the observed 36 cm^{-1} splitting of these lines is due to a splitting of the terminal state of the transition it is clear, from an examination of Figure 14, that the transition can only end on the $^3T_2$ levels. Seeing the presence of higher spin-orbit levels can also be expected, but transitions ending on these levels are obscured by the presence of phonon assisted peaks in the spectrum.

If the 13,000 cm^{-1} band in $MgF_2:Ni^{2+}$ were due to a $^1E \rightarrow {}^3A_2$ transition, the 36 cm^{-1} splitting would have to be due to crystal field splitting of the ^1E level since the spin-orbit splittings of the ground state are only 2 cm^{-1} and 7 cm^{-1} (87). The relative properties, strengths and positions of lines m_1 and m_2 for a thermalized system might be expected to vary over the temperature range 15K to 80K if the splitting were in the initial state. It can be seen from Figure 13 that the intensity ratio is constant within experimental error. However, the primary evidence that the 36 cm^{-1} splitting cannot be due to the splitting of the ^1E levels is presented below in the section on polarization.

For the cubic host crystals, the spin-orbit splitting can be ob-

served as follows. If the assumption is made that the peaks in the $^1T_2 \rightarrow {}^3A_2$ bands are due to phonon assisted transitions, then one should expect to see peaks with about the same energy spacing in the $^1T_2 \rightarrow {}^3T_2$ band. To make it clear, in Figures 9-11, the peak positions of the phonon assisted transitions of the 21,000 cm^{-1} bands are marked by the long lines shown above the 13,000 cm^{-1} bands. The series of phonon assisted peaks are labeled A in Tables II-IV. From Figure 9, for the case of MgO:Ni, it is observable that the phonon assisted peaks of the 21,000 cm^{-1} band are mirrored by the 13,000 cm^{-1} band. However, it is evident that "extra" peaks occur in this latter band. The first "extra" peak indicated by an arrow in the figure is a relatively sharp line 182 cm^{-1} to the low energy side of the first peak (band origin). The model suggests that the first peak is a pure electronic transition to the E component of the $^3T_2$ (E) set of levels and that the "extra" peak is a transition ending on the T_1 component, $^3T_2(T_1)$. The splitting of 182 cm^{-1} is in good agreement with the previously measured splitting of 178 cm^{-1} for these two states. A second series of phonon assisted peaks, labeled series B in Table II, with the same energy separations as in the higher energy band should be observed to originate on the $^1T_2 \rightarrow {}^3T_2$ (T_1) line. The shorter lines shown above the 13,000 cm^{-1} band in Figure 9 illustrate where these peaks should appear. It is possible that another "extra" peak at 438 cm^{-1} from the $^1T_2 \rightarrow {}^3T_2$ (E) line is due to the $^1T_2 \rightarrow {}^3T_2$ (T_2) transition since the observed splitting of the $^3T_2$ (T_2) level is 429 cm^{-1}. It should be pointed out that Moreau et. al. (90) have associated the emission peaks at 20,940 and 20,745 cm^{-1} with a Jahn-Teller effect. A detailed analysis of collected data in terms of a Jahn-Teller would be complicated. A better understanding of the sit-

uation will be obtained once more data become available, like that presented by Moreau et. al.

In $KZnF_3$ the situation is similar. Several peaks in the $^1T_2 \rightarrow {}^3T_2$ band can be associated with phonon assisted peaks (as observed in the $^1T_2 \rightarrow {}^3A_2$ band). Again there is a sharp "extra" peak split from the first electronic transition by 160 cm^{-1}. This is in a good agreement with the spin-orbit splitting of the $^3T_2$ (E) and $^3T_2$ (T_1) levels observed by Ferguson et. al. (21). While the phonon spectrum of $KZnF_3:Ni^{2+}$ is so complicated that it makes it difficult to identify a second series of peaks based on the $^1T_2 \rightarrow {}^3T_2$ (T_1) transition, the significance lies in the evidence that the two prominent peaks near the center of the $^1T_2 \rightarrow {}^3T_2$ band are split by 172 cm^{-1}, suggesting that the lower energy peak may be associated with the $^1T_2 \rightarrow {}^3T_2$ (T_1) transitions involving an interaction with the same phonon mode.

In $KMgF_3:Ni^{2+}$, the $^3T_2$ (T_1) level is 167 cm^{-1} above $^3T_2$ (E). Examination of the $^1T_2 \rightarrow {}^3A_2$ band shows that there is a phonon mode at approximately this same energy so that the $^1T_2 \rightarrow {}^3T_2$ (T_1) transition is obscured. It is worthwhile to note, however, that while there is one prominent peak near the center of the $^1T_2 \rightarrow {}^3A_2$ band, there are two similar peaks in the $^1T_2 \rightarrow {}^3T_2$ band separated by 170 cm^{-1}. This implies that the splitting of these peaks reflects the spin-orbit splitting of the $^3T_2$ (E) and $^3T_2$ (T_1) levels, as is the case for $KZnF_3:Ni^{2+}$.

Polarized Emission

Polarized emission spectra of $MgF_2:Ni^{2+}$ support the assignment of the 13,000 cm^{-1} band to the transition $^1T_2 \rightarrow {}^3T_2$. As indicated previously, a comparison of the σ,π and α spectra indicates that the lines m_1

and m_2 are polarized, magnetic-dipole transitions in D_{2h} symmetry. A study of the energy level diagram in Figure 14 shows that the only scheme which fits the data, i.e., a pure π transition 35 cm^{-1} higher in energy than a pure σ transition, is that illustrated in Figure 15a. This then establishes the transition giving rise to lines m_1 and m_2 as $^1T_2\ (B_3) \rightarrow {}^3T_2\ (B_1)$ and $^1T_2\ (B_3) \rightarrow {}^3T_2\ (A)$, respectively. The $^1T_2\ (B_3)$ level is presumably the lowest of three $^1T_2$ components, $^1T_2(A)$, $^1T_2(B_2)$ and $^1T_2(B_3)$.

The other energetically possible assignment for the 13,000 cm^{-1} band is $^1E \rightarrow {}^3A_2$. In this case lines m_1 and m_2 would have to originate on the $^1E\ (A)$ and $^1E\ (B_1)$ levels with these levels split by 35 cm^{-1}. Combining this with the known assignments of the ground state levels, (21) one obtains the schemes shown in Figures 15b and 15c. It is clear that neither of these can explain the observed spectra.

Uniaxial Stress Measurements

The results of the uniaxial stress measurements on the 13,000 cm^{-1} band in $MgO:Ni^{2+}$ are consistent with both $^1T_2 \rightarrow {}^3T_2$ and $^3T_2{}^a$, $^1E \rightarrow {}^3A_2$ transitions, and hence are inconclusive in distinguishing between the two possibilities. The transition $^1T_2 \rightarrow {}^3T_2$ has been proposed in the previous section. The interpretation of the stress responsible for this transition is as follows. With a stress along the z-axis, [001], the symmetry of the Ni^{2+} site is lowered from O_h to D_{4h}. This splits the $^1T_2$ level into $^1T_2\ (E)$ and $^1T_2\ (B_2)$ components. Since the B_2 states have lobes in the plane perpendicular to the stress direction ($\theta_{B_2} \sim xy$); it is expected that the energy of the level will be only slightly affected by the stress. The E states have lobes at 45^o to the stress axis

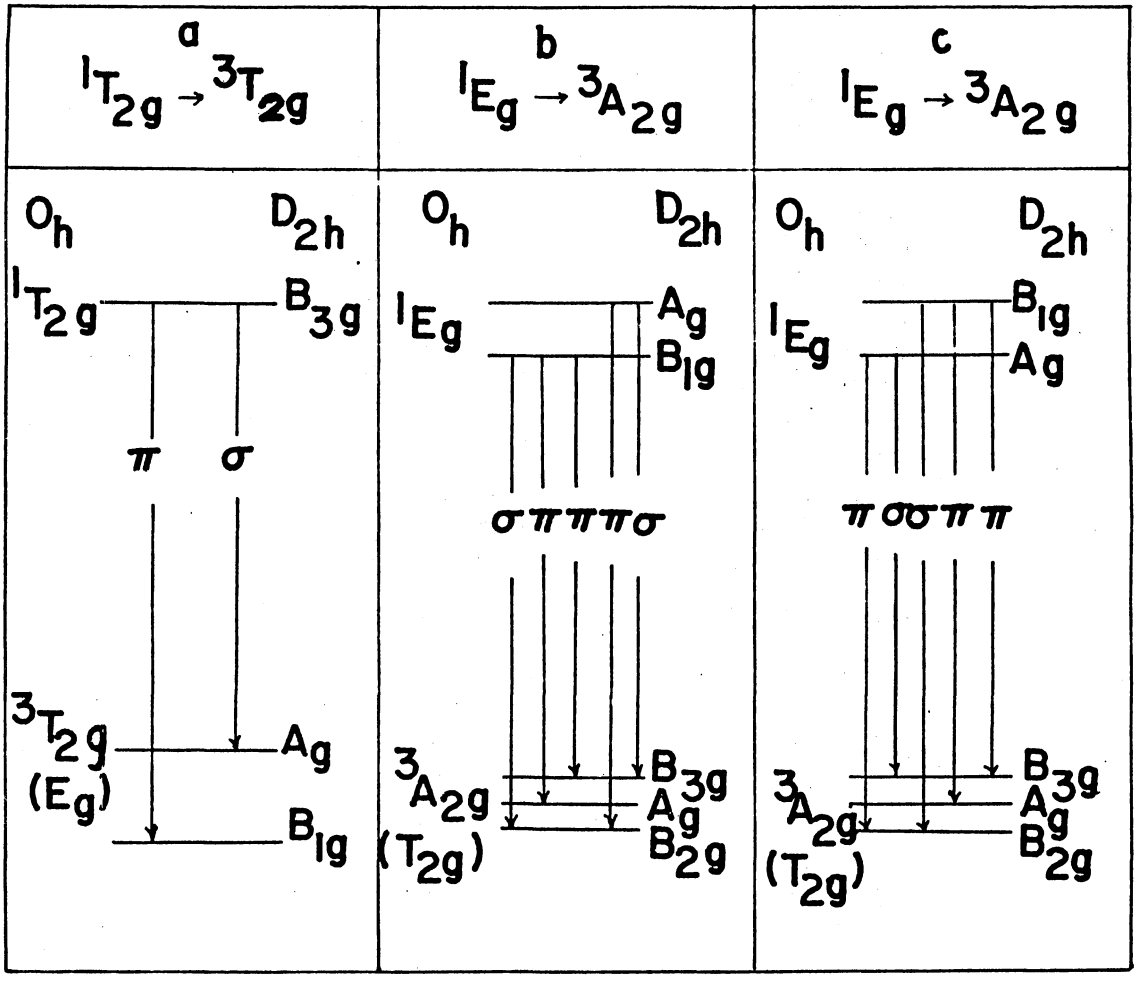

Figure 15. Magnetic-Dipole Allowed Transitions, (a) $^1T_{2g} \rightarrow {}^3T_{2g}$, (b) and (c) $^1E_g \rightarrow {}^3A_{2g}$

(θ_E ~ xz, yz), and from elementary considerations it is expected that their energy to be increased as the stress is applied. The terminal level of this transition, $^3T_2$ (E), would be split into $^3T_2$ (A_1) and $^3T_2$ (B_1) components. Furthermore, the B_1 states, having lobes perpendicular to [001] (θ ~ (x^2-y^2)) will be shifted only slightly, while the A_1 state with lobes along the stress axis (θ ~ Z^2) should have its energy increased.

The two observed effects, the shift of the band to slightly lower energy and the apparent enhancement of the σ polarization with respect to the π polarization, might then be explained as follows: The shift of the σ component to lower energy is due to a slightly larger downward shift of the $^3T_2$ (B_1) level than that of the $^1T_2$ (B_2) level [or a larger downward shift of the $^1T_2$ (B_2) level]. The π component consists of a pair of lines, one member shifted downward $^1T_2$ (E) $\rightarrow$ $^3T_2$ (A_1) and the other upward $^1T_2$ (E) $\rightarrow$ $^3T_2$ (B_1) such that the center of the pair is shifted to lower energies. Two effects tend to enhance the peak height of the σ transition: (1) the π transitions, being an unresolved doublet tend to appear as a broader line than the singlet transition, and (2) the π intensities are decreased by a reduced population in the $^1T_2$ (E) level (at 4^oK, $kT \simeq 2.8\ cm^{-1}$ which is comparable with the observed energy shifts).

Mn^{2+}: Emission Bands in $KMgF_3$ and MgF_2

Results

Afterglow Emission. When $KMgF_3$:Mn is irradiated at any temperature between 15 and 300K, with even a low dose of high energy electrons, an emission band with peak at about 610 nm is evident as an afterglow. The

same emission band is observed if an unirradiated sample is excited with x-rays or optically stimulated with 365 nm or 450 nm light after the irradiation. This band is illustrated in Figure 16. Excitation of unirradiated $KMnF_3$ at 15K by x-rays or optical excitation results in similar emission with slight changes in the sharp line structure. This emission is attributed to Mn^{2+}.

As shown in Figure 17, MgF_2:Mn and Mn yields a similar emission band at 590 nm under the same treatments described above. In the same figure, the σ, π, and α emission is portrayed.

Immediately after irradiation at temperatures below 80K a complicated absorption occurs for $KMgF_3$:Mn and MgF_2:Mn which decays with time and/or optical bleaching. An optical bleach with 450 nm light decreases rapidly the absorption in certain regions. In Figure 18, the spectra, which are shown as the solid lines, for absorption before and after a 450 nm bleach are depicted. The dashed lines in the figure represent the excitation spectra for the 590 nm and 610 nm luminescence bands. When optical bleaching is effective and a crystal with cubic structure such as $KMgF_3$ is being used, it is possible to use polarized light to determine the orientation of the defects responsible for the emission and absorption. Illustration of the data for such a polarized bleach is presented in Figure 19.

680 nm Emission. After some 20 minutes in the dark or 1 minute under white light illumination with the sample at 15K, the emission bands at 610 nm for $KMgF_3$:Mn and 590 nm for MgF_2:Mn almost disappear. In the case of $KMgF_3$:Mn, when this band has decreased, it is possible to detect emission around 680 nm when measurement is made below 180 K, and at 630 nm when the sample is above 180K. The lifetimes of these

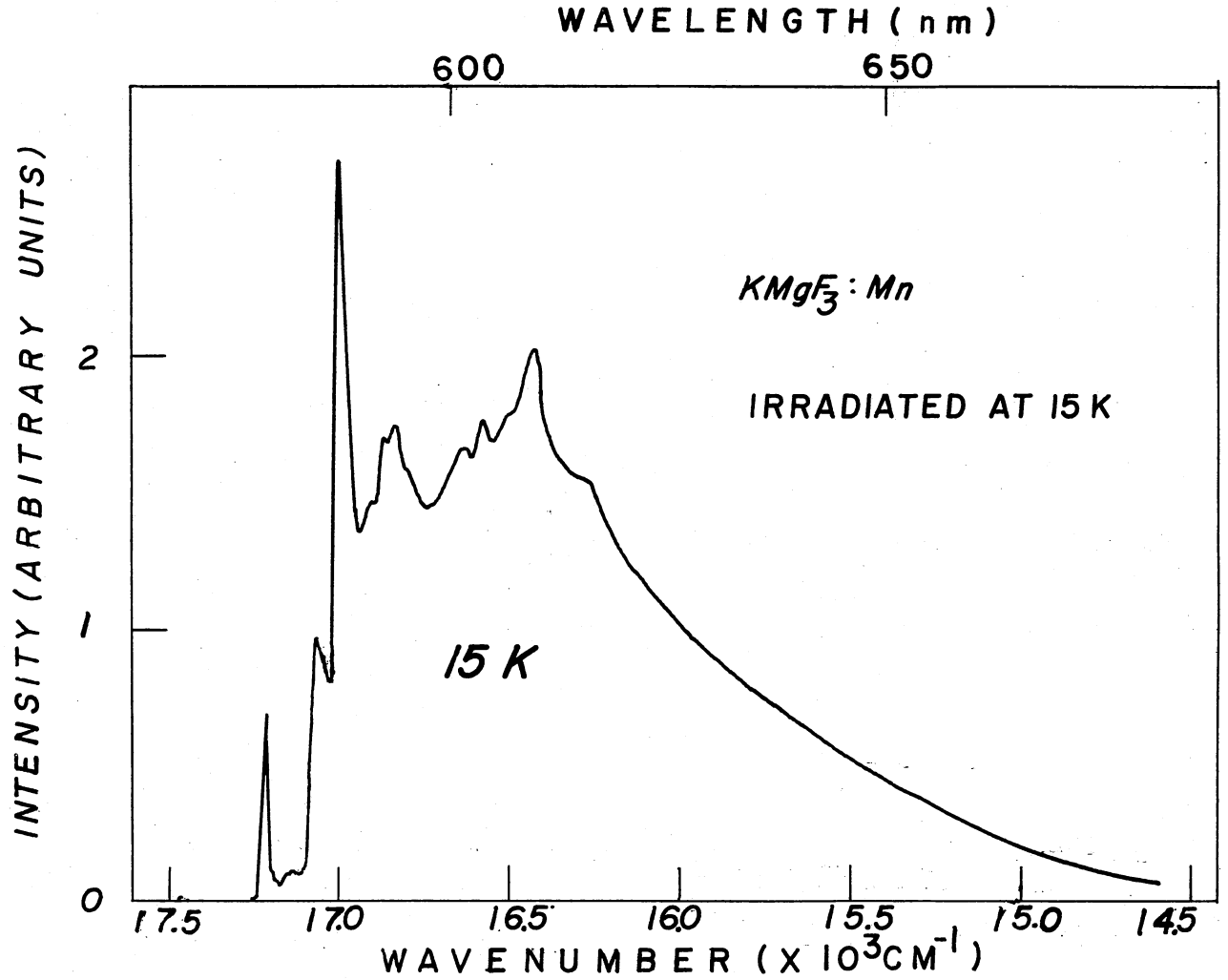

Figure 16. The 610 nm Emission Band Present in Low Temperature Irradiated $KMgF_3$:Mn

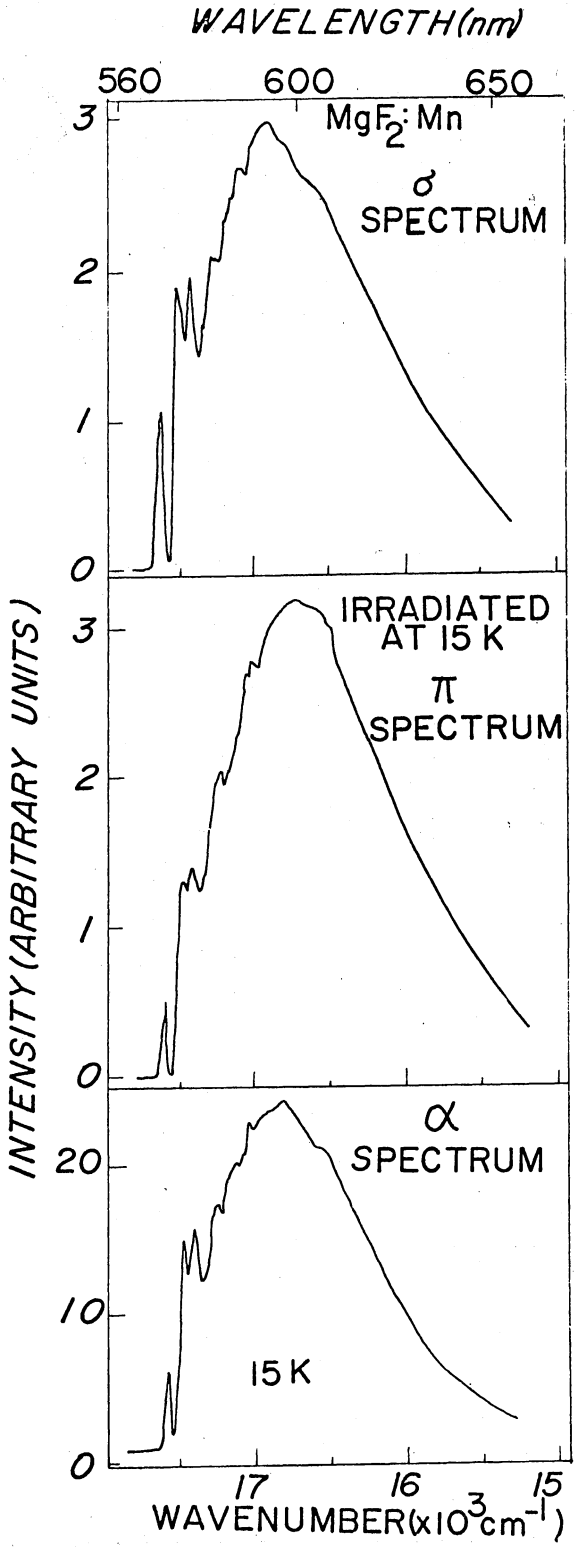

Figure 17. Polarized 590 nm Emission Band Observed in Low Temperature Irradiated MgF_2:Mn

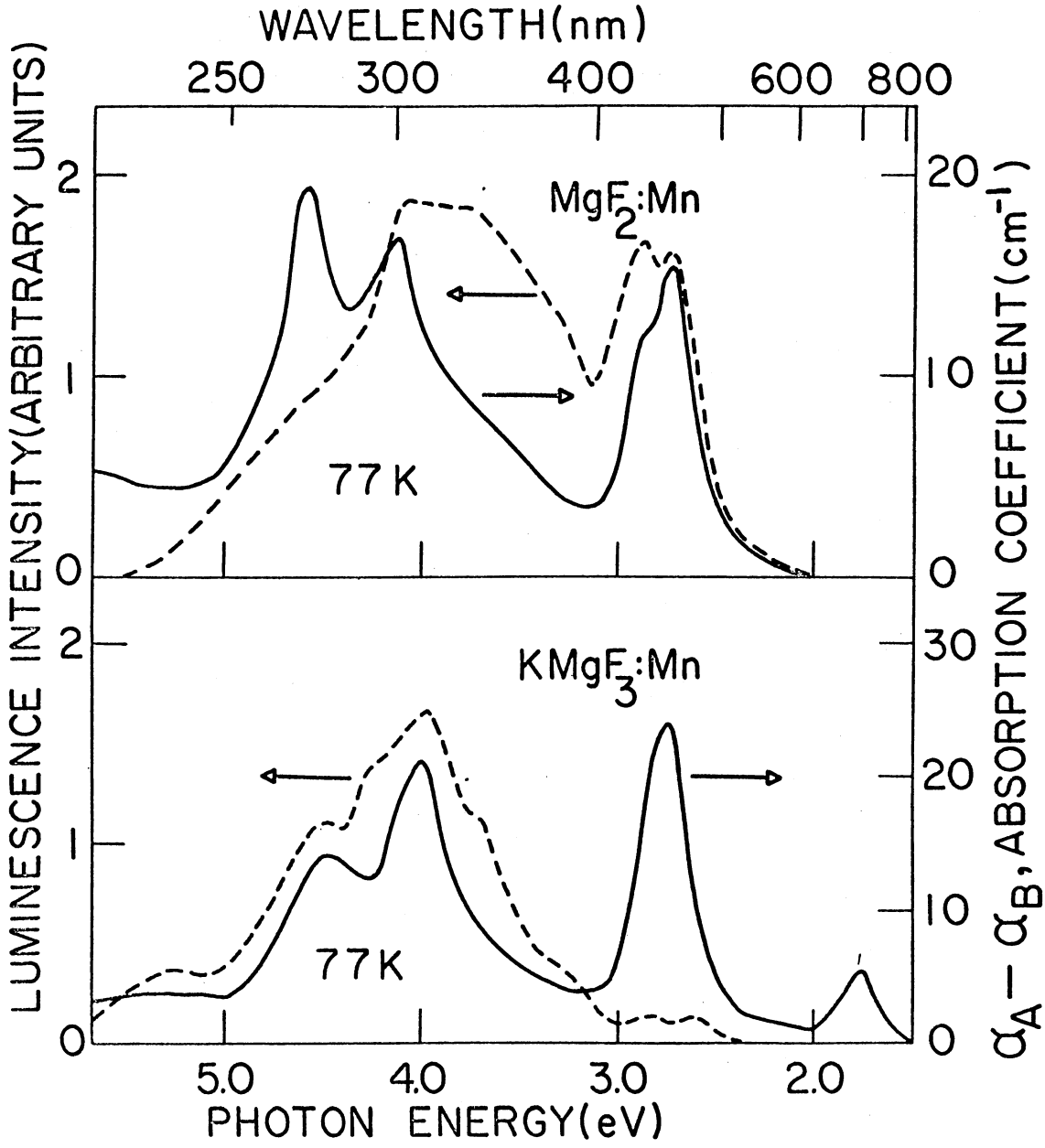

Figure 18. The Dashed Lines Represent Excitation Data Taken Using the 590 nm Emission Band of MgF_2:Mn and the 610 nm $KMgF_3$:Mn Emission. The solid lines are absorption data

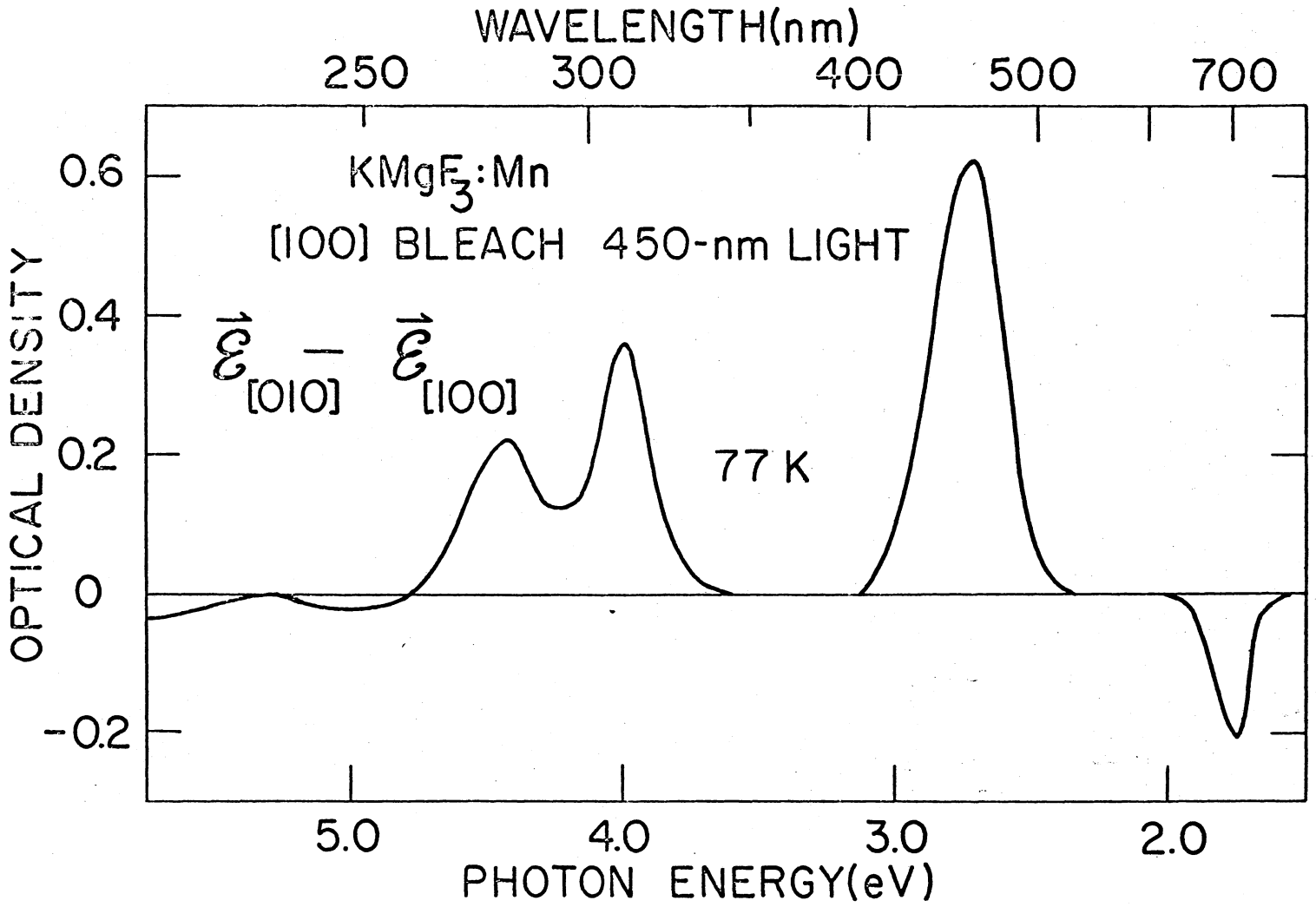

Figure 19. The Difference Curve for Irradiated $KMgF_3$:Mn Bleached With [100] Polarized Light

bands differ appreciably as has been noted previously by Sibley, Yun, and Vehse (66). The low temperature spectrum of this band is shown in Figure 20, and the excitation spectrum for a sample irradiated and held at 15K is portrayed in Figure 21.

720 nm Emission. When $KMgF_3$:Mn crystals which have been irradiated at 15K and then warmed to room temperature are measured at 15K, the 680 nm band has decreased, but an emission band at 720 nm has increased. At 15K irradiation, the 680 nm band is more intense and the 720 nm band is extremely weak. On the other hand, 300K irradiated specimens measured at low temperature show a dominant 720 nm band. The luminescence band at 720 nm and the excitation spectrum for this band taken with the sample at 15K are shown in Figure 22 and Figure 23, respectively.

For a sample irradiated at 300K, the intensity differences between these two emission bands are displayed in Figure 24. The 720 nm emission is more intense, but both emissions have similar growth characteristic. When the sample is thermally annealed above room temperature, the emission from the two bands has similar decay characteristic, as shown in Figure 24. The absorption spectrum after being irradiated at 300K, is shown in Figure 25.

670 nm Emission. The σ, π, and α emission spectra for MgF_2:Mn specimens irradiated at 15K are illustrated in Figure 26. It should be noted that there is some difference in the intensity of the fine structure between the various spectra. The excitation spectrum for this 670 nm band is presented in Figure 27. The inset of the figure provides an expanded picture of the $^4T_{1g}$ band at about 570 nm and shows the polarization of the band for the polarizer oriented along the c axis of the

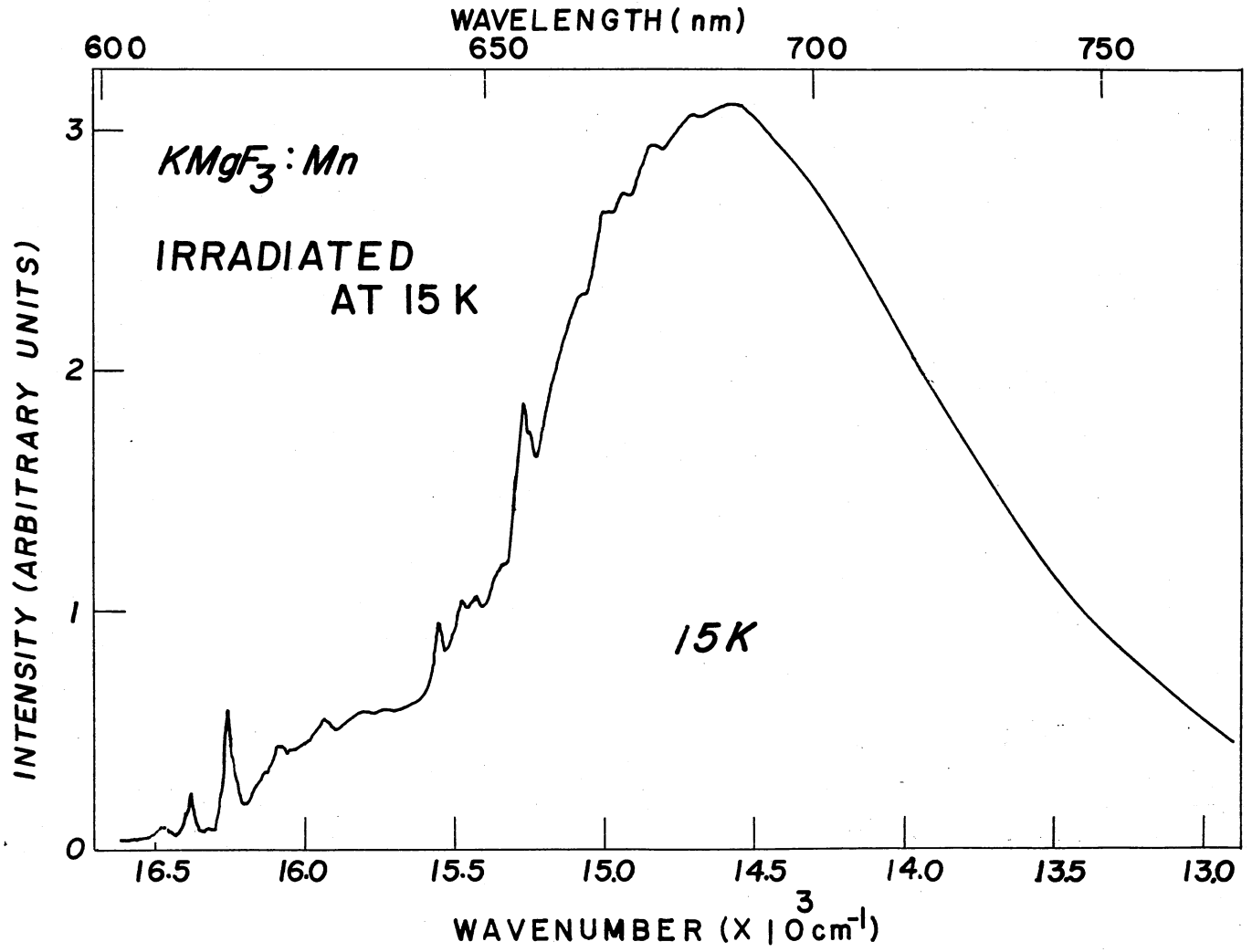

Figure 20. The 680 nm Emission Band From 15 K Electron-Irradiated $KMgF_2$:Mn at 15 K

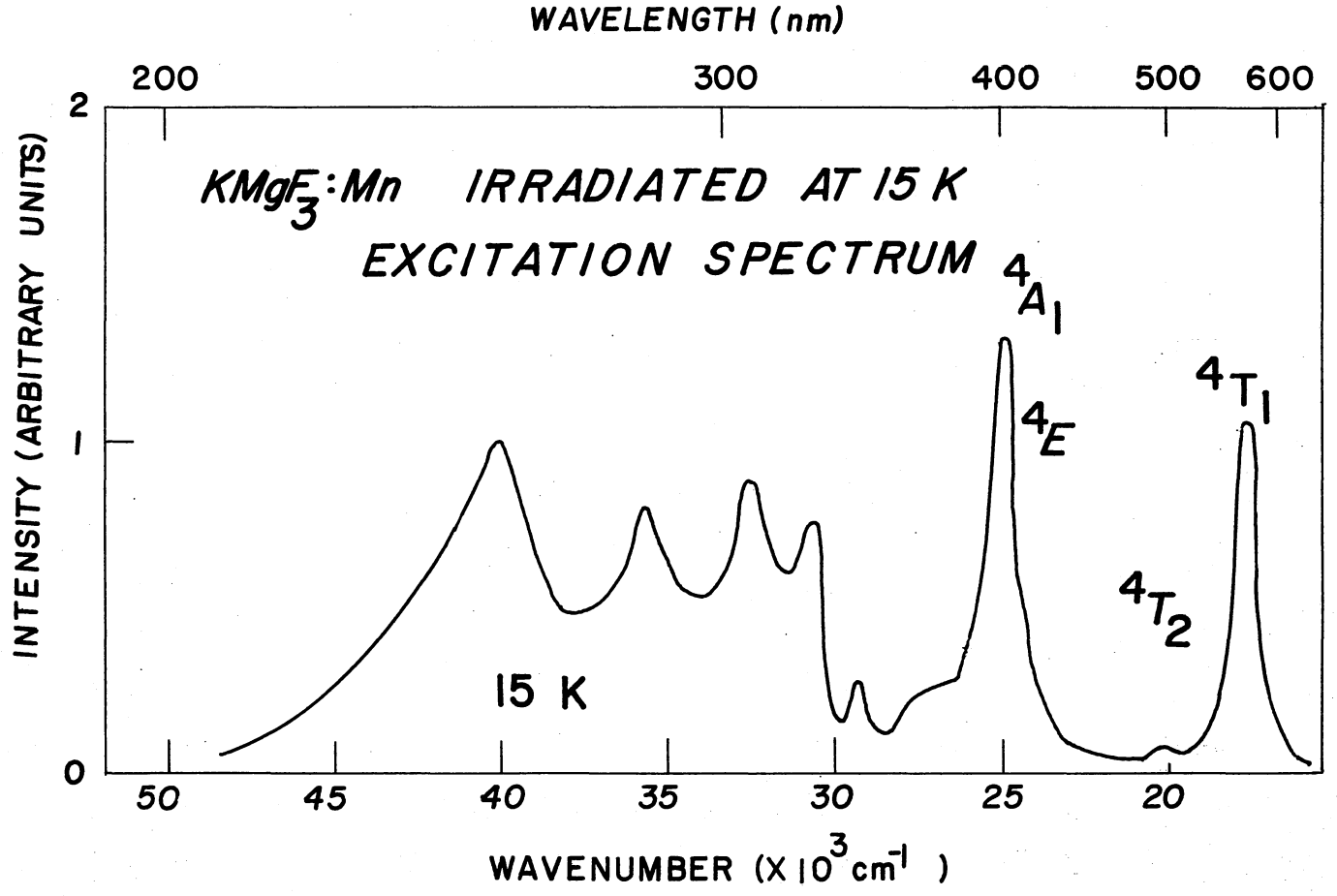

Figure 21. The 15 K Excitation Spectrum for the 680 nm Emission in 15 K Irradiated $KMgF_3$:Mn

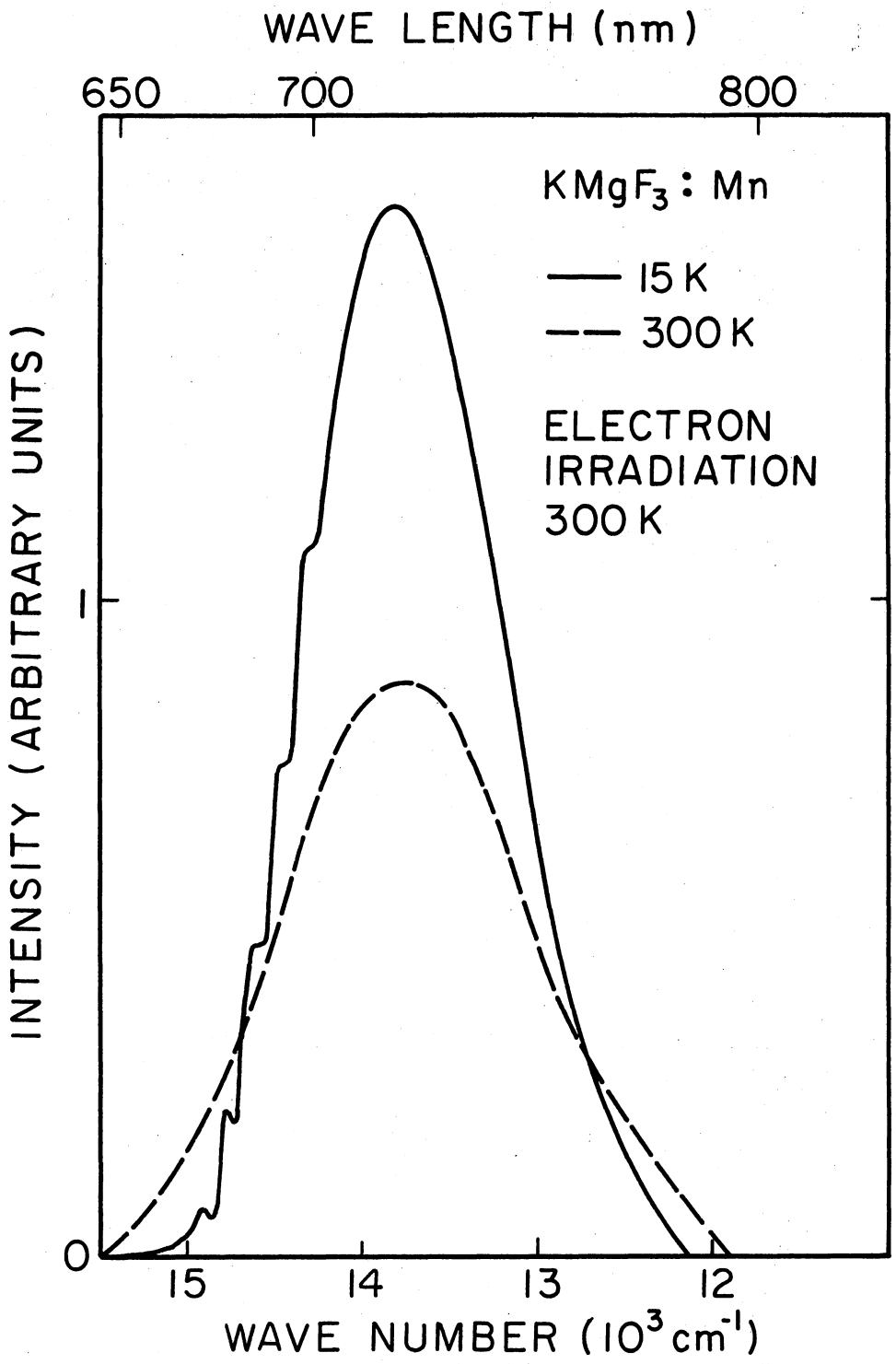

Figure 22. 720 nm Emission Band From 300 K Electron Irradiated $KMgF_3$:Mn Measured at 15 K

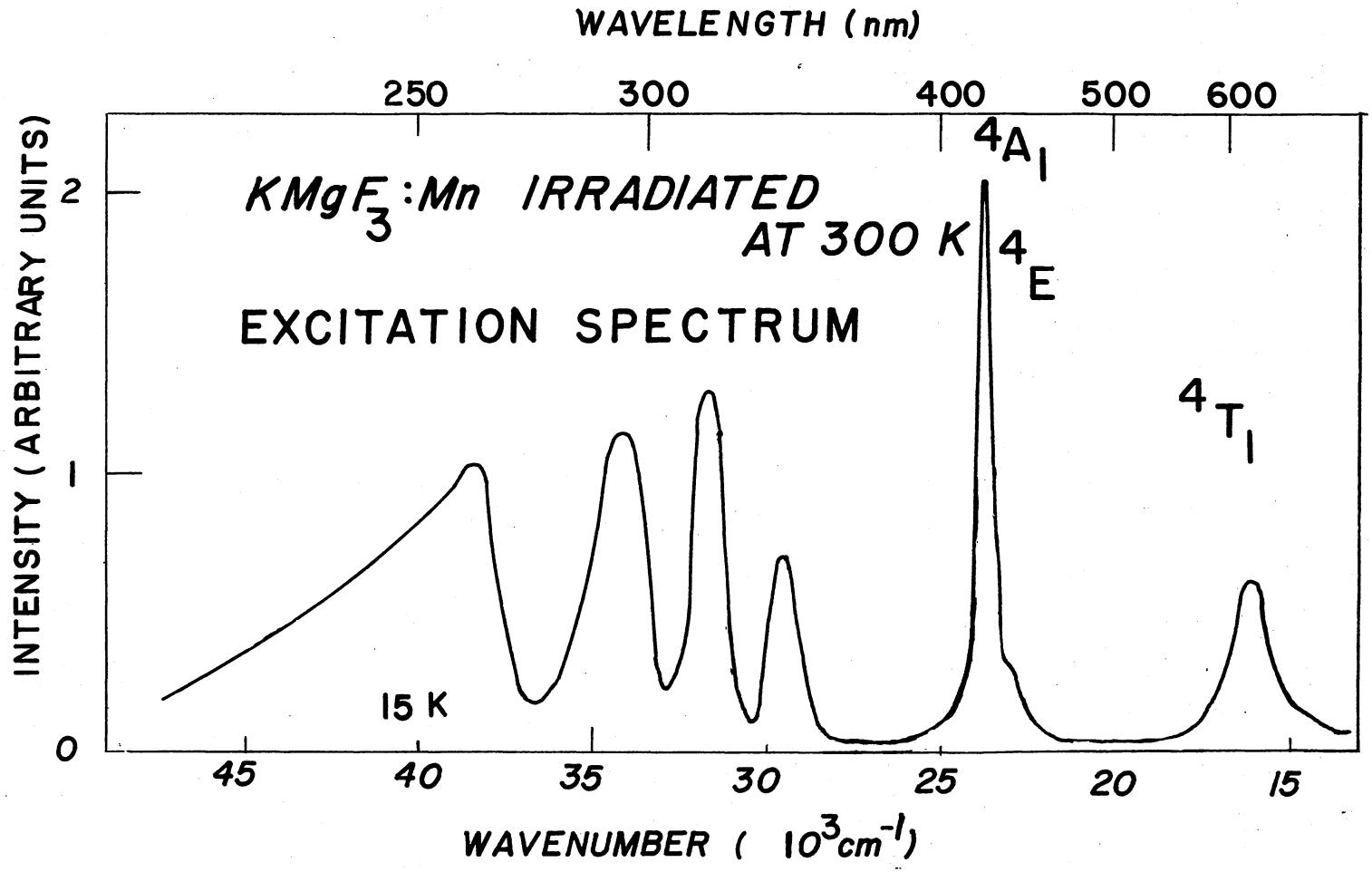

Figure 23. The 15 K Excitation Spectrum for the 720 nm Emission Band From a 300 K Irradiated $KMgF_3$:Mn Specimen

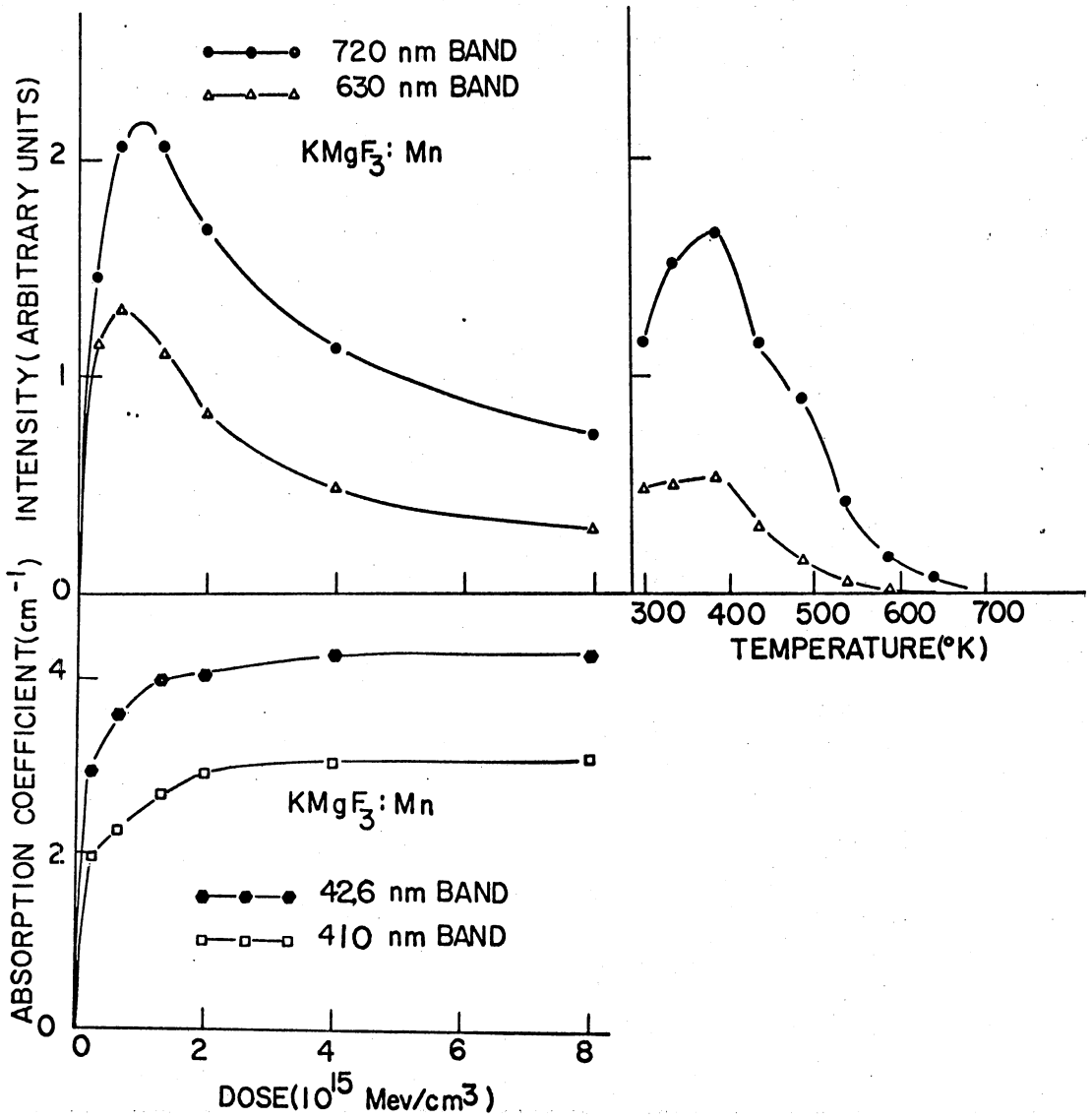

Figure 24. Growth Curves of 630 nm and 720 nm Emission Bands and 426 nm (420 nm 15 K) and 410 nm (406 nm 15 K) Absorption Bands With Radiation Dose. Annealing curves of 630 nm and 720 nm bands from 300 K electron irradiated $KMgF_3$:Mn

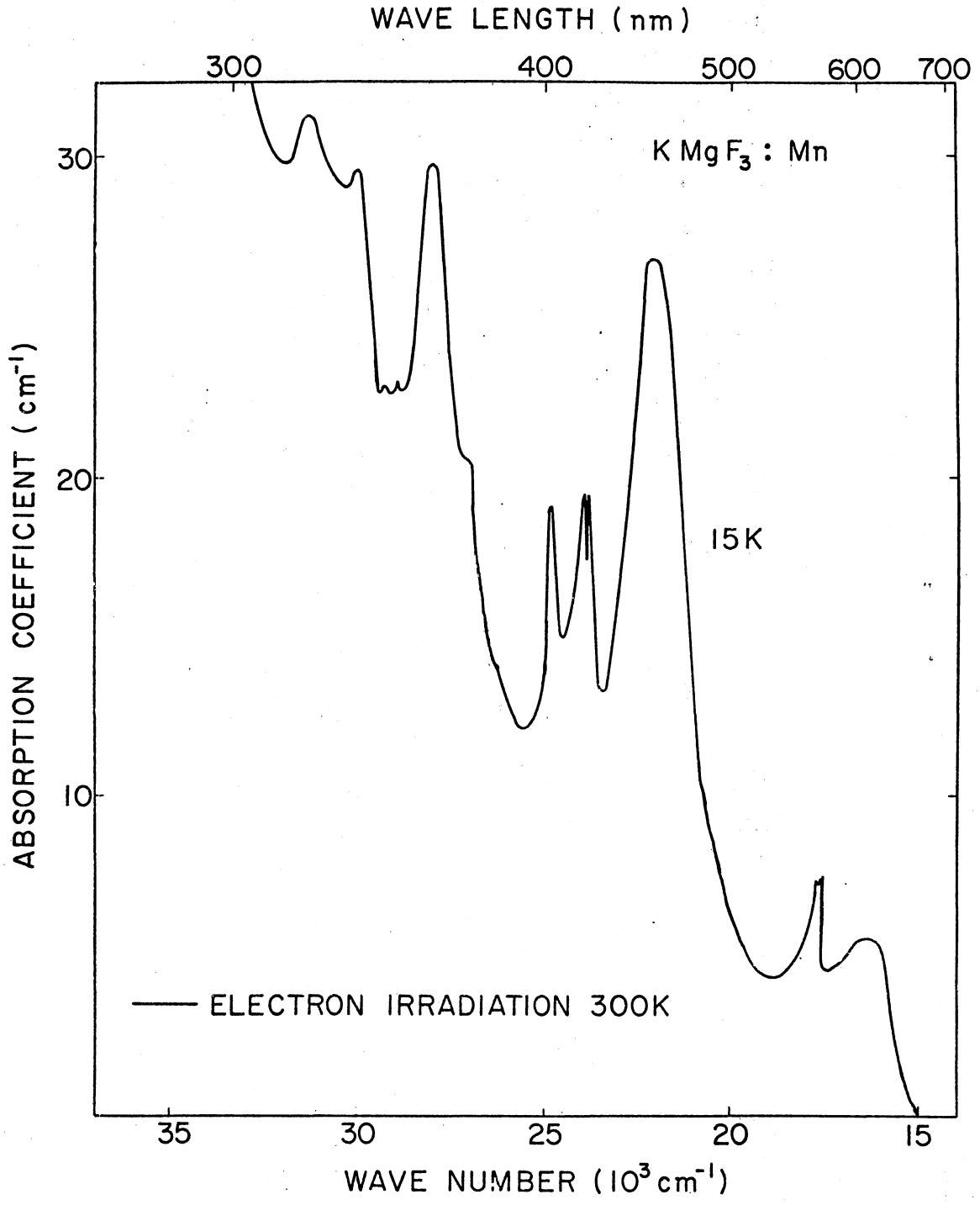

Figure 25. Absorption Spectrum From 300 K Electron Irradiated $KMgF_3$:Mn Measured at 15 K

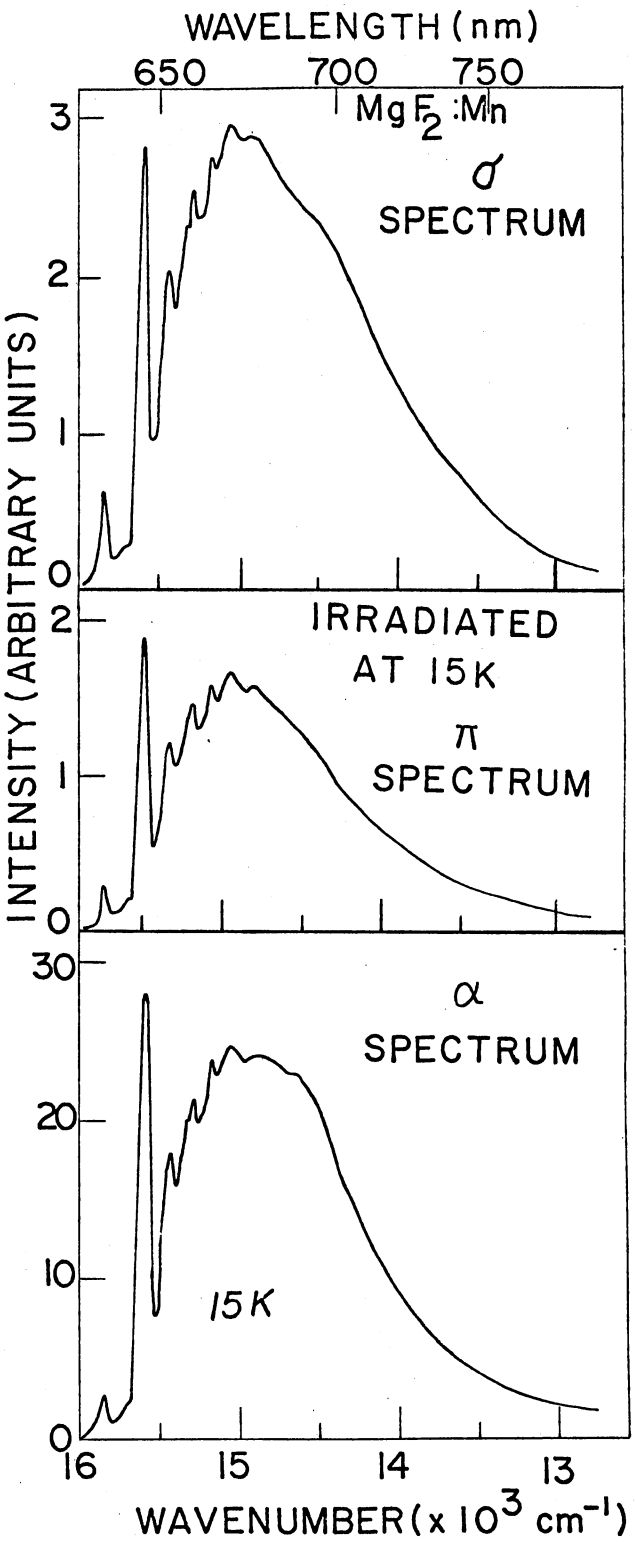

Figure 26. The 670 nm Emission Band From 15 K Electron Irradiated MgF_2:Mn Measured at 15 K

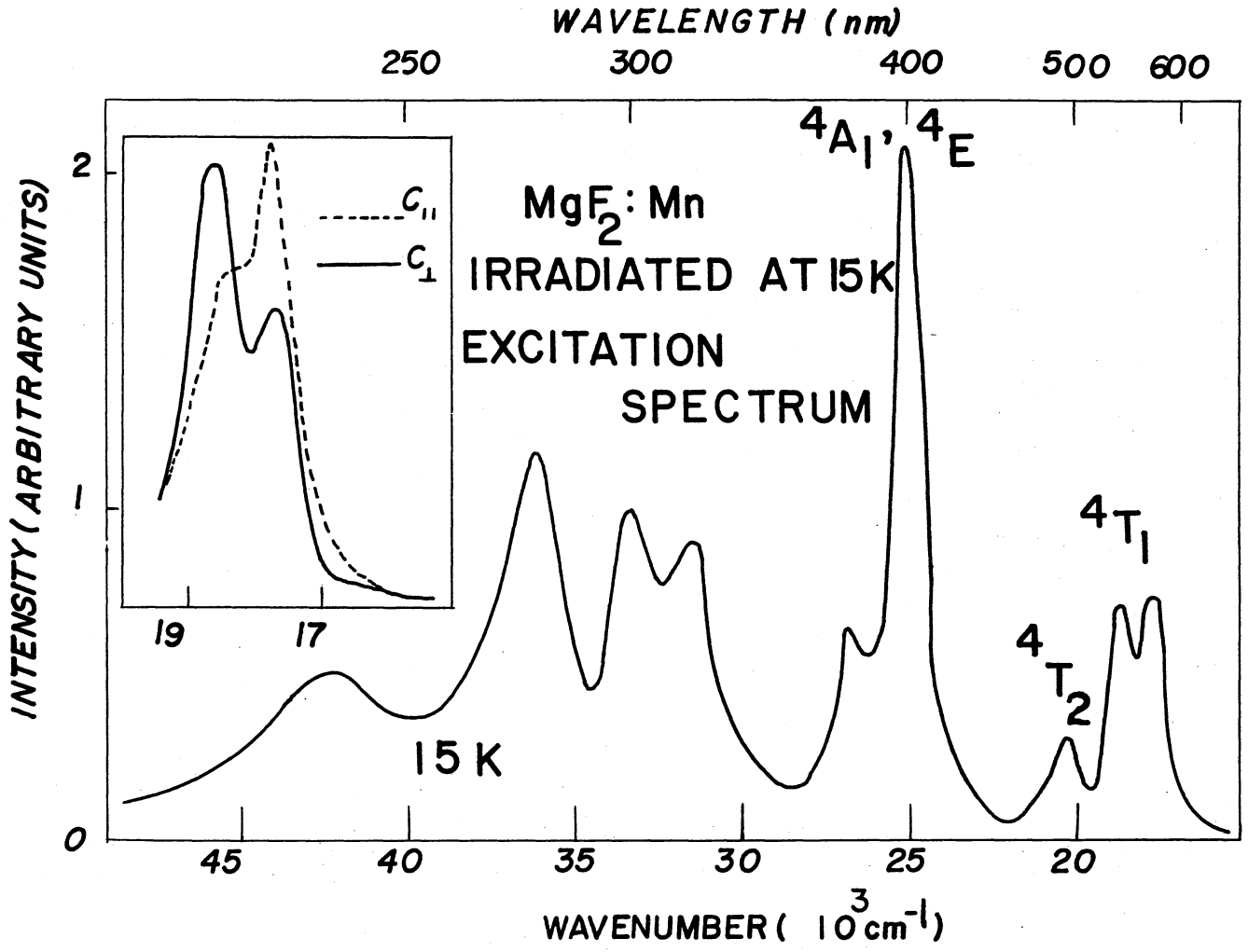

Figure 27. The 15 K Excitation Spectrum for the 670 nm Emission Band From a 15 K Electron Irradiated MgF_2:Mn

crystal, E//c, or perpendicular to the c axis, E $\perp$ c. From the inset it is clear that the two transitions are strongly polarized. The defect responsible for the 670 nm emission forms during room temperature irradiation.

700 nm Emission. A 700 nm emission band, as shown in Figure 28, was observed via using a crystal of MgF_2:Mn irradiated at 300K and measure at 15K. The defect responsible for these emission and excitation bands evidently does not form during low temperature irradiation or after low temperature (either 15 or 77K) irradiation and warming to 300K. The 15K excitation spectrum for the 700 nm band is shown in Figure 29. Although it is inhibited clearly in the figure, a possible excitation peak occurs at 43,000 cm^{-1}; but, because the exciting source is weak in this region, the peak is not clearly observed. It should be pointed out that no splitting of the $^4T_{1g}$ excitation peak is observed for the 700 nm emission.

When the samples are irradiated at 300 K, F-aggregate centers, such as F_2 and F_3 centers, can be observed through both emission and absorption spectra. For low temperature irradiation, no F aggregates are formed.

Table VII indicates the energy differences between the sharp line spectra for the various bands and is presented in such a way that a comparison of $KMgF_3$:Mn and MgF_2:Mn can be made.

Discussion

The emission bands which occur at 590 nm in MgF_2:Mn and at 610 nm in $KMgF_3$:Mn after irradiation are apparently due to "unperturbed" Mn^{2+} ions, since the emission spectra are essentially the same as observed

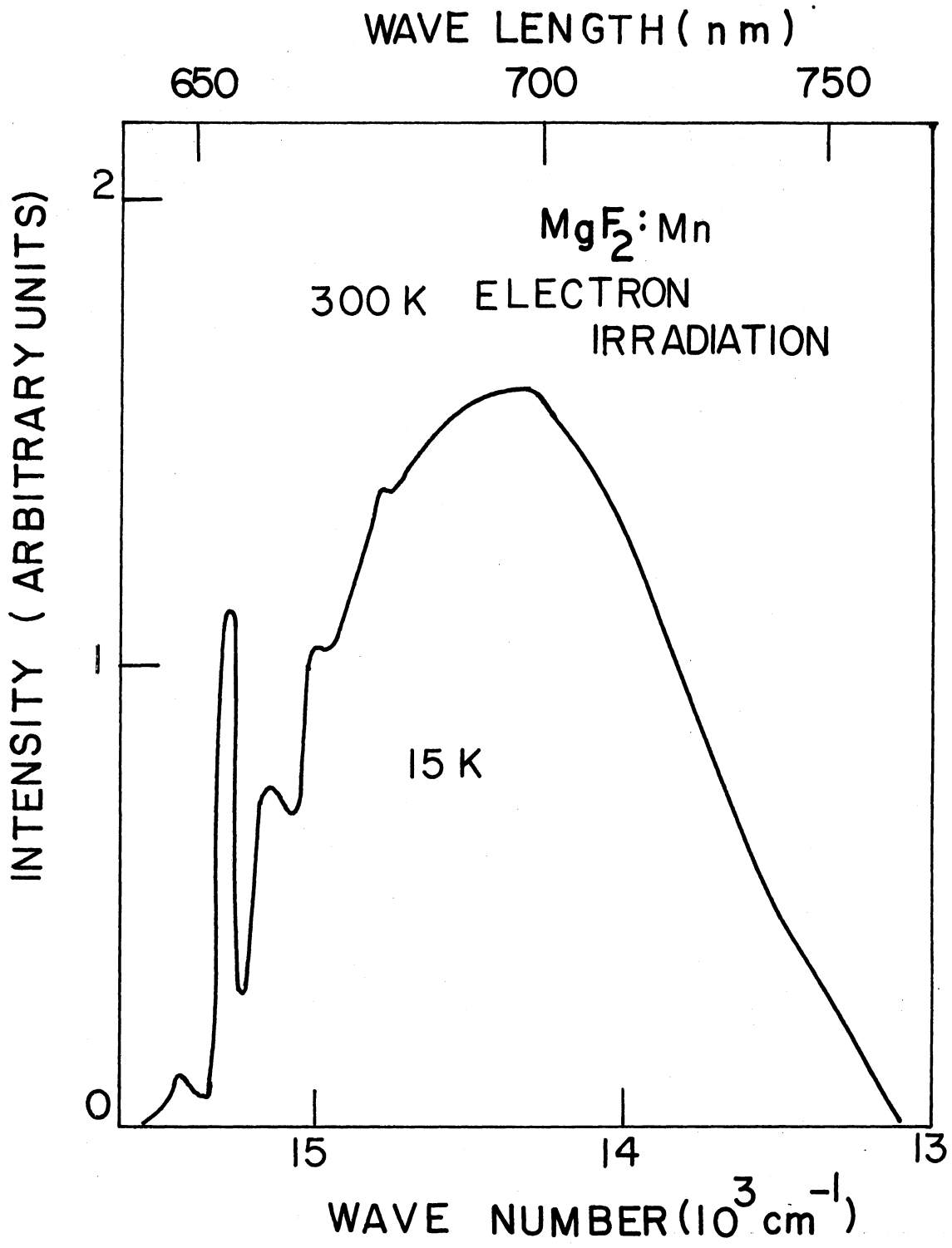

Figure 28. 700 nm Emission Band From 300 K Electron Irradiated MgF_2:Mn Measured at 15 K

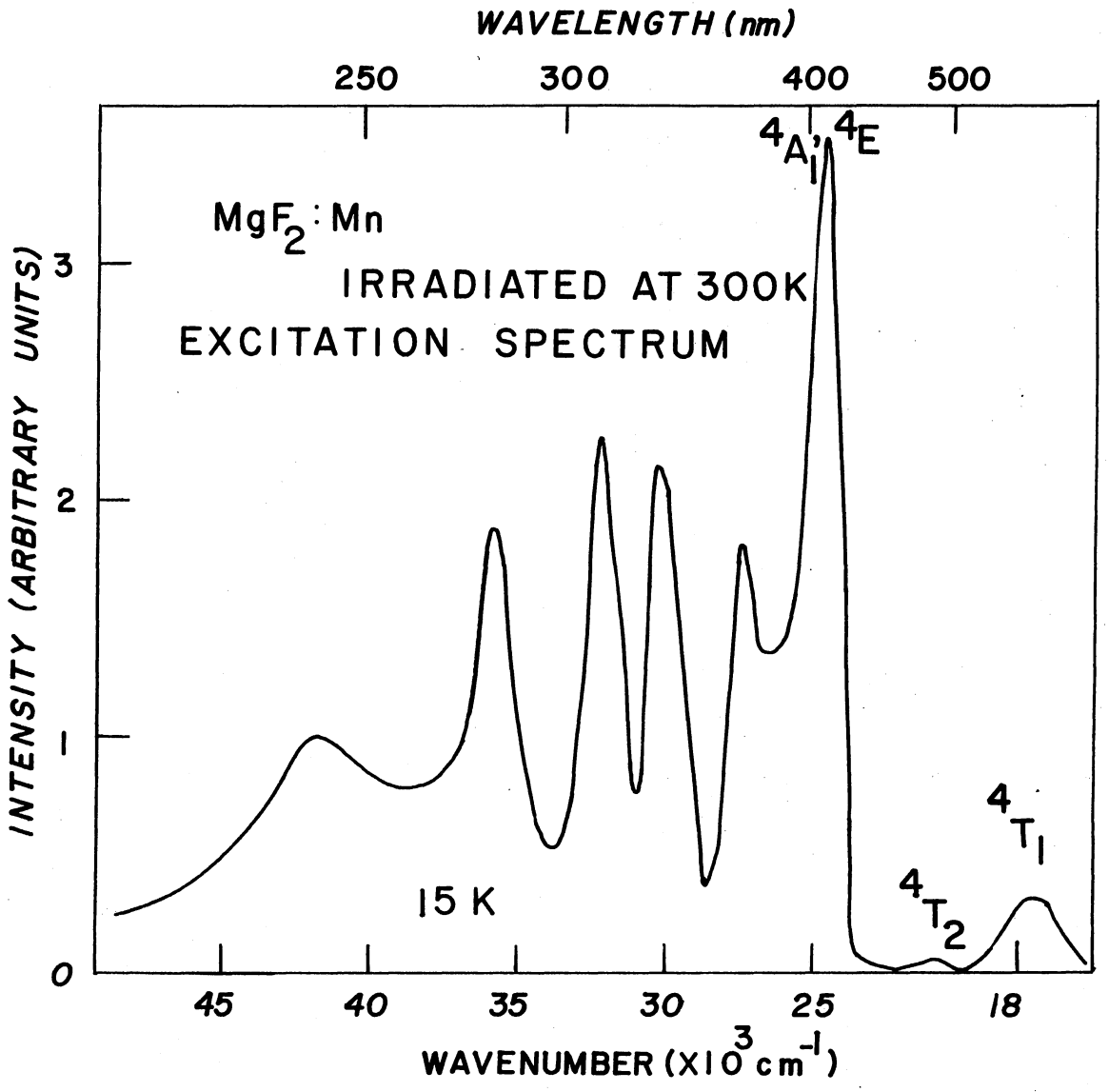

Figure 29. The 15 K Excitation for the 700 nm Emission Band in MgF_2:Mn

TABLE VII

PHONON LINES IN $KMgF_3$:Mn AND MgF_2:Mn

$KMgF_3$:Mn			MgF_2:Mn		
Emission Band (nm)	Peak Position nm (cm^{-1})	Energy Difference (cm^{-1})	Emission Band (nm)	Peak Position nm (cm^{-1})	Energy Difference (cm^{-1})
				α-SPECTRUM	
610	581.0 (17211)	---	590	569.0 (17574)	---
(excitation	585.8 (17070)	141	(excitation	572.8 (17458)	116
365 nm)	588.7 (16986)	225	365 nm)	575.2 (17385)	189
				579.5 (17256)	318
				π-SPECTRUM	
				560.0 (17574	---
				572.5 (17467)	108
				575.0 (17391)	184
				580.8 (17218)	357
				σ-SPECTRUM	
				569.2 (17569)	---
				573.2 (17446)	123
				575.0 (17391)	178
				580.0 (17241)	328
				α,π,σ-SPECTRA	
680	607.4 (16464)	---	670	645.7 (15487)	---
(excitation	610.1 (16391)	73	(excitation	652.0 (15337)	150
409 nm)	615.0 (16260)	204	540 nm)	658.0 (15198)	289
				663.5 (15072)	415
				669.0 (14947)	540

TABLE VII (Continued)

$KMgF_3$:Mn			MgF_2:Mn		
Emission Band (nm)	Peak Position nm (cm^{-1})	Energy Difference (cm^{-1})	Emission Band (nm)	Peak Position nm (cm^{-1})	Energy Difference (cm^{-1})
720 (excitation 420 nm)	670.6 (149.2)	---	700 (excitation 420 nm)	647.5 (15444)	---
	677.8 (14754)	158		654.5 (15278)	166
	684.7 (14605)	307		660.0 (15151)	293
	692.0 (14451)	461		667.0 (14992)	452
	699.1 (14304)	608		677.0 (14771)	673

in MnF_2 and $KMnF_3$. From successive optical bleaching experiments, a linear relation is found between the height of the 450 nm absorption band, shown in Figures 18 and 19, and the 590 or 610 nm luminescence intensity. Furthermore, the after-glow and x-ray excited luminescence spectra from MgF_2:Mn and $KMgF_3$:Mn also show 590 or 610 nm bands. The optical absorption bands for low temperature irradiated crystals are very complex. Some of the complexity can be reduced by taking difference curves. The difference curves are driven by subtracting the absorption after bleaching from the absorption of freshly irradiated crystals. The intensity of the bands as well as the relationship between the Mn^{2+} emission and the height of the 450 nm absorption suggests that some valence state of Manganese is involved. Ikeya and Itoh (91) have done extensive work on Mn^{2+}, Mn^{1+}, Mn^{o} in NaCl. Their data suggest that the 450 nm band shown in Figures 18 and 19 is due to Mn^{o} in a substitutional site. They ascribe the band at about 270 nm to Mn^{1+}. The observations obtained here so far are certainly not at variance with their tentative assignments; however, before these suggestions can be substantiated, a need to do more experiments and check-ups cannot be obliterated. Reviewing the enhanced data, it seems that Mn^{1+} centers, with charge compensation from X_2^- centers, are involved. This assumption would lead to the possibility of Mn^{2+} emission each time an electron is lost from an Mn^{1+} center or an X_2^- center recombines with Mn^{1+}. However, the <100> defect symmetry indicated from the polarized optical bleach suggests influence from another nearby defect. The presence of a 700 nm absorption band for $KMgF_3$:Mn, not for MgF_2:Mn is a mystery.

The emission and excitation bands which are intense at $300^{o}K$ and are irradiated in MgF_2:Mn and $KMgF_3$:Mn can be attributed to Mn^{2+} ions

with F centers as next neighbors. At room temperature, the radiation-induced interstitials are mobile and agglomerate. At low temperatures the interstitials should be immobile and other emission and absorption or excitation bands should be observable because of the presence of these defects.

In both $KMgF_3$:Mn and MgF_2:Mn, the intense emission bands are different for the different radiation temperatures. The excitation transitions labeled $^4A_1$, ^4E, and $^4T_2$ are enhanced for the low temperature irradiations compared to the 300°K irradiation. Moreover, for MgF_2, as seen in Figure 27, it is clear that the $^4T_1$ transition is split. From polarized light data, shown in the inset of Figure 27, the dipole direction for the defect responsible for these transitions, and the symmetry of the Mn^{2+} defect complex can be found. Previously, it was indicated that the 300°K irradiation induced bands are due to Mn^{2+}-F-center defects. Since the low temperature emission bands and excitation spectra are different, the data are perhaps best explained by assuming that nearby interstitials cause the changes in the optical properties. If this proposal is correct, an analysis of the polarized light data in Figure 27 suggests that the interstitials in 15°K irradiated MgF_2 crystals are located at the center of the triangle connecting the three neighboring Mg ion sites in a {110} plane.

In the case of irradiated $KMgF_3$:Mn, it is reported that the 630 nm emission arises from a symmetry split level of the $^4T_{1g}$ level and that the A_2 level of this symmetry split level is 400 cm^{-1} below the 630 nm level. It can be seen in Figure 25 that the 563 nm absorption band from which this 630 nm emission originates is split into two bands 63 cm^{-1} apart. The absorption intensity of these two bands is about the

same suggesting the transitions are allowed. It is believed that this suggests that the 563 nm $^4T_{1g}$ level is split into three levels (B_1 + B_2 + A_2) in C_{2v} symmetry by the presence of the low temperature radiation induced defects. The $A_2 \rightarrow A_1$ transition being responsible for the 680 nm emission observed at low temperature. The apparent C_{2v} symmetry of the defect can adequately be explained by a split interstitial-Mn^{2+}-F-center complex. In fact, Ikeya and Itoh (91) have described a split interstitial-ion-Mn^{2+} center from their EPR data on irradiated NaCl:Mn^{2+} which, if an F center were present, would be very much like the model is proposed here. Figure 30 gives a tentative idea of the models in $KMgF_3$:Mn and MgF_2:Mn.

Table VIII gives a summary of the irradiation observations with a tentative identification of the defects responsible for each emission band.

Polarized Optical Transition From Mn^{2+}-F Center

First it must be illustrated that the spectrum in Figure 23 are actually associated with Mn^{2+} impurity. In an attempt to ascertain this the polarized excitation spectrum from $KMgF_3$:Mn was measured. The sample was illuminated with light propagating along a [001] crystal axis having its electric vector oriented along [100] or [010] crystallographic directions. The detected emitted light propagated along a [010] direction and the polarizers were oriented to pass the [100] or [001] electric vectors. The 720 nm emission band was used to monitor the excitation spectrum. This emission band arises from a transition between a perturbed $^4T_{1g}$ level (the presence of an F center reduces the symmetry of a Mn^{2+} site from O_h to C_{4v} with a commensurate decomposition of the energy

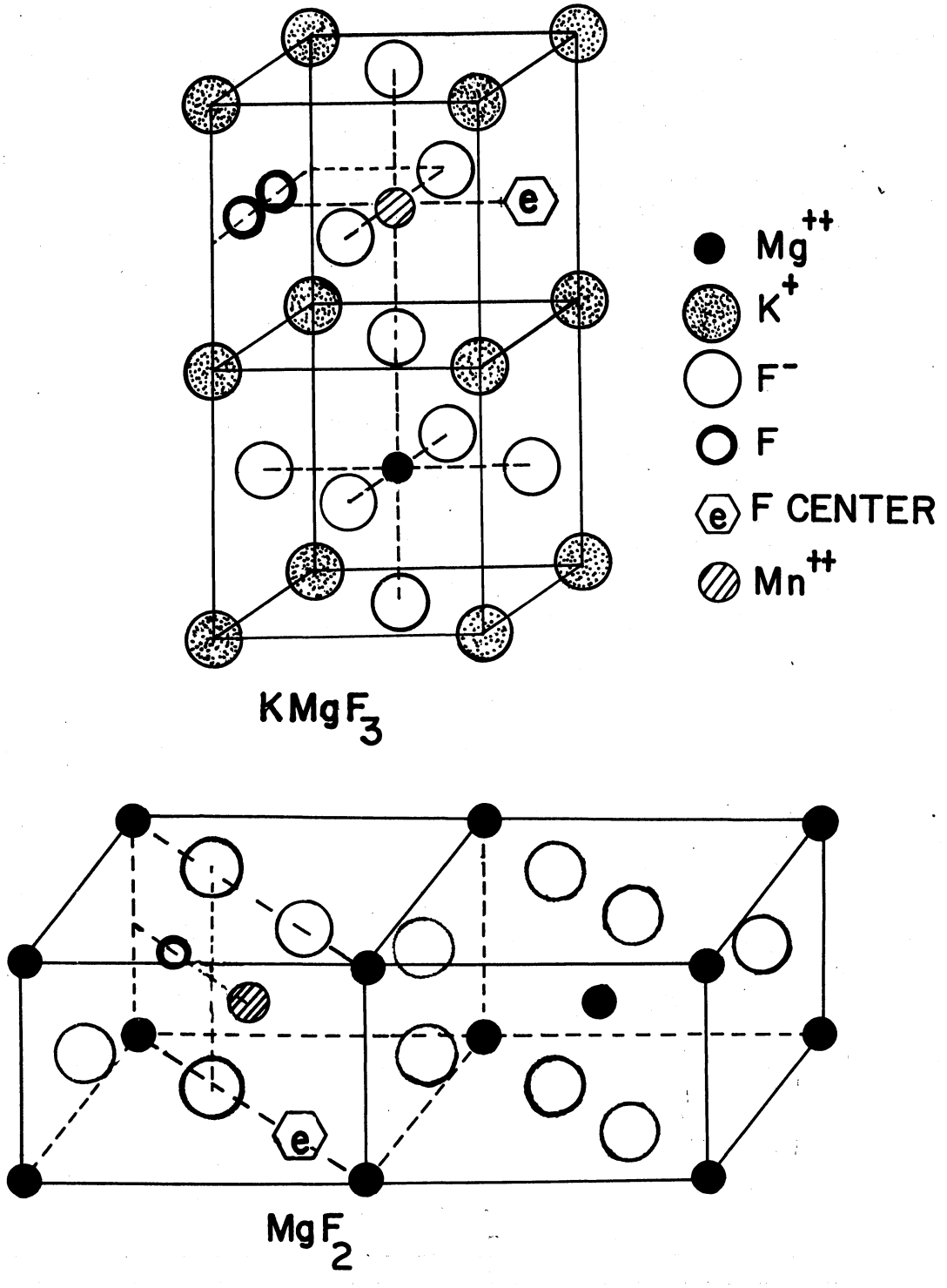

Figure 30. Schematic Suggestion for the Mn^{2+}-F-Center-Interstitial Complex Configuration in $KMgF_3$ and MgF_2

level symmetry to A_2 + E) and the $^6A_{1g}$ (in the perturbed state A_1) ground state. For electric dipole transitions between these levels only transitions perpendicular to the defect axis, π transition, are allowed while the transitions along the defect dipole axis, σ, are forbidden. This means that the 720 nm emission should be polarized. Moreover, since the 612 nm absorption band levels must be A_2 + E symmetry this absorption must be π polarized. The 420 nm levels are of A_1 and B_1 symmetry and hence the transition is σ polarized. With this in mind, a table can be constructed predicting the effects polarized excitation and emission. The intensity of the emission stimulated by [100] polarized light and measured through a [100] oriented polarizer is designated as I_{11}. For [100] exciting light and a [001] analyzer the intensity is I_{21} and for [010] exciting light and a [001] analyzer the intensity is written I_{22}. In the case of unpolarized exciting light, I_{1u} and I_{2u} are designated for the analyzer oriented along [100] and [001], respectively. The intensity can be calculated by the following equation (59,92),

$$I_{jl} = \rho \sum_i n_i |\hat{r}_i^{\beta_1} \cdot \hat{U}_j|^2 |\hat{r}_i^{\beta_2} \cdot \hat{U}_l|^2 ,$$

where n_i is the number of dipoles in r_i orientation and n_i is constant for random distribution case, l and j are the polarization of excitation and emission respectively, U_j and U_l are the polarization of the light, and β_1, $\beta_2 = \sigma, \pi_1, \pi_2$. Table IX shows the predicted and measured for 720 nm light as shown in Figure 31 assuming that these transitions are from perturbed Mn^{2+} center. The agreement certainly suggests that these are perturbed Mn^{2+} transitions.

TABLE VIII

SUMMARY OF IRRADIATION DATA

Band and Material	Wavelength (nm)	Temp. of Observation	e-irradiation Low Temp.	e-irradiation Low Temp. Warm to Room Temp.	e-irradiation Room Temp.	e-irradiation X-ray, Optical Low Temp.	Nature of Defect
610 - $KMgF_3$:Mn		15K	--	--	--	Yes-Decays	Mn^{2+} (Unperturbed)
590 - MgF_2:Mn		15K	--	--	--	Yes-Decays	Mn^{2+} (Unperturbed)
680 $KMgF_3$:Mn		15K	Yes	Yes Decreases	Yes	----	Mn^{2+}- F-Interstitial
670 MgF_2:Mn		15K	Yes	Yes Decreases	Yes (Weak)	---	Mn^{2+} F-Interstitial
720 $KMgF_3$:Mn		15K	Yes (Weak)	Yes (Weak)	Yes	---	Mn^{2+}-F
700 MgF_2:Mn		15K	No	No	Yes	---	Mn^{2+}-F
340 $KMgF_3$:Mn		15K	----	----	---	X-Ray, Yes	X_2^- (?)
390 MgF_2:Mn		15K	----	----	---	X-Ray, Yes	X_2^- (?)

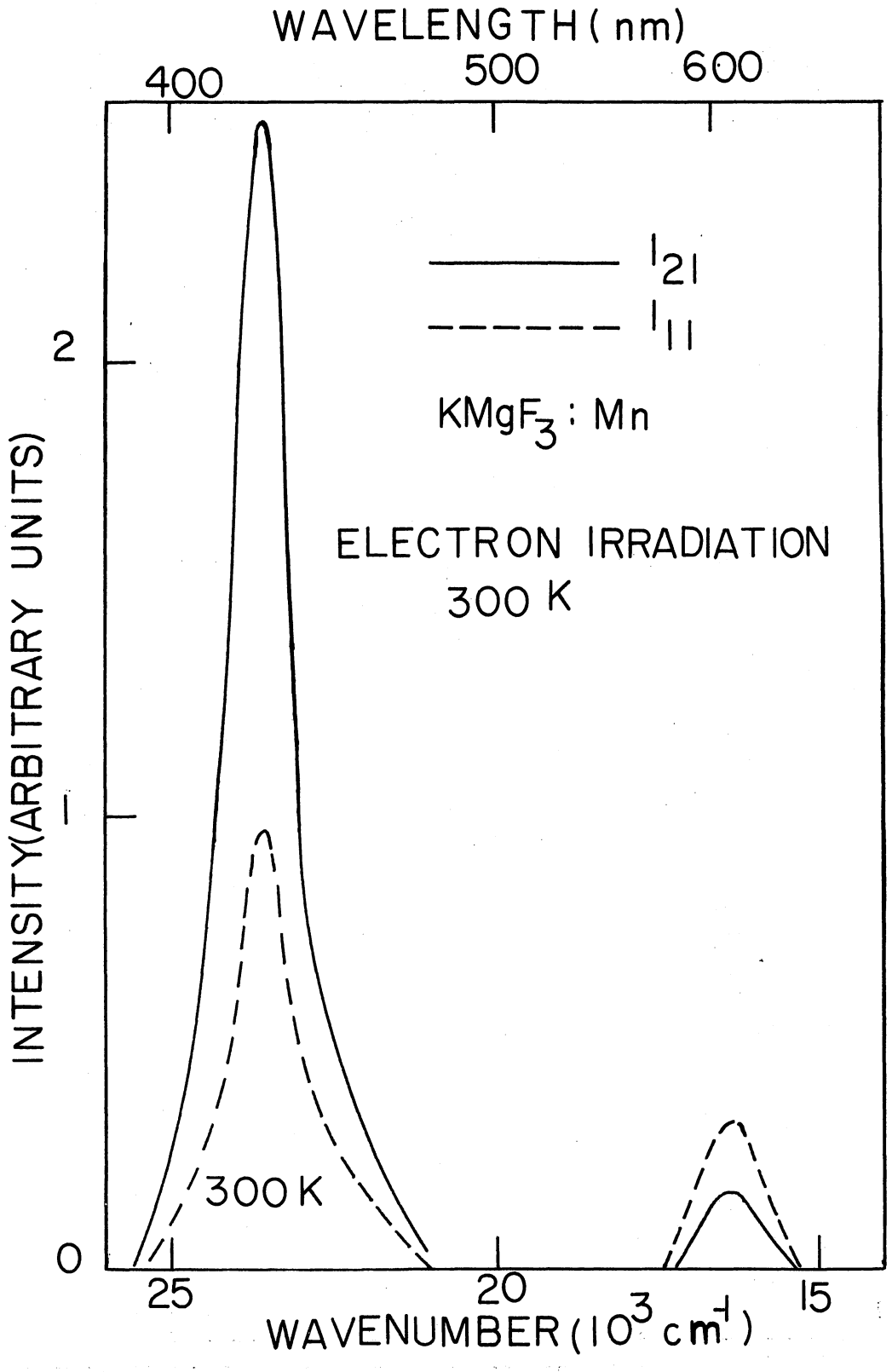

Figure 31. Polarized Excitation

TABLE IX

POLARIZED ABSORPTION FROM IRRADIATED $KMgF_3$:Mn

	612 nm Absorption			420 nm Absorption		
	I_{21}/I_{11}	I_{12}/I_{22}	I_{1u}/I_{2u}	I_{21}/I_{11}	I_{12}/I_{22}	I_{1u}/I_{2u}
Predicted	0.5	1.0	1.5	∞	1.0	0.5
Observed	0.5	1.1	1.4	3.0	1.1	0.8

Interaction Between F Center and Mn^{2+}

The absorption spectra of electron irradiated $KMgF_3$:Mn both before and after a mercury light optical bleach for two hours at 15°K are portrayed in Figure 32. It should be noted that although the bands at 612 nm (16,330 cm^{-1}) and 417 nm (24,000 cm^{-1}) decrease markedly with bleaching the sharp bands at 568 nm (17,000 cm^{-1}) and 403 nm (24,800 cm^{-1}) retain their intensity even though the background absorption changed. However, at 300°K it is possible to bleach the 417 nm and 568 nm bands with F light. The broad band at 454 nm (22,000 cm^{-1}), which is possibly due to perturbed F_2(M) centers, is also decreased by the low temperature bleach. The band at 417 nm (24,000 cm^{-1}) is split by 119 cm^{-1} which may be due to the split of ^4G of free ion Mn^{2+} into $^4A_{1g}$ and ^4E_g. The background absorption caused by the presence of a number of radiation induced defects makes it difficult to study Mn^{2+}-radiation defect absorption; however, the excitation spectra have been used to obtain a clearer idea of the optical transitions of these defects.

As mentioned earlier, the optical transitions for Mn^{2+} in O_h sym-

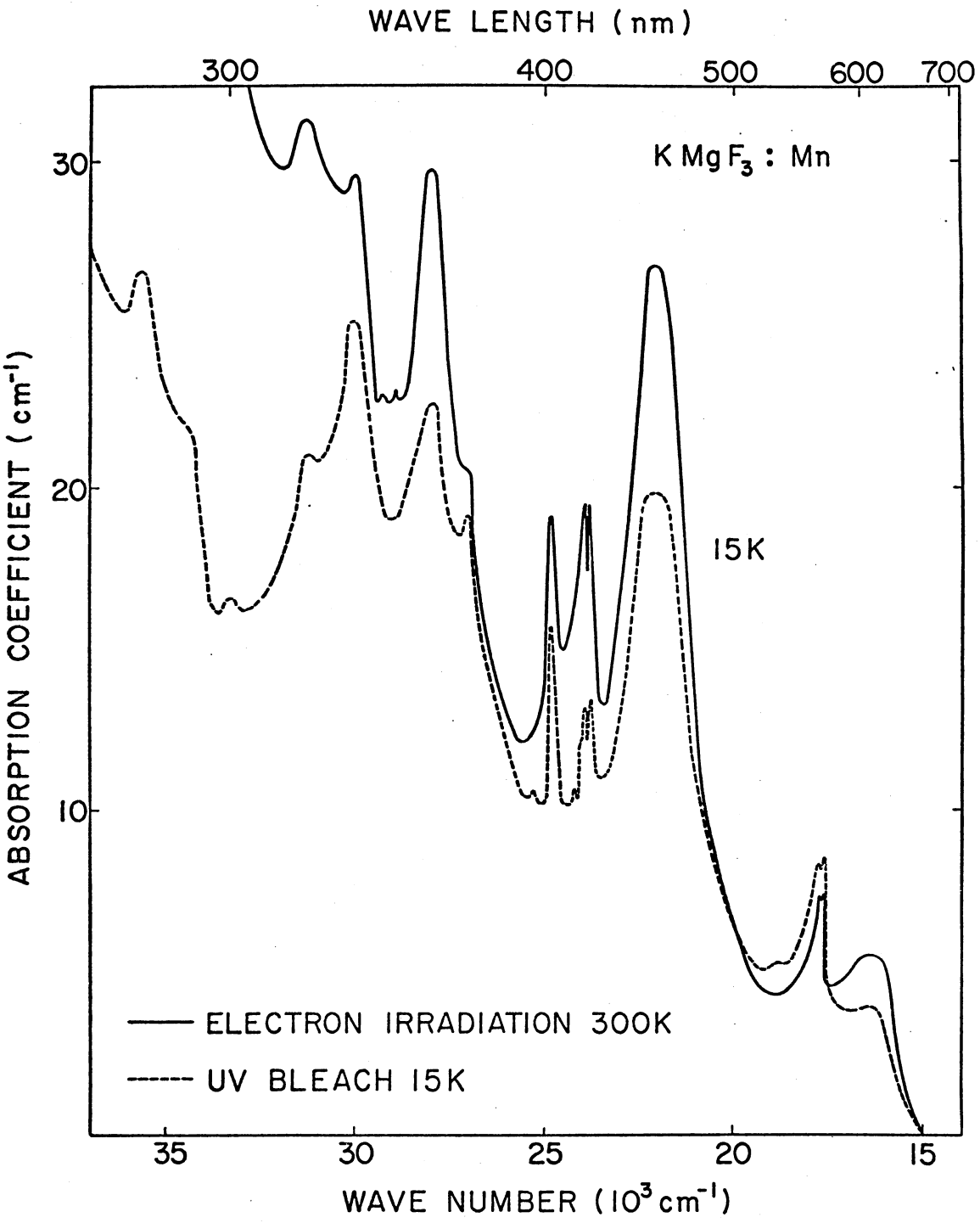

Figure 32. Bleach Effect of Absorption Spectrum From 300 K Electron Irradiated $KMgF_3$:Mn Measured at 15 K

metry are both spin and symmetry forbidden. In order to determine if the increased oscillator strength is due to site symmetry change or to exchange interactions between the Mn^{2+} and a neighboring F center, as has been tentatively proposed, the following experiment has been done. An irradiated sample is bleached with ultraviolet light at $15^{o}K$. This releases electrons from the F centers into other traps, but at this low temperature the empty vacancy is not mobile and the site symmetry remains almost the same as for the F center-Mn^{2+} defect (93). Examining the data in Figure 33, it is believed that optical bleaching causes a marked decrease in the intensity of the spectrum. If site symmetry alone is responsible for the oscillator strength changes, then this reduction will not occur. Therefore, it is justified in indicating that exchange plays a major role in enhancing the optical transitions in this material.

Co^{2+} Emission in $KMgF_3$

Results

When $KMgF_3$:Co is irradiated at $300^{o}K$, a number of new emission bands are detected. Three of these do not appear to be due to simple radiation induced defects such as F_2 centers, but have half-widths and vibronic structure more closely resembling that of 3d impurity transitions. These bands are portrayed in Figures 34-36. The bands at 875 nm (11,400 cm^{-1}) and 830 nm (12,000 cm^{-1}) have the same excitation spectra, but the 658 nm (15,000 cm^{-1}) band has a quite different excitation spectrum. On the other hand, all three bands appear to grow equally with radiation, and the data illustrated in Figure 37 which is a plot of the intensities of zero phonon lines associated with these bands

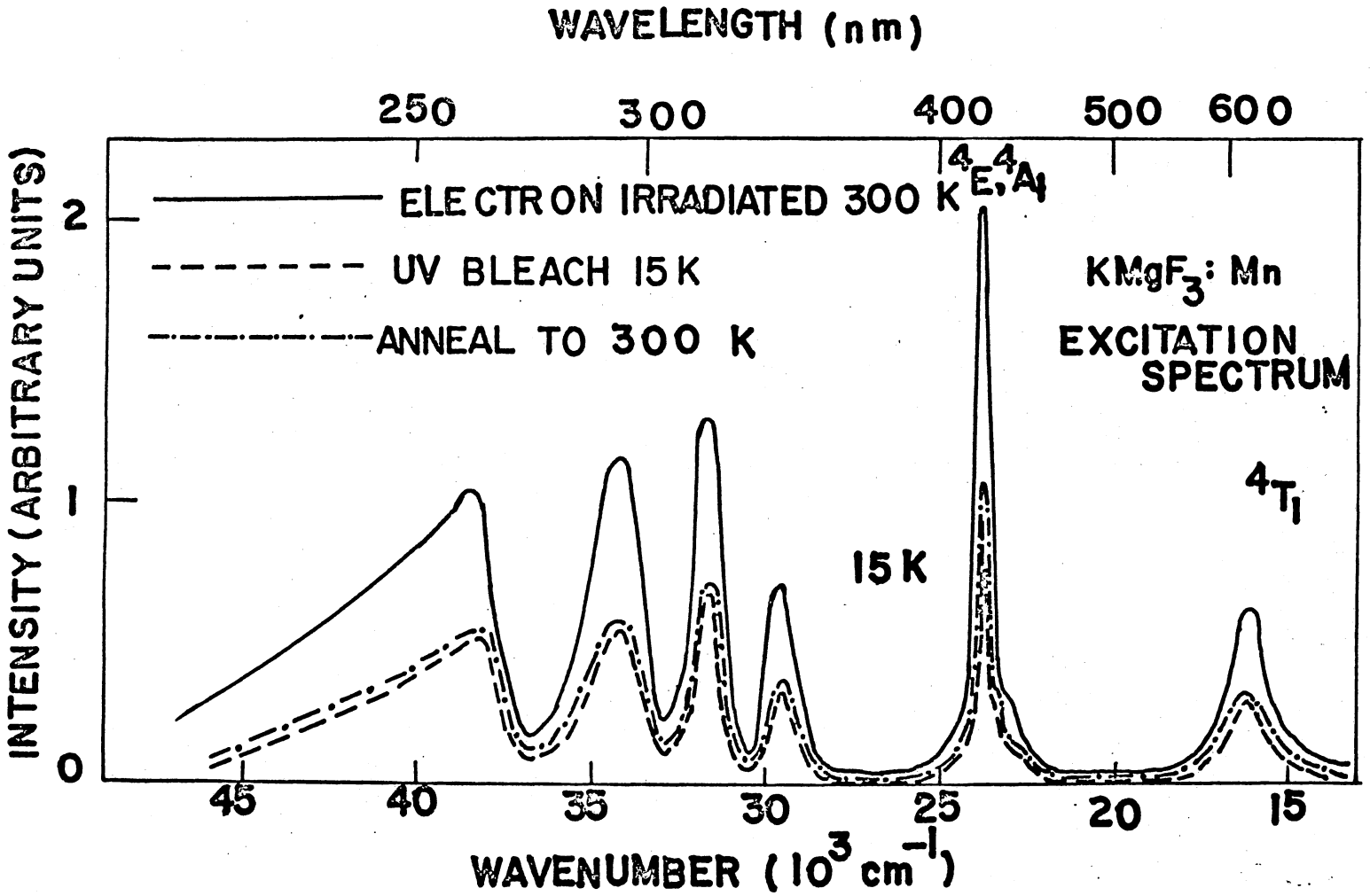

Figure 33. Bleach Effect of Excitation Spectrum for the 720 nm Emission Band of Irradiated $KMgF_3$:Mn

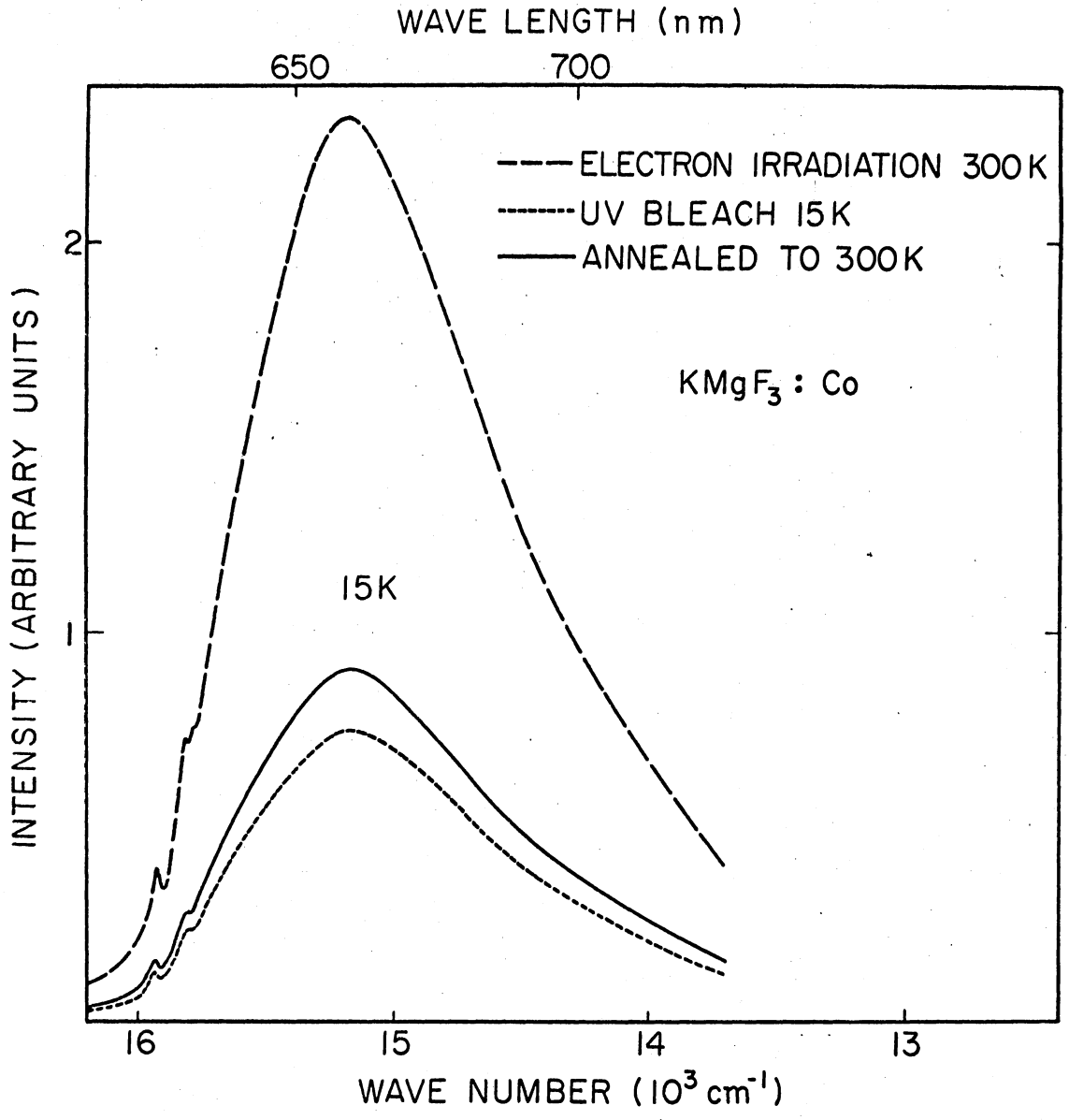

Figure 34. 658 nm Emission Band From 300K Electron Irradiated $KMgF_3$:Co Measured at 15 K

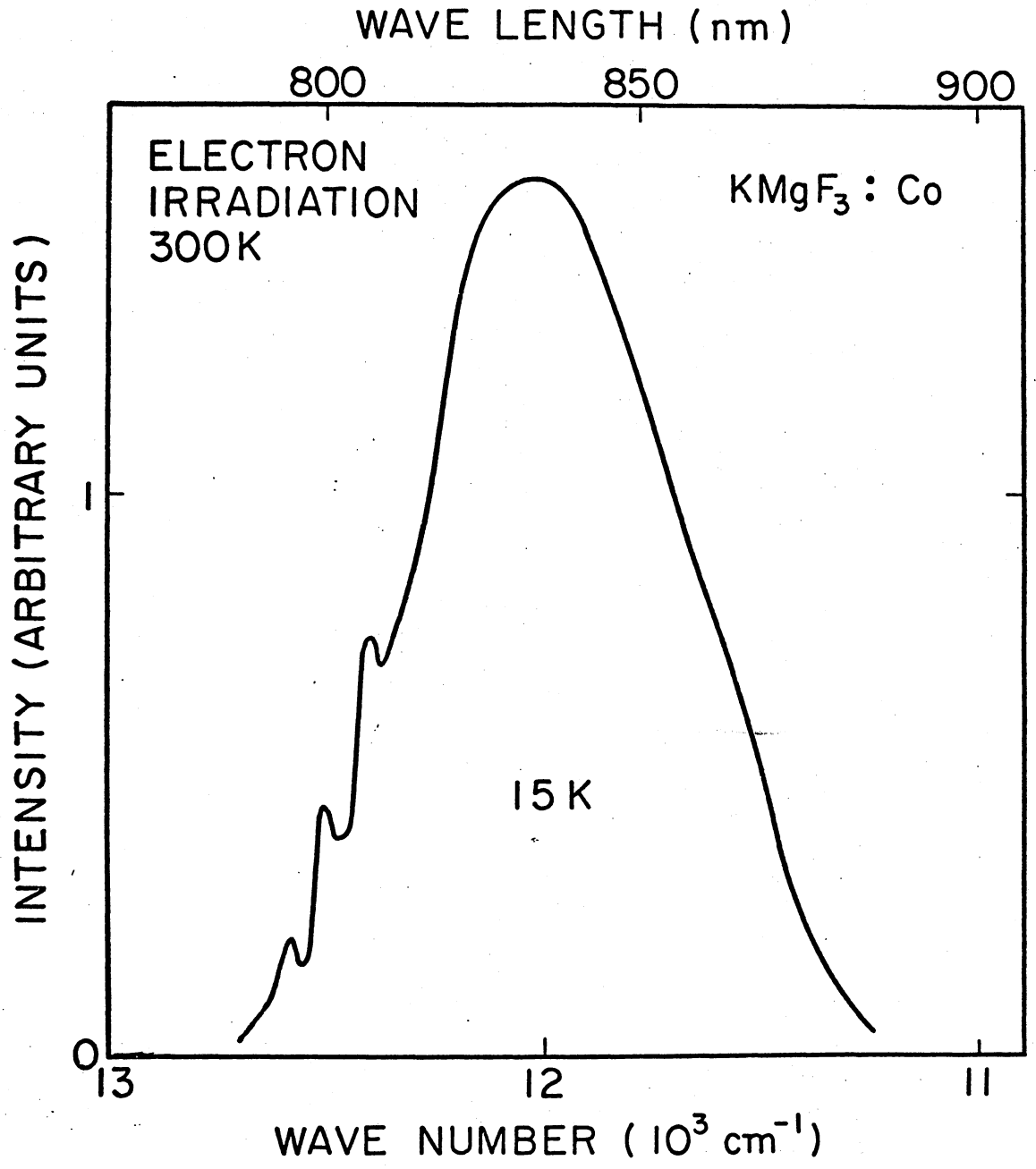

Figure 35. 830 nm Emission Band From 300 K Electron Irradiated $KMgF_3$:Co Measured at 15 K

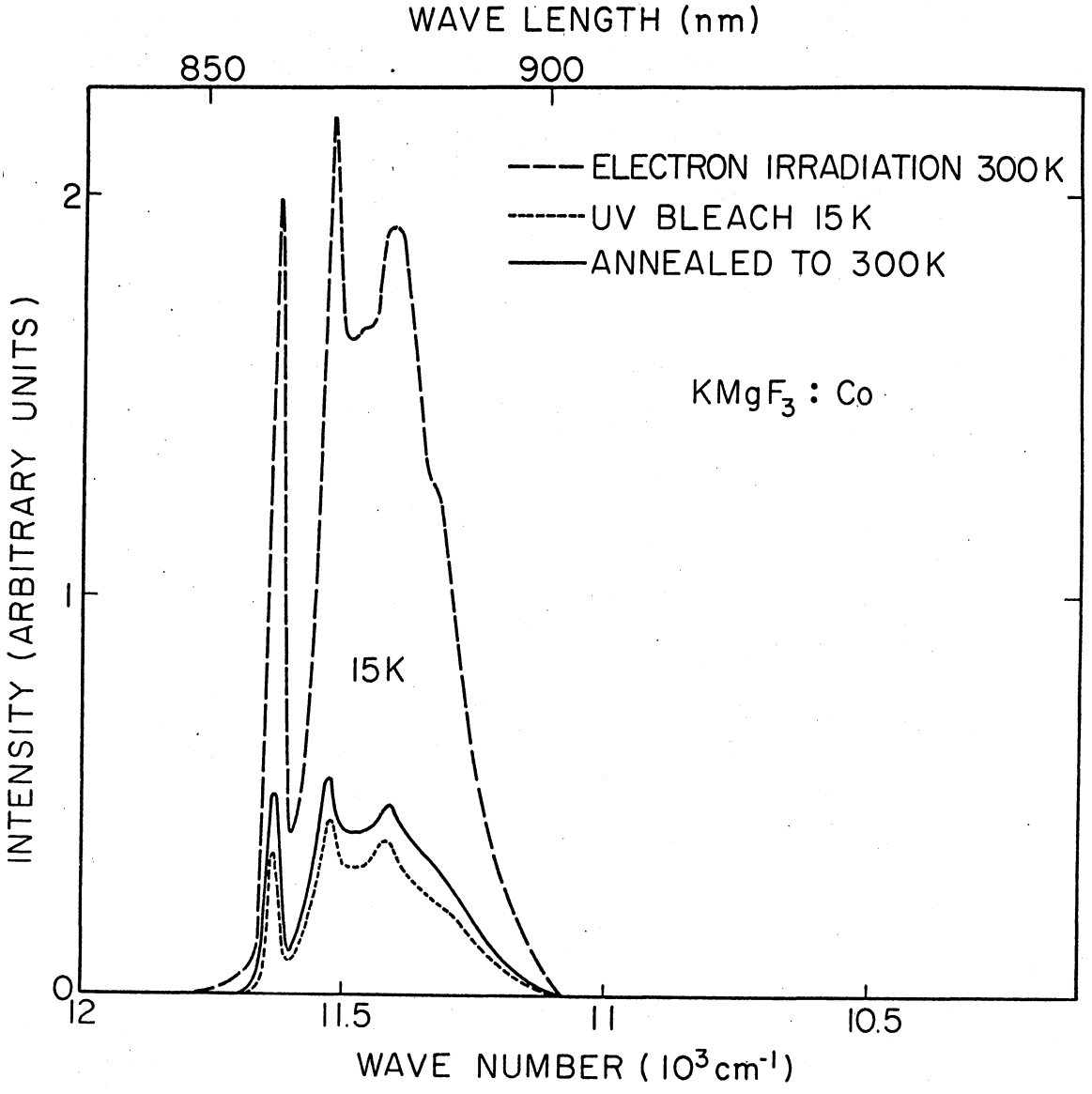

Figure 36. 875 nm Emission Band From 300 K Electron Irradiated $KMgF_3$:Co Measured at 15 K

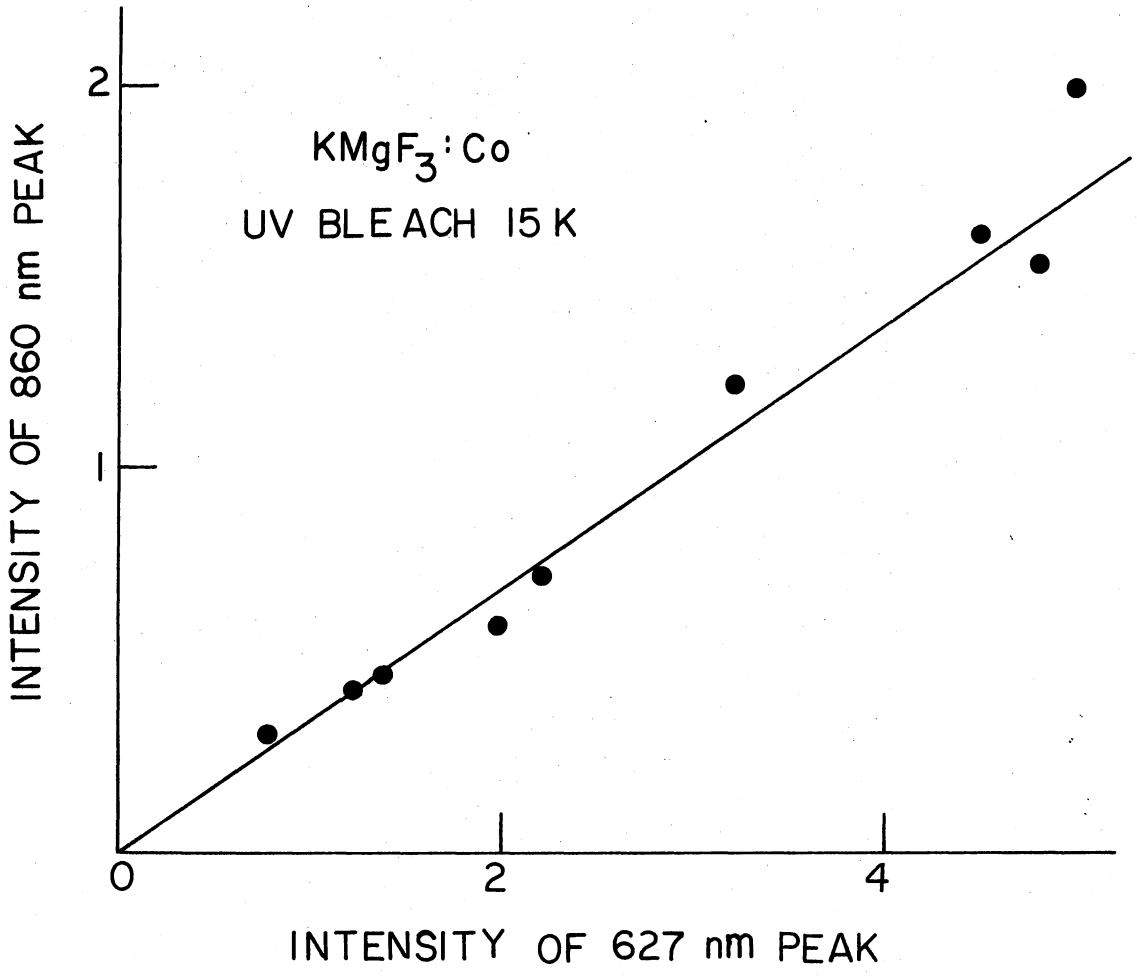

Figure 37. The Intensity Relationship of Zero Phonon Lines of 875 nm and 658 nm Emission Bands as a Function of Radiation Dose and Optical Bleaching

with optical bleaching suggests that the 658 nm (15,000 cm^{-1}) band and the other two come from the same defect complex. In order to determine if optical bleaching in the F band region (280 nm) would decrease the intensity of these bands as it does for Mn^{2+}-F-center complexes the sample were bleached at 15°K. The results are shown in Figures 34 and 36 and were similar for all three bands. If the crystals were warmed to room temperature after bleaching some recovery took place just as in the Mn^{2+} case. Since the growth of the bands with radiation appear to be the same and the effect of optical bleaching on all three is the same, it seems to suggest that these three bands are due to a Co^{2+}-F-center complex and whose increase in intensity, as compared with unperturbed Co^{2+}, is due to exchange interactions. The excitation spectrum for the three bands is shown in Figure 38. It should be noted that excitation at 445 nm yields an M center emission at 585 nm which can give problems in measuring the 658 nm excitation spectrum. This effect has been corrected in Figure 38.

Discussion

The Tanabe-Sugan diagram (13), as shown in Figure 39, for $3d^7$ ions indicates that the temperature dependence of the emission band energies can be predicted. For a transition between the ^2E_g (A_1 + B_1 perturbed) level and the ground state $^4T_{1g}$ level, the peak should shift to higher energy at higher temperatures. This behavior is exhibited by the 875 nm emission band as portrayed in Figure 40, and this emission is tentatively assigned to the transition between these two levels. The peak of the emission transition between the $^4A_{2g}$ (B_1 perturbed), and the $^4T_{1g}$ ground state should move according to an analysis of the Tanabe-Sugane

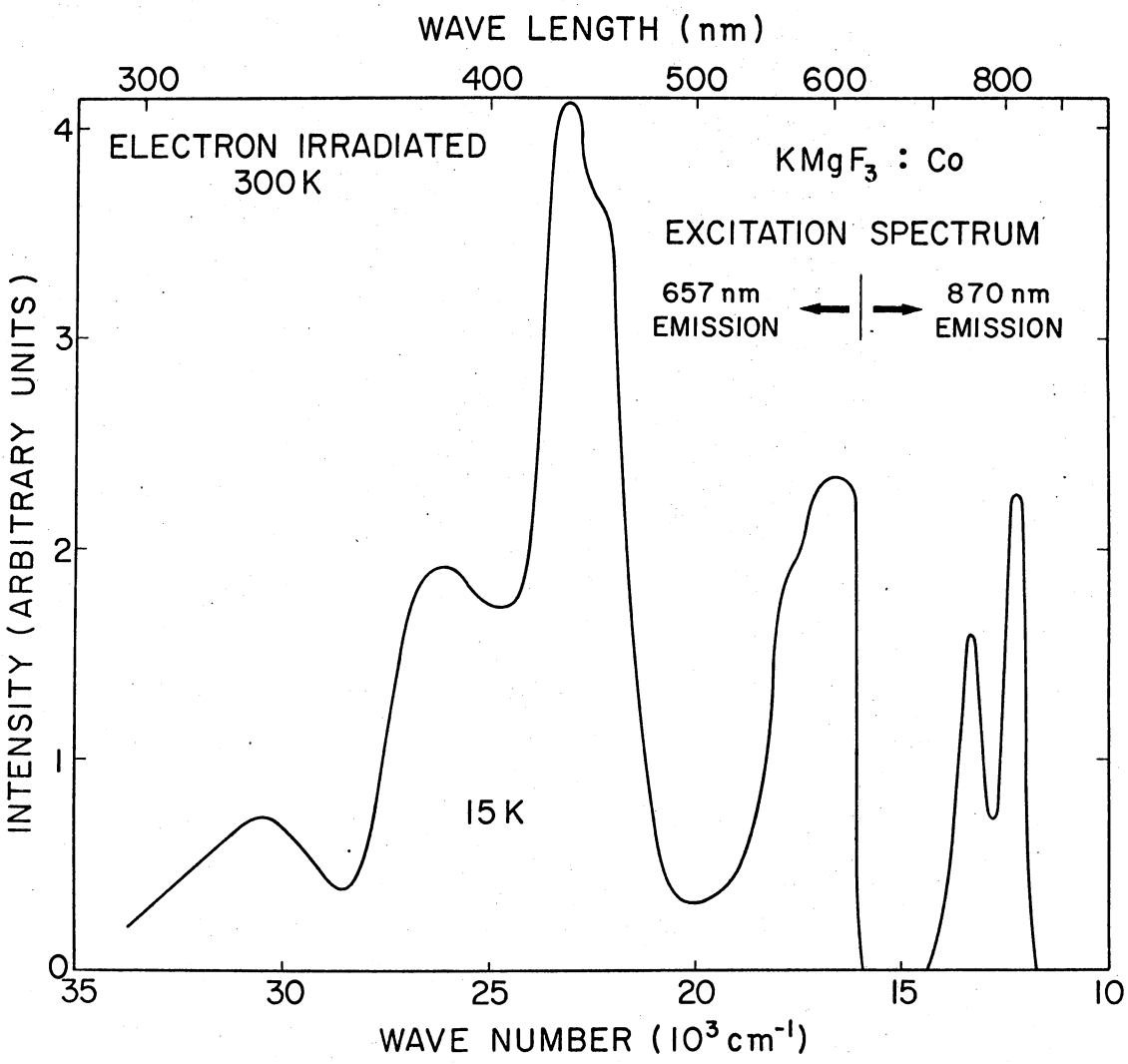

Figure 38. Excitation Spectrum for the 657 nm and 870 nm Emission Peaks

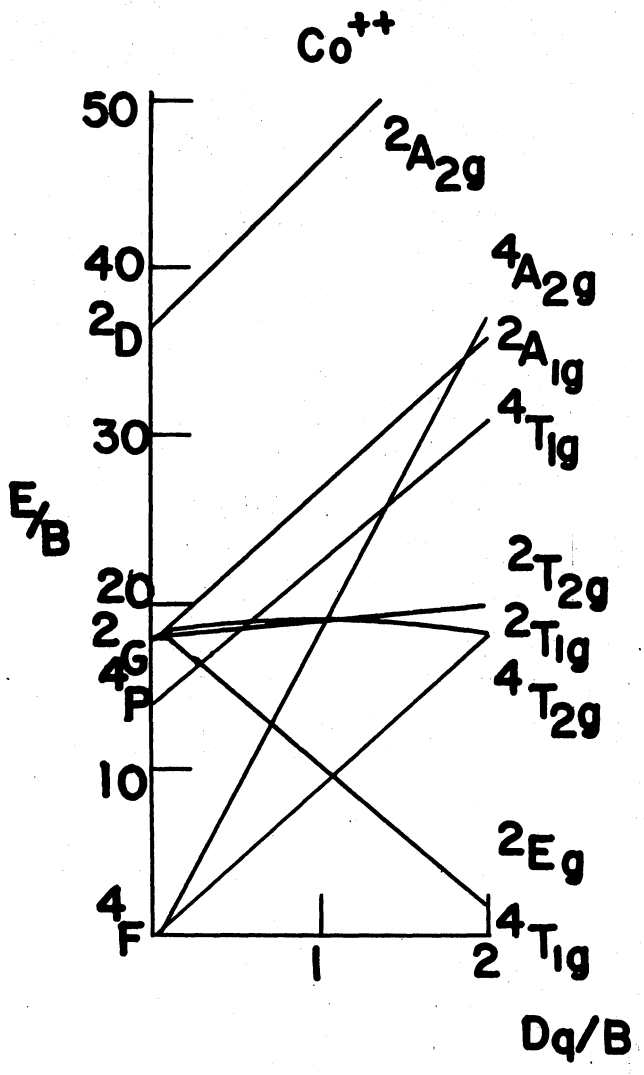

Figure 39. Tanabe Sugana Energy Diagram for Co^{2+} Ion

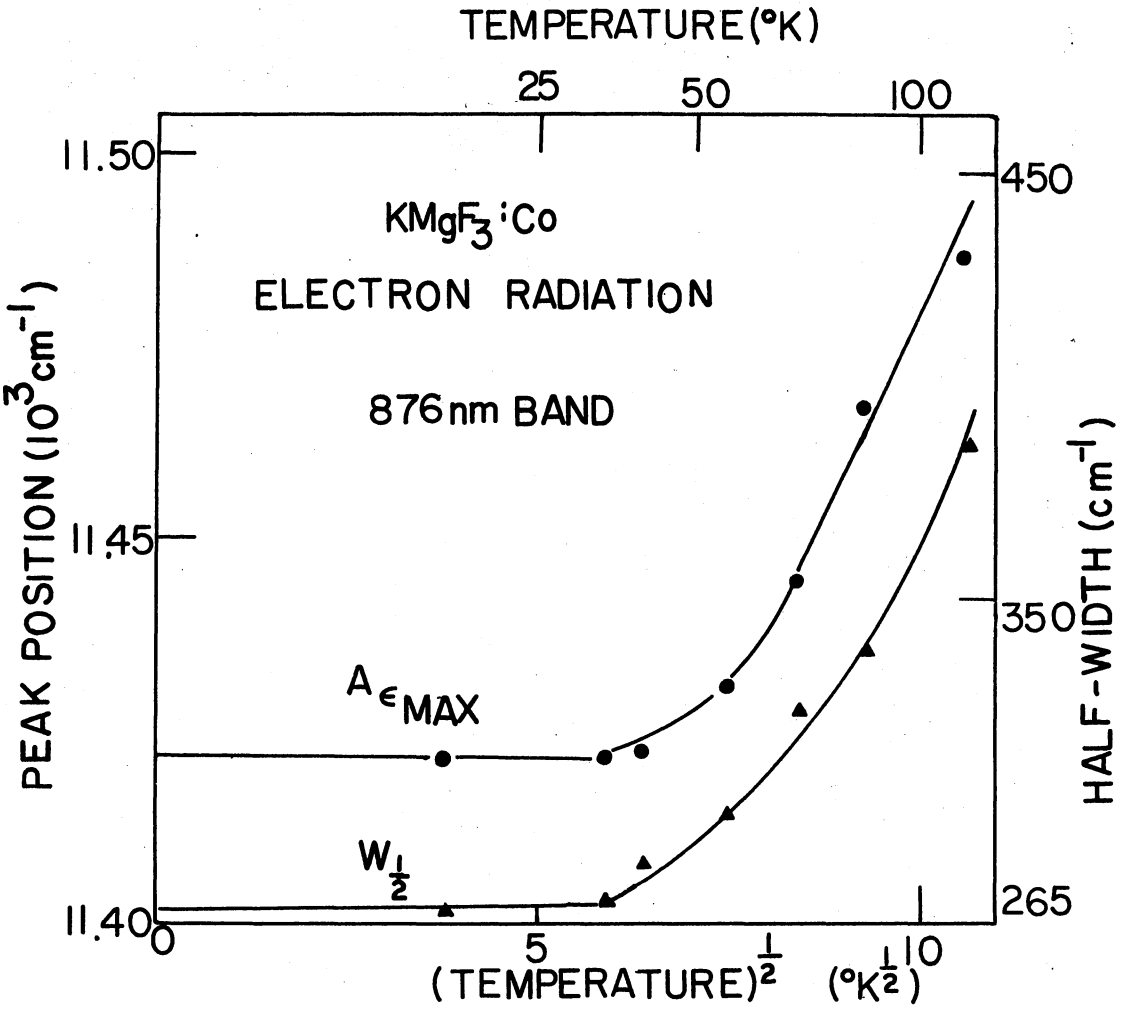

Figure 40. Temperature Dependence of Half-Width and Peak Position of 875 nm Emission Band From 300 K Electron Irradiated $KMgF_3$:Co

diagram to lower energy at higher temperatures and be very temperature dependent as shown in Figure 41. This character is evidenced by the 830 nm emission band and it is tentatively assigned to the above transition. The 658 nm band is assigned to the $^2T_{1g}$ to $^4T_{1g}$ transition of Co^{2+}. Absorption bands similar to those shown in the excitation spectrum of Figure 39 have been found previously by Aked and Simkin (67,68) on gamma irradiated $KMgF_3$:Co. As can be seen from a comparison of Figures 23 and 25, absorption spectra can be much more complex than excitation spectra and thus are more difficult to interpret. Although they interpret their bands as due to perturbed color centers, Aked and Simkin show data that have an important bearing on this work. Their annealing data indicate that bands at about 308, 345, and 600 nm anneal out together around $500^{o}K$. Although a band around 385 nm anneals at a lower temperature this is still a suggestion that the bands are connected to a particular defect. More important, they find a 800 nm absorption band present after irradiation with a zero-phonon transition at 860 nm which is the same energy as the zero-phonon emission line in the 875 nm emission, as shown in Figure 36.

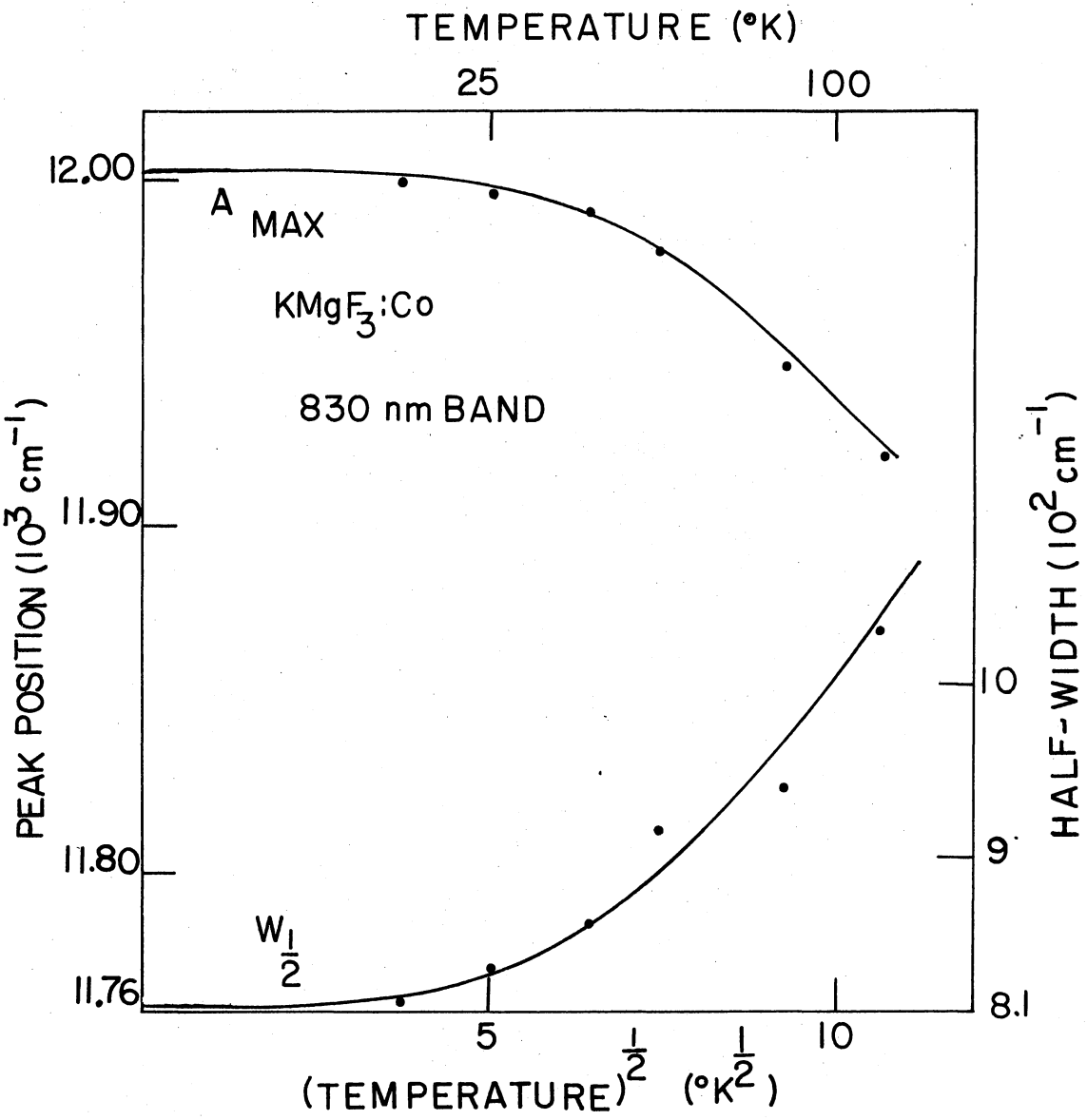

Figure 41. Temperature Dependence of Half-Width and Peak Position of 830 nm Emission Band From 300 K Electron Irradiated $KMgF_3$:Co

CHAPTER VI

COMPARISON OF THEORY AND EXPERIMENT

Energy Levels of Mn^{2+} and Co^{2+}

The bands in Figures 23 and 37 are due to perturbed Mn^{2+} and Co^{2+} transitions is shown in Table X. In this table shows the energies of the various levels as predicted by crystal field theory for the values of the crystal field parameters Dq and B shown. The prediction was made using computer programs to calculate the various energies. The program diagonalizes the energy matrices given by Chapter III. For Co^{2+}, C was fixed as 4.4 B (the same as that for the free ion), and the values of the Racah parameters B and Dq were then adjusted to obtain the best fit for the $^2E(^2H)$ and $^4A_2(^4F)$ levels. For Mn^{2+}, an equation was set as C = 3.453 B and the values of B and Dq was adjusted to obtain the best fit of $^4T_1(^4G)$ and $^4E(^4G)$. After this normalization procedure for the first two energy levels no other adjustments were made. The measured and calculated values shown in parentheses are for zero phonon line transitions. The theory should be more applicable for zero phonon lines and the values of B and Dq do vary somewhat when broad band energies or zero phonon line energies are used. The agreement between theory and experiment for the $^4A_{2g}$ level is better when the zero phonon energies are used as can be seen in Table X.

TABLE X

OBSERVED AND CALCULATED SPECTRUM FOR Co^{2+} AND Mn^{2+} IN IRRADIATED $KMgF_3$

Nature of Defect	Energy Level	Observed (10^3 cm^{-1})	Calculated (10^3 cm^{-1})
Co^{2+}-F-Center	$^4T_2(^4F)$	(a) --	6.16 (5.82)
B =948.8 cm^{-1}, C =4.4B, Dq=716.4 cm^{-1}	$^2E(^2H)$	12.19 (11.62)	12.19 (11.62)
	$^4A_2(^4F)$	13.32 (12.59)	13.32 (12.59)
	$^2T_1(^2H)$	16.60 (15.94)	17.59 (16.72)
(B =901.9 cm^{-1}, C =4.4B, Dq=667.0 cm^{-1})	$^2T_2(^2H)$	17.75	17.92 (17.08)
	$^4T_1(^4F)$	--	19.39 (18.40)
	$^2T_1(^2G)$	22.35	22.28 (21.16)
	$^2A_1(^2G)$	23.10	22.48 (21.33)
	$^2T_2(^2G)$	--	25.44 (24.15)
	$^2T_1(^2F)$	26.20	26.16 (24.83)
	$^2E(^2G)$	--	28.12 (25.68)
	$^2T_1(^2P)$	30.50	31.49 (29.37)

(a) Data From Fig. 38

TABLE X (Continued)

Nature of Defect	Energy Level	Observed (10^3 cm^{-1})	Calculated (10^3 cm^{-1})
Mn^{2+}-F-Center	$^4T_1(^4G)$	(b) 16.33	16.33
	$^4T_2(^4G)$	--	20.93
	$^4A_1(^4G)$	23.81	23.81
B =873.33 cm^{-1} C =3.453B, Dq=955.2 cm^{-1}	$^4E(^4G)$	23.81	23.81
	$^4T_2(^4D)$	--	27.64
	$^4E(^4D)$	29.60	29.92
(b) Data From Fig. 23	$^4T_1(^4P)$	31.70 34.20	33.27
	$^4A_2(^4F)$	38.50	40.30
Interstitial-Mn^{2+}-F-Center	$^4T_1(^4G)$	(c) 17.70 17.76	17.76
	$^4T_2(^4G)$	20.83 22.73	22.20
B =903.44 cm^{-1} C =3.453B, Dq=897.34 cm^{-1}	$^4E(^4G)$	24.03 24.63	24.63
	$^4A_1(^4G)$	24.75	24.63
	$^4T_2(^4D)$	28.41 29.07	28.79

TABLE X (Continued)

Nature of Defect	Energy Level	Observed (10^3 cm^{-1})	Calculated (10^3 cm^{-1})
(c) Data From Ref. 66	$^4E(^4D)$	30.12 30.96	30.95
	$^4T_1(^4P)$	32.57 34.13 35.70	33.87
	$^4A_2(^4F)$	38.72	41.71

Huang-Rhys Factor

Fine structure is observed on all of the Co^{2+} bands illustrated in Figures 33-35. This fine structure can arise from phonon-electron interactions, spin-orbit effects or a Jahn-Teller effect. The four normal modes of vibration in $KMgF_3$ have been measured as ν_1 = 450-478 cm^{-1}, ν_2 = 295-300 cm^{-1}, ν_3 = 140-156 cm^{-1}, and ν_4 = 310-350 cm^{-1} (94,95). Most of the Co^{2+} levels are spin-orbit split with the ground state having the largest splitting of about 1,000 cm^{-1} with the lowest two levels being about 333 cm^{-1} apart (96,97). In fact, in MgF_2:Co where the Co^{2+} symmetry is D_{2h} the levels are split be 152 cm^{-1}, 798. 1091, 1256, and 1398 cm^{-1} in the ground state (98). An F center defect next to a Co^{2+} ion reduces the symmetry and further splits the levels. The energy differences between the sharp lines in our spectra are shown in Table XI. There is no marked temperature dependence of these lines relative to one another and thus the transitions most likely originate in the lowest excited level. The splitting will then either give information on the spin-orbit splitting of the ground state or on the dominant phonon modes interacting with the defect. An alternate method of determining the average phonon energy of the dominant interacting phonon modes is to measure the temperatue dependence of the width at half-maximum of absorption or emission bands and use the linear coupling approximation. At very low temperature, the width at half-maximum of the bands can be written in terms of a phonon generation term S, the so-called Huang-Rhys factor, as $W^2_{\frac{1}{2}}(O) = S(\hbar\omega)^2\ 8\ \ln 2$, equation (12), at a particular temperature, T, the half-width can be expressed as $W^2_{\frac{1}{2}}(T) = W^2_{\frac{1}{2}}(O)$ coth $(\hbar\omega/2KT)$, Equation 13. From a plot of arc coth $\left(\frac{W_{\frac{1}{2}}(T)}{W_{\frac{1}{2}}(O)}\right)^2$ versus 1/T for the 658 nm, 830 nm, 875 nm bands in $KMgF_3$:Co and the 720 nm band in

TABLE XI

SPACING OF SHARP EMISSION LINES IN $KMgF_3$:Co AT $15^{o}K$

$KMgF_3$:Co			
Emission Band (nm)	Peak Position nm (cm^{-1})	Energy Difference (cm^{-1})	
658	627.4 (15939)	...	
(excitation)			
590 nm	632.2 (15818)	121	121
830	794.0 (12594)	...	
(excitation)	800.5 (12492)	102	102
746 nm	806.8 (12395)	200	98
875	860.0 (11628)	...	
(excitation)	868.0 (11521)	107	107
820 nm	875.9 (11417)	211	104

$KMgF_3$:Mn, as shown in Figure 42. It is found $\nu_{658} = 139\ cm^{-1}$, $\nu_{830} = 114\ cm^{-1}$, $\nu_{875} = 91\ cm^{-1}$, and $\nu_{720} = 223\ cm^{-1}$. The values of the Huang-Rhys factor for the Co^{2+} doped crystal are $S_{658} = 9.3$, $S_{830} = 9.2$, and $S_{875} = 1.6$. It is also possible to measure S by comparing the area of the zero phonon line to that of the broad band. This method yields $S_{658} = 5.6$, $S_{830} = 6.0$, and $S_{875} = 2.3$. The expression of Equation (10),

$$P_{vo} = \frac{S^v}{v!} e^{-S} ,$$

which arises from the linear coupling theory as shown in Chapter III, yields the ratio of the areas of the zero-phonon line and the one phonon lines. The areas of the lines in the data obtained in this lab are sufficiently close to those predicted that it is not possible to eliminate vibronic transitions as being responsible for the fine structure in Figures 33-35. In fact, consideration of the data indicates that it is impossible at this time to state whether the sharp line structure is due to electron-phonon interactions, spin-orbit splitting, the Jahn-Teller effect or a combination of these.

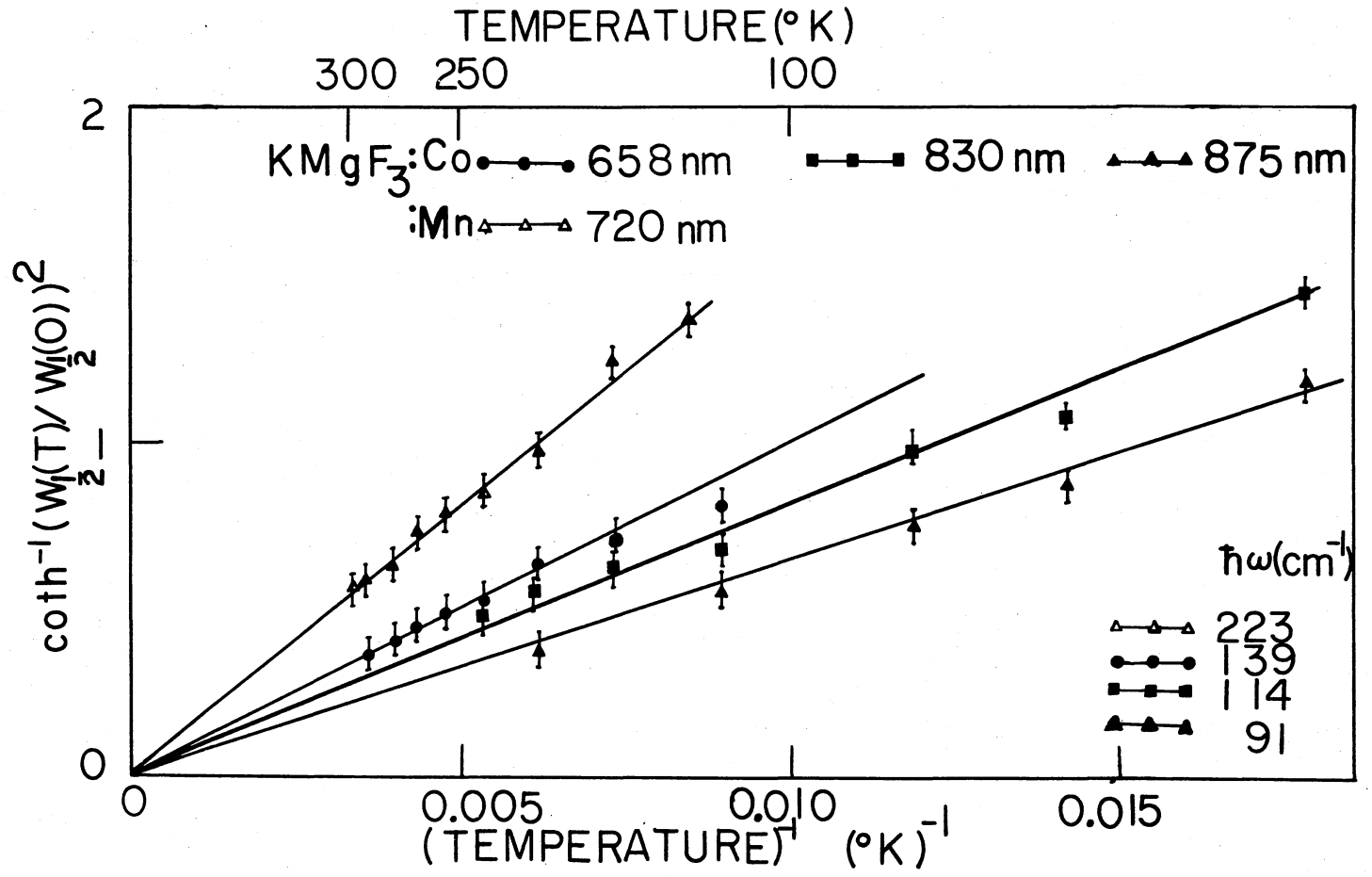

Figure 42. Temperature Dependence of 720 nm Emission Band From Irradiated $KMgF_3$:Mn and 658 nm, 830 nm, and 875 nm Emission Bands From Irradiated $KMgF_3$:Co

CHAPTER VII

SUMMARY AND PROBLEMS FOR FURTHER STUDY

By examining two optical emission bands due to Ni^{2+} ions in each of four different crystals, $KMgF_3$, $KZnF_3$, MgO, MgF_2, it has been possible to unambiguously determine the origin of the 20,000 cm^{-1} - 21,000 cm^{-1} band as arising from a $^1T_{2g} \rightarrow {}^3A_{2g}$ transition and the 13,000 cm^{-1} - 14,000 cm^{-1} band as coming from a $^1T_{2g} \rightarrow {}^3T_{2g}$ transition. The interpretation relies on the comparison of the measured transition energies in this work with existing optical absorption, emission and excitation data, on the observation of spin orbit splittings for the first excited states and on the analysis of polarization measurements in $MgF_2:Ni^{2+}$. It verifies the postulate of Bird et. al. (85). Results of stress splitting experiments in $MgO:Ni^{2+}$ are consistent with these transition assignments. After electron radiation, no notable change in band shape of these two emission bands has been observed.

The emission bands at 680 nm for $KMgF_3$:Mn and 670 nm for MgF_2:Mn are tentatively assigned due to Mn^{2+}-F center-interstitial complexes, whereas the emission bands at 720 nm for $KMgF_3$:Mn and 700 nm for MgF_2:Mn are due to Mn^{2+}-F center complexes. Although much work must yet be done to verify the presence and position of interstitial fluorines, the data presented in this work make the great potential of using 3d-transition ions as monitors for studying radiation damage quite evident. The Mn^{2+}-F center model in $KMgF_3$ has been proved correct by means of polar-

ized excitation and emission experiment and the excellent work of Young et. al. (93) by epr.

The 658 nm (15,000 cm^{-1}), 830 nm (12,000 cm^{-1}), and 875 nm (11,000 cm^{-1}) emission bands observed in irradiated $KMgF_3$:Co apparently are due to Co^{2+}-F center complexes. The 658 nm band, 830 nm band, and 875 nm band are tentatively assigned to the $^2T_{1g}$ to $^4T_{1g}$, $^4A_{2g}$ to $^4T_{1g}$, and ^2E_g to $^4T_{1g}$ transitions of Co^{2+}, respectively.

The unusually high oscillator strengths of radiation defect perturbed Mn^{2+} and Co^{2+} transitions appear to be due to exchange interactions between F centers and 3d impurities as shown by our optical bleaching experiments discussed in Chapter V.

The following projects are suggested for further study:

1. A study of radiation effects on spin allowed transition bands of Co^{2+} and Ni^{2+} ions should be initiated. From available absorption data, it appears that some of the spin allowed bands are not affected by radiation whereas spin forbidden transitions are. This result seems to have significant meaning and it would be of interest to determine why. Is it because the numbers of perturbed Co^{2+} and Ni^{2+} centers are not great enough to distinguish the absorption band changes or is it because the F-centers do not interact with these particular states. If the former is true, then more sophisticated experiments such as ESR, ENDOOR, and Emission should be undertaken and if the latter is the problem, then a theoretical analysis should be made.

2. Identification of the absorption bands at 454 nm for $KMgF_3$:Mn and 450 nm for $KMgF_3$:Ni should be made. Since the M center absorption band in $KMgF_3$ is at 445 nm, a reasonable assumption is that 454 nm and 450 nm bands could be due to a 3d impurity perturbed M center, the so-

called M_A center. This assumption should be confirmed by polarized bleaching experiments.

3. Interpretation of the fine structure of 658 nm, 830 nm, and 875 nm emission bands observed in an irradiated $KMgF_3$:Co should be obtained by means of a stress splitting experiment.

4. An additive coloration experiment on MgF_2:Mn should help to confirm the Mn^{2+}-F center model.

5. A theoretical calculation of the oscillator strength for 3d impurity-F center model must be attempted.

6. Radiation effects on 4f impurity ions should be studied to see whether or not the oscillator strengths can be enhanced by nearby radiation defects.

BIBLIOGRAPHY

(1) Bethe, H. A., Ann. Physik 3, 133 (1929).

(2) Schlapp, R. and W. G. Penney, Phys. Rev. 41, 194 (1932); 42, 666 (1932).

(3) Van Vleck, J. H., Phys. Rev. 41, 208 (1932).

(4) Van Vleck, J. H., J. Chem. Phys. 3, 803, 807 (1935).

(5) Van Vleck, J. H., J. Chem. Phys. 8, 787 (1940).

(6) Finkelstein, R. and J. H. Van Vleck, J. Chem. Phys. 8, 790 (1940).

(7) Hartmann, H. and H. L. Schlaefer, Z. Phys. 197, 115 (1951).

(8) Ilse, F. E. and H. Hartmann, Z. Phys. 197, 239 (1951).

(9) Hartmann, H. and H. L. Schlaefer, Z. Naturforsch. 6a, 751, 760 (1951).

(10) Orgel, L. E., J. Chem. Phys. 23, 1004 (1955).

(11) Orgel, L. E., J. Chem. Phys. 23, 1819 (1955).

(12) Orgel, L. E., J. Chem. Phys. 23, 1824 (1955).

(13) Tanabe, Y. and S. Sugano, J. Phys. Soc. Japan 9, 753, 766 (1954).

(14) Jorgensen, C. K., Kgl. Danske Videnskab. Selskab. Matfys. Medd. 29, No. 7 (1955).

(15) Jorgensen, C. K., Kgl. Danske Videnskab. Selskab. Matfys. Medd. 30, No. 22 (1956).

(16) Jorgensen, C. K., Kgl. Danske Videnskab. Selskab. Matfys. Medd. 29, No. 4 (1954).

(17) Jorgensen, C. K., Kgl. Danske Videnskab. Selskab. Matfys. Medd. 29, No. 8 (1955).

(18) Owen, J., Proc. Rog. Soc. of London A227, 183 (1955).

(19) Knox, K. R. G. Shulman, and S. Sugano, Phys. Rev. 130, 512 (1963).

(20) Ferguson, J., H. J. Guggenheim, and D. L. Wood, J. Chem. Phys. 40, 822 (1964).

(21) Ferguson, J. and H. J. Guggenheim, J. Chem. Phys. 44, 1095 (1966).

(22) Ferguson, J. Australia J. Chem. 21, 323 (1968).

(23) Liehr, A. D. and C. J. Ballhausen, Ann. Phys. 6, 174 (1959).

(24) Mehra, A. and P. Vehkateswarlu, J. Chem. Phys. 47, 2334 (1967).

(25) Jorgensen, C. K., Acta Chem. Scand., 9, 405 (1955).

(26) Holloway, W. W., E. W. Prohofsky and M. Kestigan, Phys. Rev. 139, A954 (1965).

(27) Klasens, H. A., P. Zalm and F. O. Huysman, Philips. Res. Rept. 8, 441 (1953).

(28) Ferguson, J., K. Knox, and D. L. Wood, J. Chem. Phys. 39, 881 (1963).

(29) Eisentein, J. C., J. Chem. Phys. 34, 1628 (1961).

(30) Nesterova, N. N., I. G. Senii, R. V. Pisarev, and P. P. Syrnikov, Sov. Phys. Solid State 9, 15 (1967).

(31) Ferguson, J., H. J. G ggenheim, and Y. Tanabe, J. Phys. Soc. Japan, 21, 692 (1966).

(32) Ferguson, J., Progress in Inorganic Chemistry, 12, 159 (1970) edited by S. J. Lippard C. Interscience, New York.

(33) Ferguson, J., H. J. Guggenheim and Y. Tanabe, J. Appl. Phys. 36, 1046 (1965).

(34) Ferguson, J., H. J. Guggenheim and Y. Tanabe, Phys. Rev. Letters 14, 737 (1965).

(35) Ferguson, J., H. J. Guggenheim and E. R. Krausz, J. Phys. C, 4, 1866 (1971).

(36) Ferguson, J., H. J. Guggenheim and Y. Tanabe, J. Chem. Phys., 45, 1134 (1966).

(37) Codling, A. J. B., J. Phys. C 4, 1409 (1971).

(38) Markham, J. J., Solid State Physics, Suppl. 8, (Academic Press, N. Y., 1966).

(39) Vehse, W. E., W. A. Sibley, F. J. Keller, and Y. Chen, Phys. Rev. 167, 828 (1968).

(40) Ward, W. C., E. B. Henseley, Phys. Rev. 175, 1230 (1968).

(41) Vehse, W. E., O. E. Facey, and W. A. Sibley, Phys. Stat. Sol. (a)1, 679 (1970).

(42) Hersh, H. N., and Bronstein, Am. J. Phys. 25, 306 (1957).

(43) Uchida, Y. and Y. Nakai, J. Phys. Soc. Japan 8, 795 (1953).

(44) Paramo, N., J. Phys. Soc. Japan 30, 1106 (1971).

(45) Sonder, E., W. A. Sibley, In Point Defects in Solids, edited by J. H. Crawford and L. M. Slifkin (Plenum, N. Y. 1972).

(46) Crawford, J. H., Adv. In Physics 17, 93 (1968).

(47) Seitz, F., Rev. Mod. Phys. 26, 7 (1954).

(48) Seitz, F., Rev. Mod. Phys. 18, 384 (1946).

(49) Schulman, J. H. and W. D. Compton, Color Centers in Solids, Pergamon, N. Y., 1971.

(50) Compton, W. D. and Rabin, Solid State Physics, 16, 121 (1964), edited by F. Seitz and D. Turnbull (Academic Press, N. Y.).

(51) Fowler, W. B., Physics of Color Center (Academic Press, N. Y., 1968).

(52) Crawford, J. H., and L. M. Slifkin, Point Defects in Solids, (Plenum, N. Y., 1972).

(53) Van Doorn, C. Z. Philips, Res. Rept. Suppl. 4, 1 (1962).

(54) Knox, R. S., Phys. Rev. Letters 2, 87 (1958).

(55) DeBoer, J. H., Receuil Trav. Chim. Pays-Bus 56, 301 (1937).

(56) Hall, T. P. P. and A. Leggeat, Solid State Commun. 7, 1657 (1969).

(57) Riley, C. R. and W. A. Sibley, Phys. Rev. B 1, 2789 (1970).

(58) Riley, C. R., Ph.D. Thesis (University of Tennessee, 1970).

(59) Riley, C. R., S. I. Yun, and W. A. Sibley, Phys. Rev. B5, 3285 (1972).

(60) Yun, S. I., Ph.D. Thesis (Oklahoma State University, 1973).

(61) Lewis, J. T., J. L. Kolopus, E. Sonder and M. M. Abraham, Phys. Rev. B7, 810 (1973).

(62) Rhoads, J. E., B. H. Rose, and L. E. Halliburton, Phys. Rev. (to be published).

(63) Rhoads, J. E., Ph.D. Thesis (Oklahoma State University, 1974).

(64) Alcala, R., N. Koumvakalis, W. A. Sibley, Phys. St. Solidi (to be published).

(65) Vehse, W. E. and W. A. Sibley, Phys. Rev. B6, 2443 (1972).

(66) Sibley, W. A., S. I. Yun, W. E. Vehse, J. Phys. C6, 1105 (1973).

(67) Aked, N. H. and D. J. Simkin, Bull. Am. Phys. Soc. 18, 1578 (1973).

(68) Aked, N. H., Master's Thesis (McGill University, 1973).

(69) Ralph, J. E. and M. G. Townsend, J. Phys. C3, 8 (1970).

(70) Yun, S. I., L. A. Kappers, and W. A. Sibley, Phys. Rev. B8, 773 (1973).

(71) Bridgman, P. W., Proc. Am. Acad. Arts Sci. 60, 303 (1925).

(72) Stockbarger, D. C., Rev. Sci. Instr. 7, 133 (1936).

(73) Stockbarger, D. C., Discussion Faraday Soc. 5, 294, 299 (1949).

(74) Cotton, F. A., Chemical Applications of Group Theory (Wiley, New York, 1971).

(75) Thomas, L. H., Nature 117, 514 (1926).

(76) Frankel, J., Z. Physik 37, 243 (1926).

(77) Keil, T. H., Phys. Rev. 140, A601 (1965).

(78) Huang, K. and A. Rhys. Proc. Roy. Soc. (London) A204, 406 (1950).

(79) Sturge, M. D., Solid State Comm. 9, 899 (1971).

(80) Manson, N. B., Phys. Rev. B4, 2645 (1971).

(81) Manson, N. B., W. V. Ohe, and S. L. Chodos, Phys. Rev. B3, 1968 (1971).

(82) Hafele, H. G., Ann. Phys. 10, 321 (1963).

(83) Barker, A. S., Jr., J. A. Ditzenberger, and H. J. Guggenheim, Phys. Rev. 175, 1180 (1968).

(84) Porto, S. P. S., P. A. Fleury, and T. C. Damen, Phys. Rev. 154, 522 (1967).

(85) Bird, B. D., G. A. Osbome, and P. J. Stephens, Phys. Rev. B5, 1800 (1972).

(86) Mason, N. B., Phys. Rev. B4, 2656 (1971).

(87) Ferguson, J., H. J. Guggenheim, H. Kamimura, and Y. Tanabe, J. Chem. Phys. 42, 775 (1965).

(88) McClure, D. S., Solid State Physics, 9, 399 (1959) edited by F. Seitz and Turnbull (Academic Press, N. Y.).

(89) Hush, N. S. and R. J. M. Hobbs, Progress in Inorganic Chemistry 10, 259 (1968), edited by F. A. Cotton (Intersicence, N.Y.).

(90) Moreau, N., A. C. Boccara, and J. Badoz, Phys. Rev. B10, 64 (1974).

(91) Ikeya, M. and N. Itoh, J. Phys. Soc. Japan 26, 291 (1969).

(92) Feofilov, P. P., The Physical Basis of Polarized Emission (Consultants Bureau, N. Y., 1961).

(93) Young, M. A., E. E. Kohnke, and L. E. Halliburton (Private communication; to be submitted to Phys. Rev.).

(94) Hunt, G. and C. H. Perry, Phys. Rev. 134, A688 (1964).

(95) Nakagawa, I., A. Tsuchida and T. Shimanouchi, J. Chem. Phys. 47, 982 (1967).

(96) Liehr, A. D., J. Phys. Chem. 67, 1314 (1963).

(97) Sturge, M. D., Phys. Rev. B8, 6 (1973).

(98) Gladney, H. M., Phys. Rev. 146, 253 (1966).

VITA

Kuo-hua Lee

Candiate for the Degree of

Doctor of Philosophy

Thesis: EFFECT OF RADIATION INDUCED DEFECTS ON THE OPTICAL TRANSITIONS OF 3-d IMPURITIES

Major Field: Physics

Biographical:

Personal Data: Born in Hua, Canton, April 25, 1946, the son of Mr. and Mrs. Hung-chao Lee.

Education: Attended primary and secondary schools in Hsin-chu Taiwan, Republic of China; graduated from Hsin-chu First High School in 1964; attended Tatung Institute of Technology, Taipei, Taiwan (1965-69) with major in Electrical Engineering; received Bachelor of Science in June, 1969; attended Northeast Louisiana University, Monroe, Louisiana (1970-72); received Master of Science in Physics in August, 1972; attended Oklahoma State University (1972-75); received Master of Science in Electrical Engineering in July, 1974; completed requirement for the Doctor of Philosophy degree in July, 1975.

Experience: Employed as Teaching Assistant in the Mathematics Department of Northeast Louisiana University, Monroe, Louisiana (1970-71) and as Graduate Teaching Assistant in the Physics Department of NLU (1971-72); Graduate Teaching Assistant in the Physics Department of Oklahoma State University, Stillwater, Oklahoma (1972-73); Graduate Research Assistant in the Physics Department of Oklahoma State University (1973-75).

Organization: Member of Sigma Pi Sigma.